DYNAMIC STRESS INTENSITY FACTORS
FOR HOMOGENEOUS AND NONHOMOGENEOUS MATERIALS
USING THE INTERACTION INTEGRAL METHOD

BY

SEONG HYEOK SONG

B.E., University of Seoul, 2000

THESIS

Submitted in partial fulfillment of the requirements
for the degree of Master of Science in Civil Engineering
in the Graduate College of the
University of Illinois at Urbana-Champaign, 2003

Urbana, Illinois

Abstract

DYNAMIC STRESS INTENSITY FACTORS
FOR HOMOGENEOUS AND NONHOMOGENEOUS MATERIALS
USING THE INTERACTION INTEGRAL METHOD

Seong Hyeok Song

Department of Civil and Environmental Engineering
University of Illinois at Urbana-Champaign

Glaucio H. Paulino, Advisor

Dynamic stress intensity factors (DSIFs) are important fracture parameters in understanding and predicting dynamic behavior of a cracked body. To evaluate DSIFs for both homogeneous and nonhomogeneous materials, the interaction integral (conservation integral) originally proposed to evaluate SIFs for a static homogeneous medium is extended to incorporate dynamic effects and material nonhomogeneity, and is implemented in conjunction with the finite element method. In this study, a research code is developed and verified using benchmark problems. Then, various homogeneous and nonhomogeneous cracked bodies under dynamic loading are employed to investigate dynamic fracture behavior such as the variation of DSIFs for different material profiles, the relation between initiation time and the domain size (for integral evaluation), and the contribution of each distinct term in the interaction integral.

For the Glory of God

Acknowledgments

The author would like to express his profound gratitude to his advisor Professor Glaucio H. Paulino. He provided the author endless support, excellent guidance, invaluable suggestions and warm encouragement during his study. His comments and suggestions helped improve the content and clarity of this thesis. The author is also deeply indebted to Professor William G. Buttlar for his patience and warm encouragement.

The author is grateful to his colleagues, Dr. Jeong-Ho Kim and Matthew C. Walters, for their suggestions in this study and their help in reviewing this thesis. The author would like to thank his colleagues: Mr. Alok Sutradhar, Ms. Zhengyu Zhang, Ms. Mariana F.T. Silva, Ms. Fang-Ju Chou, and Mr. Michael P. Wagoner.

The author heartily appreciates his wife, Seong Im Jin, for her endless patience, support, and encouragement.

Table of Contents

List of Tables

List of Figures

List of Abbreviations

2D Two-Dimensional

3D Three-Dimensional

BEM Boundary Element Method

CCT Center Cracked Tension

COD Crack Opening Displacement

DCT Displacement Correlation Technique

DISFs Dynamic Stress Intensity Factors

EDI Equivalent Domain Integral

EFG Element Free Galerkin

FDM Finite Difference Method

FEM Finite Element Method

FGM Functionally Graded Materials

GIF Generalized Isoparametric Formulation

Q8 Eight-node Quadrilateral

QPE Quarter Point Element

SIFs Stress Intensity Factors

T6 Six-node Triangular

Chapter 1

Introduction

Stress intensity factors (SIFs) are important fracture parameters in understanding dynamic fracture behavior for both homogeneous and nonhomogeneous materials. For evaluation of SIFs, various methods have been proposed, such as displacement correlation technique (DCT) [3, 5, 39], standard and modified J integral [19, 21, 32, 50, 59]. The interaction integral is a two-state integral, which was originally proposed to determine SIFs for homogeneous materials under quasi-static conditions by Yau et al. [60]. In this work, the interaction integral is extended to include material gradient and dynamic effects to investigate fracture behavior. In this Chapter, comprehensive literature reviews on the evaluation of dynamic stress intensity factors (DSIFs) for homogeneous and nonhomogeneous materials are addressed. Then, dynamic stress fields are derived to explain dynamic behavior of a cracked body. Finally, dynamic auxiliary fields for nonhomogeneous materials are discussed in conjunction with the interaction integral.

1.1 Literature Review on Dynamic Stress Intensity Factors

DSIFs are relevant to determine the stress state of a cracked body. Thus, an accurate evaluation of DSIFs is crucial in fracture mechanics as they can be used to investigate crack initiation and propagation. Several methods have been developed and applied by many researchers to evaluate DSIFs for various problems, as discussed below.

For homogeneous materials, Chen [9] examined a centrally cracked rectangular finite strip subjected to step loading using a Lagrangian finite difference method (FDM). DSIFs were obtained from the relation between DSIFs and stress fields in the vicinity of a crack tip. This problem has been considered as a benchmark problem and explored by many researchers. Aoki et al. [3] utilized the relationship between displacements and DSIFs to obtain mode I or mode III DSIFs. Kishimoto et al. [32] proposed a modified path-independent J-integral, which involves the inertial effects to determine DSIFs in conjunction with the finite element method (FEM), and employed a decomposition procedure for mixed-mode problems. Brickstad [5] used an explicit time scheme in a special FEM program to evaluate DSIFs. By means of the relationship between SIFs and crack opening displacement, DSIFs were determined without singular elements. Murti and Valliappan [39] examined various problems, such as Chen's problem [9], using quarter-point elements (QPEs) and the FEM. DSIFs were evaluated from the relation between the first two coefficients of Williams [58] solution and the finite element displacement in the vicinity of the crack. The effect of QPE size was assessed qualitatively in their works. Lee and Freund [35] solved mixed mode problems of a semi-infinite plate containing an edge crack under an impact loading and determined DSIFs through linear superposition of several stress wave propagation solutions. Lin and Ballmann [36] revisited Chen's problem [9] using the Lagrangian FDM. They adopted the same technique by Chen [9] to evaluate DSIFs. Their numerical results are almost identical with those obtained by Chen except for a few time periods when wave fluctuations occurs. They contended that Chen [9] used too few cells to capture actual peaks of DSIFs. Dominguez and Gallego [16] computed DSIFs using time domain boundary element method with singular quarter-point boundary elements. Fedelinski et al. [21] adopted the $\hat{J}$-integral to obtain DSIFs by means of the dual boundary element method. In the $\hat{J}$-integral approach, the mode decomposition procedure is employed for mixed mode problems. Belytschko et al. [4] determined static and dynamic SIFs using the Element Free Galerkin (EFG) method, which is a meshless method based on moving least square interpolants. The DSIFs were calculated by conservation integrals, which directly evaluate the individual SIFs for the mixed mode problem in terms of known auxiliary solutions. Sladek et al. [50, 51] used the $\hat{J}$-integral to determine DSIFs in conjunction with the boundary element method (BEM). They proposed the interaction integral for the computation of T-stress (non-singular stress), and the $\hat{J}$-integral for the evaluation of DSIFs. Krysl and Belytschko [34] investigated three-dimensional (3D) stationary and dynamically propagating crack problems. DSIFs were obtained from the interaction integral in conjunction with the EFG method. Zhang [61] explored transient dynamic problems using hypersingular time-domain traction BEM. DSIFs were obtained from relating the crack tip opening displacements and SIFs. Tabiei and Wu [52] investigated fracture behavior including DSIFs and energy release rate for a cracked body subjected to dynamic loadings using DYNA3D [57], which is a non-linear explicit finite element code. An element deletion-and-replacement remeshing scheme was employed using the FEM to simulate crack propagation. Enderlein et al. [19] investigated fracture behavior for two-dimensional (2D) and 3D cracked bodies under impact loading using FEM. They adopted the J-integral, the modified crack closure integral and the displacement correlation technique to evaluate pure mode I DSIFs.

For bimaterials, Tan and Meguid [53] examined cracked body where cracks are perpendicular to bimaterial interfaces. They utilized the relationship between stress and SIFs near the crack tip to evaluate DSIFs. Chang and Wu [8] proposed a pair of contour integrals to obtain DSIFs for a crack normal to a bimaterial interface.

For nonhomogeneous materials, Rousseau and Tippur [48] obtained DSIFs for FGMs both numerically and experimentally. The DSIFs prior to crack initiation were determined utilizing asymptotic fields of Williams' solution [58], which is equivalent to the stationary fields. After initiation, the crack tip fields for steadily growing cracks in FGMs obtained by Parameswaran and Shukla [43] were used to obtain DSIFs. Material gradients were employed in the commercial software ABAQUS [1] by applying temperature, which is a function of material properties, and by letting the coefficient of thermal expansion be zero. As the distance is close to the crack tip, the DSIFs were underestimated because no singular elements were used. Therefore, regression technique was employed to obtain DSIFs at the crack tip based on the DCT. Wu et al. [59] extended the J-integral to incorporate material gradients and dynamic effects. They evaluated J for a single edge cracked FGM panel under step loading in conjunction with the EFG method.

Unlike the works mentioned above, Gurtin [25] proposed a path independent integral in the time domain for stationary and moving crack, utilizing convolution as basic tools. He assumed that the body is homogeneous and body force is zero. This integral is well defined and path-independent for a moving crack at a given time. Notice that if we transform the integral from time domain into Laplace domain, the integral by Gurtin [25] is equivalent to the integral by Nilsson [42].

1.2 Dynamic Stress Fields

Delale [14] stated that "in nonhomogeneous materials with continuous and continuously differentiable elastic constants the nature of the stress singularity at a crack tip would be identical to that of a homogeneous solid". Eischen [18] investigated static crack tip fields for nonhomogeneous materials by extending Williams' eigenfunction expansion technique. In his work, he concluded that if the material properties (Young's modulus E and Poisson's ratio ν) are continuous, bounded and generally differentiable functions of space satisfying the conditions $E > 0$ and $-1 < \nu < 1/2$ everywhere in the domain, then the asymptotic singular stress ($O(r^{-1/2})$) and the associated displacement ($O(r^{1/2})$) fields around the crack tip in nonhomogeneous materials are identical to those in homogeneous materials. However, the higher order terms for nonhomogeneous materials do differ from those for homogeneous materials.

Rice [47] obtained dynamic stress fields of homogeneous materials for constant crack tip speed. Then, Freund [22], Freund and Clifton [23] and Nilsson [42] investigated dynamic stress fields of homogeneous materials for non-uniformly moving crack speed. They observed that, under dynamic loading, the stress fields retain $1/\sqrt{r}$ singularity, which is the same as the static case. However, if the crack propagates, the solution also depends on the crack speed .

Dynamic problems of nonhomogeneous materials are naturally more involved than those of homogeneous materials. Chiu and Erdogan [11] examined one-dimensional wave propagation in a functionally graded elastic medium using Laplace transform technique. Parameswaran and Shukla [43] investigated stress fields around a crack tip which propagates with constant speed in nonhomogeneous materials. They also concluded that the asymptotic singular dynamic stress fields in nonhomogeneous materials are identical to those in homogeneous materials.

In summary, the asymptotic singular stress fields of nonhomogeneous materials under dynamic loading show similar behavior to those of homogeneous materials under quasi-static condition as discussed above [18, 22, 23, 42, 43]. In this section, wave equations are derived and discussed. Then, dynamic stress fields for mode I under steady state condition are provided. The mode I stress fields are obtained by applying Helmholtz decomposition procedures and boundary conditions such as traction free around the crack faces.

1.2.1 Linear Elastodynamics

For dynamic problems, the governing equilibrium equation is given by [2, 22]

$$\sigma_{ij,j} + f_i = \rho(\boldsymbol{x})\ddot{u}_i, \tag{1.1}$$

where $\rho(\boldsymbol{x})$ is mass density which varies spatially, f_i denotes the body force components, σ_{ij} refers to the stress component, and each super-imposed dot indicates a derivative with respect to time. The compatibility condition and constitutive relation are expressed by

$$\varepsilon_{ij} = \frac{1}{2}(u_{i,j} + u_{j,i}), \tag{1.2}$$

$$\sigma_{ij} = \lambda(\boldsymbol{x})\delta_{ij}\varepsilon_{kk} + 2\mu(\boldsymbol{x})\varepsilon_{ij}, \tag{1.3}$$

respectively, where $\lambda(\boldsymbol{x})$ and $\mu(\boldsymbol{x})$ are the Lame constants which are a function of coordinates, and the strain displacement relation, Eq. (1.2), is valid for infinitesimal strains.

With no body force, a combination of Eqs. (1.1), (1.2) and (1.3) leads to the following equation:

$$\mu(\boldsymbol{x})u_{i,jj} + (\lambda(\boldsymbol{x}) + \mu(\boldsymbol{x}))u_{j,ji} + \lambda(\boldsymbol{x})_{,i}u_{k,k} + \mu(\boldsymbol{x})_{,j}(u_{i,j} + u_{j,i}) = \rho(\boldsymbol{x})\ddot{u}_i. \tag{1.4}$$

If homogeneous materials are adopted, Eq. (1.4) is reduced to the Navier's equation:

$$\mu\nabla^2\boldsymbol{u} + (\lambda + \mu)\nabla(\nabla \cdot \boldsymbol{u}) = \rho\ddot{\boldsymbol{u}} \quad \text{or} \quad \mu u_{i,jj} + (\lambda + \mu)u_{j,ji} = \rho\ddot{u}_i. \tag{1.5}$$

Using the vector identity $\nabla \times (\nabla \times \boldsymbol{u}) = \nabla(\nabla \cdot \boldsymbol{u}) - \nabla^2\boldsymbol{u}$, one rewrites Eq. (1.5) as follows

$$c_d^2\nabla(\nabla \cdot \boldsymbol{u}) - c_s^2\nabla \times (\nabla \times \boldsymbol{u}) = \ddot{\boldsymbol{u}}, \tag{1.6}$$

where c_d and c_s are dilatational and shear wave speeds, respectively, given by

$$c_d = \sqrt{\frac{\lambda + 2\mu}{\rho}} \quad \text{and} \quad c_s = \sqrt{\frac{\mu}{\rho}}\ . \tag{1.7}$$

Multiplying Eq. (1.6) by the divergence operator ($\nabla\cdot$), one obtains

$$c_d^2\nabla^2(\nabla \cdot \boldsymbol{u}) = (\nabla \cdot \boldsymbol{u})_{,tt} \quad \text{or} \quad c_d^2(u_{i,i})_{,jj} = (u_{i,i})_{,tt} \tag{1.8}$$

Moreover, multiplying Eq. (1.6) by the curl operator ($\nabla\times$), one obtains

$$c_s^2\nabla^2(\nabla \times \boldsymbol{u}) = (\nabla \times \boldsymbol{u})_{,tt} \ \text{ or } \ c_s^2(\epsilon_{ijk}u_{k,j})_{,nn} = (\epsilon_{ijk}u_{k,j})_{,tt}\ . \tag{1.9}$$

The dilatation $\nabla \cdot \boldsymbol{u}$ and the rotation vector $(\nabla \times \boldsymbol{u})/2$ satisfy the wave equation with dilatational wave speed (c_d) and shear wave speed (c_s), respectively.

1.2.2 Dynamic Stress Fields for Homogeneous Materials

Parameswaran and Shukla [43] examined crack tip dynamic stress fields in nonhomogeneous materials under steady state condition and concluded that the dynamic stress fields for nonhomogeneous materials retain singularity, which is the same for homogeneous materials. In their work, two material variations are adopted: (1) exponential variation of shear modulus and mass density; (2) linear variation of the shear modulus with constant mass density.

However, these material variations do not represent real material profiles. Moreover, the steady state condition that they assumed is questionable because material nonhomogeneity induces varying crack tip speed. Therefore, dynamic stress fields for homogeneous materials are derived in this section.

Wave equations are solved by means of Helmholtz decomposition of displacements [2, 22]:

$$u_x = \frac{\partial \phi}{\partial X} + \frac{\partial \psi}{\partial Y}, \; u_y = \frac{\partial \phi}{\partial Y} - \frac{\partial \psi}{\partial X}, \tag{1.10}$$

where (X, Y) represents the fixed coordinate before the crack propagates, and ϕ and ψ are the dilatational and shear wave potentials, respectively. As illustrated in Figure 1.1, V is crack tip speed, t is time, (x, y) is the coordinate system based on the current crack tip, and (X, Y) is the coordinate system based on the original crack tip.

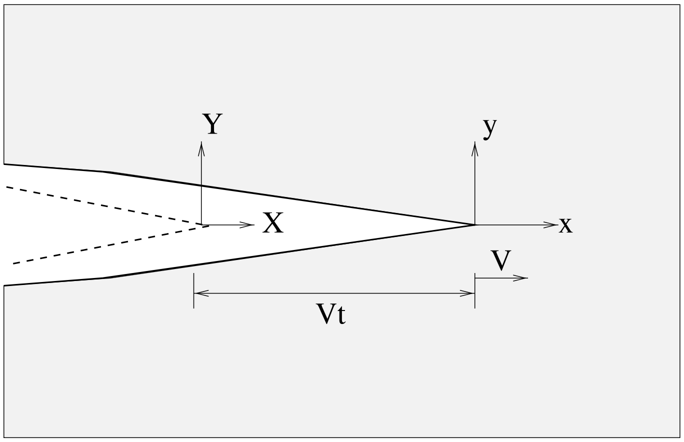

Figure 1.1: Two coordinate systems under steady state condition. Dashed line indicates the original crack faces, while solid line represents the current crack faces. At time t=0, the crack starts to grow from the origin (X, Y) with a constant velocity V.

Stress can be expressed in terms of displacement potential using Eqs. (1.2), (1.3) and (1.10) for homogeneous materials

$$\begin{aligned}
\sigma_{xx} &= (2\mu+\lambda)\left(\frac{\partial^2 \phi}{\partial X^2} + \frac{\partial^2 \phi}{\partial Y^2}\right) - 2\mu \frac{\partial^2 \phi}{\partial Y^2} + 2\mu \frac{\partial^2 \psi}{\partial X \partial Y}, \\
\sigma_{yy} &= (2\mu+\lambda)\left(\frac{\partial^2 \phi}{\partial X^2} + \frac{\partial^2 \phi}{\partial Y^2}\right) - 2\mu \frac{\partial^2 \phi}{\partial X^2} - 2\mu \frac{\partial^2 \psi}{\partial X \partial Y}, \\
\sigma_{xy} &= 2\mu \frac{\partial^2 \phi}{\partial X \partial Y} + \mu \left(\frac{\partial^2 \psi}{\partial^2 Y} - \frac{\partial^2 \psi}{\partial X^2}\right).
\end{aligned} \tag{1.11}$$

Substituting Eq. (1.10) into Eq. (1.6), one obtains

$$\begin{aligned}(\lambda+2\mu)\frac{\partial}{\partial X}\left(\frac{\partial\phi^2}{\partial X^2}+\frac{\partial\phi^2}{\partial Y^2}\right)+\mu\frac{\partial}{\partial Y}\left(\frac{\partial\psi^2}{\partial X^2}+\frac{\partial\psi^2}{\partial Y^2}\right) &= \rho\left(\frac{\partial}{\partial X}\frac{\partial^2\phi}{\partial t^2}+\frac{\partial}{\partial Y}\frac{\partial^2\psi}{\partial t^2}\right), \\ (\lambda+2\mu)\frac{\partial}{\partial Y}\left(\frac{\partial\phi^2}{\partial X^2}+\frac{\partial\phi^2}{\partial Y^2}\right)-\mu\frac{\partial}{\partial Y}\left(\frac{\partial\psi^2}{\partial X^2}+\frac{\partial\psi^2}{\partial Y^2}\right) &= \rho\left(\frac{\partial}{\partial X}\frac{\partial^2\phi}{\partial t^2}-\frac{\partial}{\partial Y}\frac{\partial^2\psi}{\partial t^2}\right)\end{aligned} \tag{1.12}$$

In order to satisfy Eq. (1.12), the potentials ϕ and ψ should be wave functions satisfying

$$c_d^2\nabla^2\phi-\ddot{\phi}=0 \text{ and } c_s^2\nabla^2\psi-\ddot{\psi}=0. \tag{1.13}$$

The double differentiation of each wave potential with respect to time yields

$$\ddot{\phi}=V^2\frac{\partial^2\phi}{\partial x^2}-2V\frac{\partial^2\phi}{\partial x\partial t}+\frac{\partial^2\phi}{\partial t^2}-\dot{V}\frac{\partial\phi}{\partial x}, \tag{1.14}$$

$$\ddot{\psi}=V^2\frac{\partial^2\psi}{\partial x^2}-2V\frac{\partial^2\psi}{\partial x\partial t}+\frac{\partial^2\psi}{\partial t^2}-\dot{V}\frac{\partial\psi}{\partial x}. \tag{1.15}$$

The first term on the right hand side of Eqs. (1.14) and (1.15) dominates the stress field of Eq. (1.11) in the near-tip regions.

In order to express the rate of change of each wave potential in terms of space derivative, a new moving coordinate system is used:

$$x=X-Vt \quad\text{and}\quad y=Y. \tag{1.16}$$

By substituting the dominant terms of Eqs. (1.14) and (1.15) into Eq. (1.13), one obtains the following relationships:

$$\alpha_d^2\frac{\partial^2\phi}{\partial x^2}+\frac{\partial^2\psi}{\partial y^2}=0 \text{ and } \alpha_s^2\frac{\partial^2\psi}{\partial x^2}+\frac{\partial^2\phi}{\partial y^2}=0, \tag{1.17}$$

where α_d and α_s are nondimensional parameters relating crack tip speed and wave speed given by

$$\alpha_d=1-\left(\frac{V}{c_d}\right)^2 \text{ and } \alpha_s=1-\left(\frac{V}{c_s}\right)^2. \tag{1.18}$$

In order to solve the wave equation, i.e. Eq.(1.17), Freund and Clifton [23] applied a complex variable method. Using traction free boundary conditions at the crack faces, $\sigma_{yy}=\tau_{xy}=0$, dynamic stress fields for the mode I crack under steady state condition are obtained by

$$
\begin{aligned}
\sigma_{xx} &= \frac{K_I(t)}{\sqrt{2\pi r}} \frac{1+\alpha_s^2}{D(t)} \left[\left(1+2\alpha_d^2-\alpha_s^2\right) \cos\left(\frac{\theta_1}{2}\right) \sqrt{\frac{r}{r_1}} - \frac{4\alpha_d\alpha_s}{1+\alpha_s^2} \cos\left(\frac{\theta_2}{2}\right) \sqrt{\frac{r}{r_2}} \right], \\
\sigma_{yy} &= \frac{K_I(t)}{\sqrt{2\pi r}} \frac{1+\alpha_s^2}{D(t)} \left[-\left(1+\alpha_s^2\right) cos\left(\frac{\theta_1}{2}\right) \sqrt{\frac{r}{r_1}} - \frac{4\alpha_d\alpha_s}{1+\alpha_s^2} \cos\left(\frac{\theta_2}{2}\right) \sqrt{\frac{r}{r_2}} \right], \\
\sigma_{xy} &= \frac{K_I(t)}{\sqrt{2\pi r}} \frac{2\alpha_d(1+\alpha_s^2)}{D(t)} \left[\sin\left(\frac{\theta_1}{2}\right) \sqrt{\frac{r}{r_1}} - \sin\left(\frac{\theta_2}{2}\right) \sqrt{\frac{r}{r_2}} \right],
\end{aligned} \tag{1.19}
$$

where

$$D(t) = 4\alpha_d\alpha_s - (1+\alpha_s^2)^2. \tag{1.20}$$

Equation (1.19) is reduced to Williams' solution under stationary condition, i.e. $V = 0$.

1.3 Dynamic Auxiliary Fields for Nonhomogeneous Materials

The interaction integral utilizes two admissible fields: auxiliary and actual fields. Auxiliary fields are based on known fields such as Williams' solution [58], while actual fields utilize quantities such as displacements, strains and stresses obtained by means of numerical methods, e.g. FEM.

In this section, the choice of the auxiliary fields is discussed thoroughly. Then, three alternative formulations owing to nonhomogeneous materials are derived and presented in conjunction with the auxiliary fields.

1.3.1 The Choice of Auxiliary Fields

An appropriate choice of auxiliary fields leads to the computation of SIFs by means of the interaction integral or M-integral. The auxiliary fields should be suitably defined and contain the quantities to be determined, i.e. K_I and K_{II}. Yau et al. [60] adopted Williams' solution [58] as the auxiliary fields to evaluate SIFs for a homogeneous cracked body. Dolbow and Gosz [15], Rao and Rahman [45], and Kim and Paulino [29] employed this same auxiliary fields for a nonhomogeneous cracked body under quasi-static conditions. Sladek et al. [51] defined the elastostatic field, i.e. $\sigma_{ij,j}^{aux} = 0$, as dynamic auxiliary field for the computation of T-stress of a homogeneous medium. In the present work, the asymptotic fields of Williams' solution [58] are employed as the auxiliary fields for dynamic nonhomogeneous materials, because the dynamic asymptotic fields of nonhomogeneous materials show similar behavior to those of quasi-static homogeneous materials around the crack tip locations [18, 22, 23, 42, 43].

The asymptotic auxiliary stress fields, defined according to the illustration in Fig. 1.2, are given by [2, 17]:

$$\sigma_{xx}^{aux} = \frac{K_I^{aux}}{\sqrt{2\pi r}} \cos\frac{\theta}{2}(1 - \sin\frac{\theta}{2}\sin\frac{3\theta}{2}) - \frac{K_{II}^{aux}}{\sqrt{2\pi r}} \sin\frac{\theta}{2}(2 + \cos\frac{\theta}{2}\cos\frac{3\theta}{2}) \tag{1.21}$$

$$\sigma_{yy}^{aux} = \frac{K_I^{aux}}{\sqrt{2\pi r}} \cos\frac{\theta}{2}(1 + \sin\frac{\theta}{2}\sin\frac{3\theta}{2}) + \frac{K_{II}^{aux}}{\sqrt{2\pi r}} \sin\frac{\theta}{2}\cos\frac{\theta}{2}\cos\frac{3\theta}{2} \tag{1.22}$$

$$\sigma_{xy}^{aux} = \frac{K_I^{aux}}{\sqrt{2\pi r}} \sin\frac{\theta}{2}\cos\frac{\theta}{2}\cos\frac{3\theta}{2} + \frac{K_{II}^{aux}}{\sqrt{2\pi r}} \cos\frac{\theta}{2}(1 - \sin\frac{\theta}{2}\sin\frac{3\theta}{2}), \tag{1.23}$$

and the corresponding auxiliary displacement fields are

$$u_x^{aux} = \frac{K_I^{aux}}{4\mu_{tip}}\sqrt{\frac{r}{2\pi}}\{(2\kappa - 1)\cos\frac{\theta}{2} - \cos\frac{3\theta}{2}\} + \frac{K_{II}^{aux}}{4\mu_{tip}}\sqrt{\frac{r}{2\pi}}\{(2\kappa + 3)\sin\frac{\theta}{2} + \sin\frac{3\theta}{2}\} \tag{1.24}$$

$$u_y^{aux} = \frac{K_I^{aux}}{4\mu_{tip}}\sqrt{\frac{r}{2\pi}}\{(2\kappa + 1)\sin\frac{\theta}{2} - \sin\frac{3\theta}{2}\} - \frac{K_{II}^{aux}}{4\mu_{tip}}\sqrt{\frac{r}{2\pi}}\{(2\kappa - 3)\cos\frac{\theta}{2} + \cos\frac{3\theta}{2}\}, \tag{1.25}$$

where μ_{tip} is the shear modulus at the crack tip, κ is given by

$$\kappa = \begin{cases} 3 - 4\mu & \text{Plane Strain} \\ (3-\mu)/(1+\mu) & \text{Plane Stress} \end{cases} \tag{1.26}$$

and K_I^{aux} and K_{II}^{aux} are the auxiliary mode I and mode II SIFs, respectively.

As mentioned earlier, the asymptotic fields of Williams' solution [58] are selected as the auxiliary fields to evaluate DSIFs in conjunction with the M-integral in this work. When a finite domain is chosen to evaluate the M-integral, however, these auxiliary fields cannot hold except for the crack tip location due to nonhomogeneous material properties. This aspect is noticeable when auxiliary fields are evaluated at finite distances from the crack tip. As a consequence, extra terms appear in the formulation to compensate for the difference in response owing to material nonhomogeneity.

1.3.2 Three Formulations

Due to the difference between material properties at the crack tip and away from the tip, three different additional formulations, which are non-equilibrium, incompatibility and constant constitutive tensor, are derived. The additional terms and the corresponding formulations for nonhomogeneous materials have been discussed by various researchers. Dolbow and Gosz [15] proposed the incompatibility formulation and used this formulation to ob-

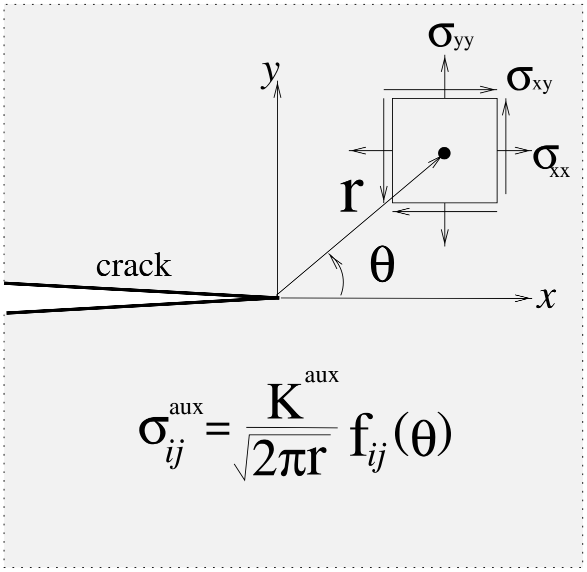

Figure 1.2: Williams' [58] solution for SIF evaluation. Here x and y indicate the local coordinate system.

tain SIFs for an arbitrarily oriented crack in FGMs using the extended FEM. They also discussed non-equilibrium and constitutive tensor formulations. Rao and Rahman [45] employed the constant constitutive tensor and the incompatibility formulations to evaluate SIFs for FGMs by means of the Element Free Galerkin (EFG). Kim and Paulino [29] proposed the non-equilibrium formulation to determine SIFs for various cracked FGMs in conjunction with FEM. Theoretically, this non-equilibrium formulation is equivalent to the incompatibility formulation and the constant constitutive tensor formulation. In this work, the non-equilibrium term and the corresponding non-equilibrium formulation are used in conjunction with FEM to determine SIFs for arbitrarily oriented cracks in nonhomogeneous materials under dynamic loading.

Non-Equilibrium Formulation

The field quantities from Williams' solution such as displacements, strains and stresses should be evaluated properly in order to be valid as the auxiliary fields. But all quantities can not be used at the same time because they are valid at the crack tip location and not valid at other points due to nonhomogeneity. Therefore, only two quantities can be selected from Williams' solution and the other quantity is obtained by considering material nonhomogeneity.

In this formulation, the auxiliary displacements and strains are obtained directly from Williams' solution and the auxiliary stresses are evaluated from the nonhomogeneous constitutive model. The auxiliary displacement is given by Eqs.(1.24) and (1.25). Then auxiliary strain fields are obtained using the relation between strain and displacement:

$$\varepsilon_{ij}^{aux} = \frac{1}{2}(u_{i,j}^{aux} + u_{j,i}^{aux}). \tag{1.27}$$

Finally, the auxiliary stress is obtained from

$$\sigma_{ij}^{aux} = C_{ijkl}(\boldsymbol{x})\varepsilon_{kl}^{aux}, \tag{1.28}$$

where $C_{ijkl}(\boldsymbol{x})$ is a constitutive tensor which vary spatially.

Since displacement and strains are obtained from the Williams' solutions directly, the compatibility condition is satisfied. However, the auxiliary stress field does not satisfy the equilibrium equation, i.e., $\sigma_{ij,j}^{aux} \neq 0$, because the constitutive tensor consists of material properties, which are functions of location. This condition will lead to a non-equilibrium term in the formulation.

Incompatibility Formulation

The auxiliary displacements and stresses are obtained from Williams' solutions and the auxiliary strain is obtained from the the constitutive model. The auxiliary stress and displacement fields are given by Eqs.(1.21) to (1.25), and the auxiliary strain field is obtained from

$$\varepsilon_{ij}^{aux} = S_{ijkl}(\boldsymbol{x})\sigma_{kl}^{aux}, \tag{1.29}$$

where $S_{ijkl}(\boldsymbol{x})$ is the compliance tensor of the nonhomogeneous material.

In this formulation, the equilibrium condition, $\sigma_{ij,j}^{aux} = 0$, is satisfied because stress fields of Williams' solution are employed. However, the auxiliary displacement and strain fields violate the compatibility condition, $\varepsilon_{ij}^{aux} \neq \frac{1}{2}(u_{i,j}^{aux} + u_{j,i}^{aux})$, because the displacement field is based on constant material properties, and the strain is obtained considering material gradient effects, $S(\boldsymbol{x})$, as expressed in Eq. (1.29). This condition will lead to an incompatibility term in the formulation.

Constant Constitutive Tensor Formulation

In this formulation, the displacement and stress fields are selected from Williams' solution, and the strain field is obtained from the following relationship,

$$\varepsilon_{ij}^{aux} = (S_{ijkl})_{tip}\sigma_{kl}^{aux}, \tag{1.30}$$

where $(S_{ijkl})_{tip}$ is a constant compliance tensor based on the material properties at the crack tip. Since the compliance tensor is defined at the crack tip, the constitutive relationship is valid at the crack tip and is not valid at other points. This condition will lead to a correction term associated to the constitutive properties of the material.

Chapter 2

Theoretical Formulation

Since the J-integral was presented by Rice [46], this method has been widely used in evaluating SIFs for various problems and has been a basis for new methods such as the $\hat{J}$ integral where decomposition procedures are employed to determine mixed-mode SIFs. The interaction integral, which is used to evaluate DSIFs for nonhomogeneous materials, is also based on the J-integral. Therefore, a generalized J-integral is derived and explained. Then, three formulations of the interaction integral are presented considering non-equilibrium, incompatibility and constant constitutive tensor terms, which follow the description given in Chapter 1.

2.1 Generalized J-Integral

An equilibrium equation can be expressed with zero body force as follows [2, 38, 40]:

$$\sigma_{ij,j} = \rho \ddot{u}_i, \tag{2.1}$$

where ρ is mass density and each dot indicates a derivative with respect to time. Taking inner product of both sides with velocity and rearranging the result, one obtains

$$(\sigma_{ij}\dot{u}_i)_{,j} = \rho \ddot{u}_i \dot{u}_i + \sigma_{ij}\dot{u}_{i,j} = \dot{L} + \dot{W}, \tag{2.2}$$

where L and W are kinetic energy and strain energy density, respectively, and are given by

$$W = \int_0^t \sigma_{ij}\dot{\varepsilon}_{ij} dt, \ L = \int_0^t \rho \ddot{u}_i \dot{u}_i dt. \tag{2.3}$$

Equation (2.2), which is a strong form of energy balance, is a generalized balance law.

Transforming from local to global form, and applying the divergence theorem, one obtains

$$\int_{\partial\Omega} \sigma_{ij} u_i m_j dA = \int_{\Omega} (\dot{L} + \dot{W}) dV, \tag{2.4}$$

where Ω is volume, $\partial\Omega$ is the surface, and m_j is the outward normal vector of the surface. Equation (2.4) is a weak form of energy balance. Applying Reynolds Transport theorem to Eq.(2.4), one obtains

$$\int\limits_{\partial\Omega} (\sigma_{ij} \dot{u}_i m_j) dA = \frac{d}{dt} \int\limits_{\Omega} (L + W) dV - \int\limits_{\partial\Omega} (L + W) V_j m_j dA, \tag{2.5}$$

where V_j is the instantaneous velocity of $\partial\Omega$.

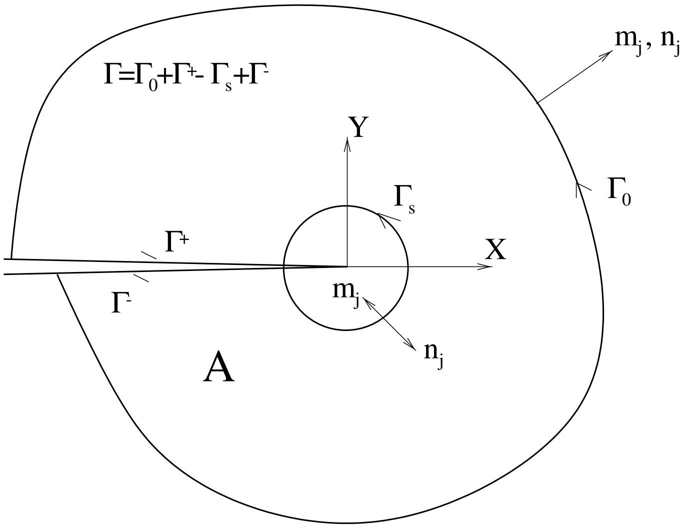

Figure 2.1: Domain with the crack tip which propagates with a constant speed, V. The area A is enclosed by Γ, the normal vector is $m_j = n_j$ on Γ_0, Γ^+ and Γ^-, and $m_j = -n_j$ on Γ_s.

In order to apply the above energy balance law, i.e. Eq.(2.5), to planar crack propagation problems, let's consider a 2D domain with a crack which is oriented along the X axis. The contour Γ_0 is fixed in space, and the inner contour Γ_s is fixed in size and translates with a constant speed, V. The area A enclosed by $\Gamma = \Gamma_o + \Gamma^+ - \Gamma_s + \Gamma^-$ is free of singularity as illustrated in Figure 2.1. Crack faces are assumed to be traction free. Therefore, Eq. (2.5) becomes

$$\int\limits_{\Gamma_0} t_i \dot{u}_i d\Gamma = \frac{d}{dt} \int\limits_{A} (W + L) dA - \int\limits_{\Gamma_s} \left[(W + L) V \delta_{1j} + \sigma_{ij} \dot{u}_i \right] m_j d\Gamma, \tag{2.6}$$

where $t_i = \sigma_{ij} n_j$ and δ_{1j} denotes the Kronecker delta. The term on the left hand side of Eq. (2.6) is the rate of energy input into the body. The first term and second term on the right hand side of Eq. (2.6) are the rate of increase in internal energy and the instantaneous rate of energy at which energy is lost due to flux of internal energy into the crack tip region, respectively [2]. By using $m_j = -n_j$ on Γ_s, one rewrites the instantaneous rate of energy as

$$F(\Gamma) = \int\limits_{\Gamma_s} \left[(W + L)V\delta_{1j} + \sigma_{ij}\dot{u}_i\right] n_j d\Gamma. \tag{2.7}$$

In order for Eq. (2.7) to have significance in fracture mechanics, the fundamental property of path-independence should be satisfied. For evaluation of path-independence, let's consider two different contours Γ_1 and Γ_2 as illustrated in Figure 2.2. Application of the divergence theorem to Eq. (2.7) leads to

$$F(\Gamma_2) - F(\Gamma_1) = \int_{A_{12}} (\sigma_{ij}\dot{u}_i + (L + W)V\delta_{1j})_{,j}\ dA, \tag{2.8}$$

where A_{12} indicates the area between the contour Γ_1 an Γ_2.

Differentiating Eq. (2.8) and substituting Eq. (2.2) into the result, one obtains

$$\begin{aligned} F(\Gamma_2) - F(\Gamma_1) &= \int_{A_{12}} [(\dot{L} + \dot{W}) + (L + W)_{,1}V]dA \\ &= \int_{A_{12}} [(\dot{W} + VW_{,1}) + (\dot{L} + VL_{,1})]dA. \end{aligned} \tag{2.9}$$

In order to obtain path independence, Eq. (2.9) must be zero. Therefore, the path independence is satisfied if

$$\frac{\partial f}{\partial t} + V\frac{\partial f}{\partial x_1} = 0, \tag{2.10}$$

where f is a field variable. If the crack propagates with constant speed, which is the definition of steady state condition, Eq. (2.10) is satisfied.

The dynamic energy release rate, which is equal to J-integral under linear elastic condition, is defined as F/V as the contour Γ_s shrinks to the crack tip. Under the steady state condition, the energy release rate becomes

$$J = G = \lim_{\Gamma_s \to 0} \frac{d\Pi}{dA} = \lim_{\Gamma_s \to 0} \frac{F(\Gamma)}{V} = \lim_{\Gamma_s \to 0} \int\limits_{\Gamma_s} [(W + L)\delta_{1j} - \sigma_{ij}u_{i,1}]n_j d\Gamma. \tag{2.11}$$

Equation (2.11), so called generalized J-integral, is applicable to static and to dynamic problems with a constant crack tip speed to evaluate the energy required for a crack to propagate.

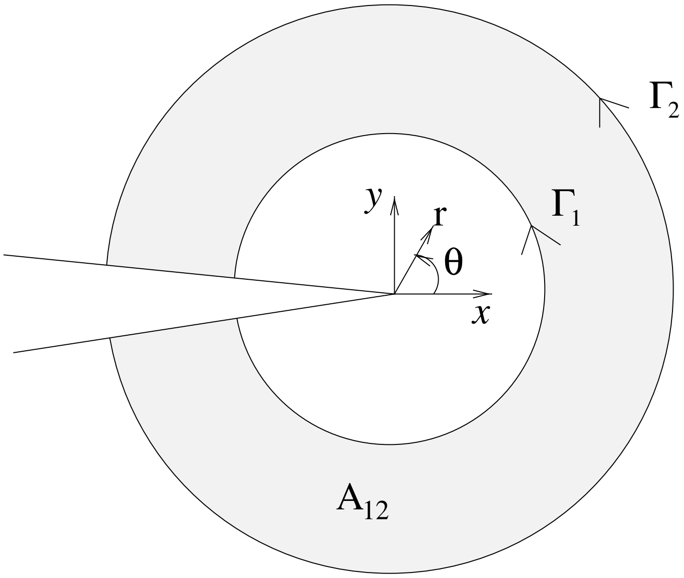

Figure 2.2: The domain enclosed by two different contours Γ_1 and Γ_2. A_{12} indicates the domain enclosed by Γ_1, Γ_2 and crack faces.

Equation (2.11) reduces to the following form under stationary condition, i.e. V=0,

$$J = \lim_{\Gamma_s \to 0} \int_{\Gamma_s} (W\delta_{1j} - \sigma_{ij} u_{i,1}) n_j d\Gamma, \tag{2.12}$$

because the kinetic energy L, a function of crack tip speed, is zero under the stationary condition, and thus

$$L = \frac{1}{2}\rho \dot{u}_i \dot{u}_i = \frac{1}{2}\rho(-V\frac{\partial u}{\partial x})^2 = 0. \tag{2.13}$$

So, the kinetic energy does not contribute to the J-integral. This statement is numerically observed by Vargas and Dodds [54] who determined the dynamic J integral for impact fracture testing. They concluded that the kinetic energy contribution is less than 0.1 percent to the total J integral.

2.2 Interaction Integral Formulation

Assuming that the crack faces are traction-free and using the q function (q is 1 on Γ_s and 0 on Γ_0) according to Figure 2.3, one rewrites the generalized J-integral from Eq. (2.12), i.e.

$$J = \lim_{\Gamma_s \to 0} \int_{\Gamma_s} (W\delta_{1j} - \sigma_{ij} u_{i,1}) n_j d\Gamma = -\lim_{\Gamma_s \to 0} \oint_{\Gamma} (W\delta_{1j} - \sigma_{ij} u_{i,1}) m_j q d\Gamma, \tag{2.14}$$

where $\Gamma = \Gamma_o + \Gamma^+ - \Gamma_s + \Gamma^-$, m_j is a unit normal vector to the contour (Γ), as illustrated in Figure 2.4. Application of the divergence theorem to Eq. (2.14) leads to the equivalent domain integral (EDI) [44] as follows:

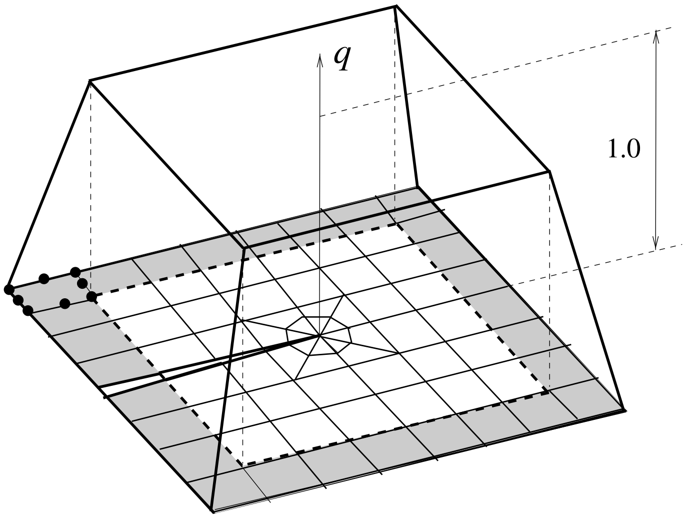

Figure 2.3: The q function (plateau weight function).

$$J = \int_A (\sigma_{ij} u_{i,1} - W\delta_{1j}) q_{,j} \; dA + \int_A (\sigma_{ij} u_{i,1} - W\delta_{1j})_{,j} q \; dA. \tag{2.15}$$

Considering the following relationships, which can be applied for general cases including material gradient and dynamic effects,

$$W_{,1} = \frac{1}{2}\sigma_{ij,1}\varepsilon_{ij} + \frac{1}{2}\sigma_{ij}\varepsilon_{ij,1} \tag{2.16}$$

and

$$(\sigma_{ij} u_{i,1})_{,j} = \sigma_{ij,j} u_{i,1} + \sigma_{ij} u_{i,1j}, \tag{2.17}$$

one obtains the following expression:

$$J = \int_A (\sigma_{ij} u_{i,1} - W\delta_{1j}) q_{,j} dA + \int_A (\sigma_{ij,j} u_{i,1} + \sigma_{ij} u_{i,1j} - \frac{1}{2}\sigma_{ij,1}\varepsilon_{ij} - \frac{1}{2}\sigma_{ij}\varepsilon_{ij,1}) q dA, \tag{2.18}$$

which is modified as

$$J = \int_A (\sigma_{ij} u_{i,1} - W\delta_{1j}) q_{,j} dA + \int_A (\rho \ddot{u}_i u_{i,1} - \frac{1}{2} C_{ijkl,1}\varepsilon_{ij}\varepsilon_{kl}) q dA, \tag{2.19}$$

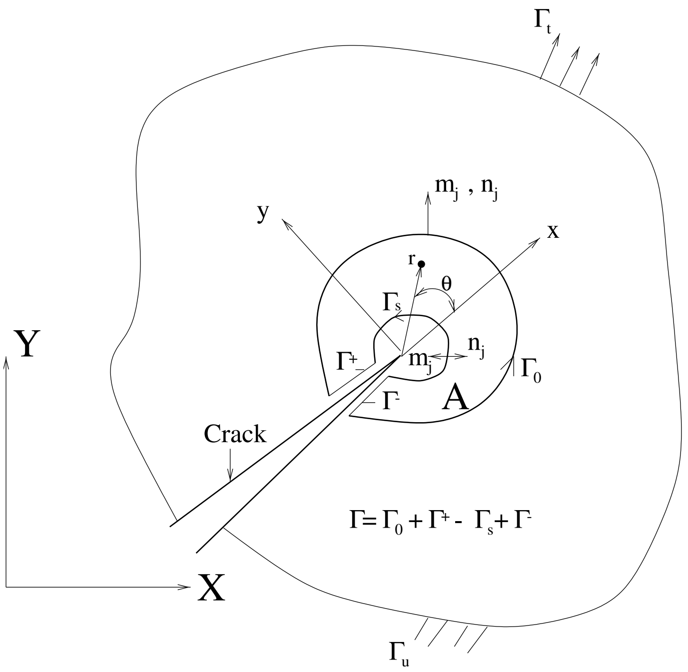

Figure 2.4: Transformation from line integral to equivalent domain integral (EDI). Notice that the normal vector $m_j = n_j$ for Γ_0, Γ^+ and Γ^-, and $m_j = -n_j$ on Γ_s.

using the following equalities:

$$\begin{aligned} \sigma_{ij,j} &= \rho \ddot{u}_i, \\ \sigma_{ij,1}\varepsilon_{ij} &= \left(C_{ijkl}\varepsilon_{kl}\right)_{,1}\varepsilon_{ij} = \left(C_{ijkl,1}\varepsilon_{kl}\varepsilon_{ij} + \sigma_{ij}\varepsilon_{ij,1}\right), \\ \sigma_{ij}u_{i,1j} &= \sigma_{ij}\varepsilon_{ij,1}, \end{aligned} \tag{2.20}$$

where C_{ijkl} denotes the elasticity tensor. Notice that Eq. (2.19) is the extended J*-integral under the stationary condition*. Equation (2.19) is reduced to the J-integral for the static nonhomogeneous material case as derived by Kim and Paulino [27]. Besides, for homogeneous materials, Eq. (2.19) is identical to the one derived by Moran et al. [38] under the stationary condition, i.e. V=0.

Superimposing the actual and auxiliar fields on Eq. (2.18), one obtains

$$\begin{aligned} J &= \int_A \left\{ (\sigma_{ij}^{aux} + \sigma_{ij})(u_{i,1}^{aux} + u_{i,1}) - \frac{1}{2}(\sigma_{ik}^{aux} + \sigma_{ik})(\varepsilon_{ik}^{aux} + \varepsilon_{ik})\delta_{1j} \right\} q_{,j} dA \\ &+ \int_A \left\{ (\sigma_{ij,j}^{aux} + \sigma_{ij,j})(u_{i,1}^{aux} + u_{i,1}) + (\sigma_{ij}^{aux} + \sigma_{ij})(u_{i,1j}^{aux} + u_{i,1j}) \right\} q dA \\ &- \frac{1}{2}\int_A \left\{ (\sigma_{ij,1}^{aux} + \sigma_{ij,1})(\varepsilon_{ij}^{aux} + \varepsilon_{ij}) + (\sigma_{ij}^{aux} + \sigma_{ij})(\varepsilon_{ij,1}^{aux} + \varepsilon_{ij,1}) \right\} q dA, \end{aligned} \tag{2.21}$$

which is decomposed into

$$J^s = J + J^{aux} + M, \tag{2.22}$$

where J and J^{aux} are given by

$$\begin{aligned} J &= \int_A (\sigma_{ij} u_{i,1} - \frac{1}{2}\sigma_{ik}\varepsilon_{ik}\delta_{1j}) q_{,j} dA \\ & \int_A (\sigma_{ij,j} u_{i,1} + \sigma_{ij} u_{i,1j} - \frac{1}{2}\sigma_{ij,1}\varepsilon_{ij} - \frac{1}{2}\sigma_{ij}\varepsilon_{ij,1}) q dA, \end{aligned} \tag{2.23}$$

$$\begin{aligned} J^{aux} &= \int_A (\sigma_{ij}^{aux} u_{i,1}^{aux} - \frac{1}{2}\sigma_{ik}^{aux}\varepsilon_{ik}^{aux}\delta_{1j}) q_{,j} dA \\ & \int_A (\sigma_{ij,j}^{aux} u_{i,1}^{aux} + \sigma_{ij}^{aux} u_{i,1j}^{aux} - \frac{1}{2}\sigma_{ij,1}^{aux}\varepsilon_{ij}^{aux} - \frac{1}{2}\sigma_{ij}^{aux}\varepsilon_{ij,1}^{aux}) q dA, \end{aligned} \tag{2.24}$$

respectively. The resulting M integral is given by

$$\begin{aligned} M &= \int_A \left\{ (\sigma_{ij}^{aux} u_{i,1} + \sigma_{ij} u_{i,1}^{aux}) - \frac{1}{2}(\sigma_{ik}^{aux}\varepsilon_{ik} + \sigma_{ik}\varepsilon_{ik}^{aux})\delta_{1j} \right\} q_{,j} dA \\ &+ \int_A \left\{ (\sigma_{ij,j}^{aux} u_{i,1} + \sigma_{ij,j} u_{i,1}^{aux}) + (\sigma_{ij}^{aux} u_{i,1j} + \sigma_{ij} u_{i,1j}^{aux}) \right\} q dA \\ &- \frac{1}{2}\int_A \left\{ (\sigma_{ij,1}^{aux}\varepsilon_{ij} + \sigma_{ij,1}\varepsilon_{ij}^{aux}) + (\sigma_{ij}^{aux}\varepsilon_{ij,1} + \sigma_{ij}\varepsilon_{ij,1}^{aux}) \right\} q dA. \end{aligned} \tag{2.25}$$

2.2.1 Non-equilibrium Formulation

This formulation creates the non-equilibrium terms explained in Section 1.3.1. Since the actual fields employ the quantities obtained from numerical simulation, the equilibrium and compatibility condition are satisfied, i.e.,

$$\sigma_{ij,j} = \rho \ddot{u}_i \tag{2.26}$$

$$\varepsilon_{ij} = \frac{1}{2}(u_{i,j} + u_{j,i}), \quad \sigma_{ij} u_{i,1j} = \sigma_{ij}\varepsilon_{ij,1}. \tag{2.27}$$

For the auxiliary fields, the equilibrium condition is not satisfied, i.e.,

$$\sigma_{ij,j}^{aux} \neq 0, \tag{2.28}$$

while the relation between strain and displacement are compatible:

$$\varepsilon_{ij}^{aux} = \frac{1}{2}(u_{i,j}^{aux} + u_{j,i}^{aux}), \quad \sigma_{ij} u_{i,1j}^{aux} = \sigma_{ij}\varepsilon_{ij,1}^{aux}. \tag{2.29}$$

Notice that the auxiliary fields are chosen as asymptotic fields for static homogeneous materials as explained in Section 1.3. For the superimposed actual and auxiliary fields, the following equalities are obtained:

$$\sigma_{ij}\varepsilon_{ij}^{aux} = C_{ijkl}(\boldsymbol{x})\varepsilon_{kl}\varepsilon_{ij}^{aux} = \sigma_{kl}^{aux}\varepsilon_{kl} = \sigma_{ij}^{aux}\varepsilon_{ij}, \tag{2.30}$$

$$C_{ijkl,1}(\boldsymbol{x})\varepsilon_{kl}^{aux}\varepsilon_{ij} = C_{ijkl,1}(\boldsymbol{x})\varepsilon_{ij}^{aux}\varepsilon_{kl}, \tag{2.31}$$

$$C_{ijkl}(\boldsymbol{x})\varepsilon_{kl,1}\varepsilon_{ij}^{aux} = \sigma_{ij}^{aux}\varepsilon_{ij,1}, \tag{2.32}$$

$$C_{ijkl}(\boldsymbol{x})\varepsilon_{kl,1}^{aux}\varepsilon_{ij} = \sigma_{ij}\varepsilon_{ij,1}^{aux}. \tag{2.33}$$

Substitution of Eqs. (2.26) and (2.30) into Eq. (2.25) leads to

$$\begin{aligned} M &= \int_A \left\{(\sigma_{ij}^{aux}u_{i,1} + \sigma_{ij}u_{i,1}^{aux}) - \sigma_{ik}^{aux}\varepsilon_{ik}\delta_{1j}\right\} q_{,j}\ dA \\ &+ \int_A \left\{\sigma_{ij,j}^{aux}u_{i,1} + \rho\ddot{u}_i u_{i,1}^{aux} + (\sigma_{ij}^{aux}u_{i,1j} + \sigma_{ij}u_{i,1j}^{aux})\right\}\ qdA \\ &- \frac{1}{2}\int_A \left\{(\sigma_{ij,1}^{aux}\varepsilon_{ij} + \sigma_{ij,1}\varepsilon_{ij}^{aux}) + (\sigma_{ij}^{aux}\varepsilon_{ij,1} + \sigma_{ij}\varepsilon_{ij,1}^{aux})\right\}\ qdA. \end{aligned} \tag{2.34}$$

Since $\sigma_{ij}^{aux} = C_{ijkl}(\boldsymbol{x})\varepsilon_{kl}^{aux}$, then $\sigma_{ij,1}^{aux}\varepsilon_{ij}$ can be expressed by

$$\sigma_{ij,1}^{aux}\varepsilon_{ij} = (C_{ijkl}(\boldsymbol{x})\varepsilon_{kl}^{aux})_{,1}\varepsilon_{ij} = (C_{ijkl,1}(\boldsymbol{x})\varepsilon_{kl}^{aux} + C_{ijkl}(\boldsymbol{x})\varepsilon_{kl,1}^{aux})\varepsilon_{ij} \tag{2.35}$$

and the expression $\sigma_{ij,1}\varepsilon_{ij}^{aux}$ is given by

$$\sigma_{ij,1}\varepsilon_{ij}^{aux} = (C_{ijkl}(\boldsymbol{x})\varepsilon_{kl})_{,1}\varepsilon_{ij}^{aux} = (C_{ijkl,1}(\boldsymbol{x})\varepsilon_{kl} + C_{ijkl}(\boldsymbol{x})\varepsilon_{kl,1})\varepsilon_{ij}^{aux}. \tag{2.36}$$

Substituting Eqs. (2.35) and (2.36) into (2.34) and using the equality of Eqs. (2.31), (2.32) and (2.33), one obtains

$$\begin{aligned} M &= \int_A \left\{(\sigma_{ij}^{aux}u_{i,1} + \sigma_{ij}u_{i,1}^{aux}) - \sigma_{ik}^{aux}\varepsilon_{ik}\delta_{1j}\right\} q_{,j}dA \\ &+ \int_A \left\{\sigma_{ij,j}^{aux}u_{i,1} + \rho\ddot{u}_i u_{i,1}^{aux} - C_{ijkl,1}\varepsilon_{kl}^{aux}\varepsilon_{ij}\right\} qdA, \end{aligned} \tag{2.37}$$

where $\sigma_{ij,j}^{aux}u_{i,1}$, $\rho\ddot{u}_i u_{i,1}^{aux}$, and $C_{ijkl,1}\varepsilon_{kl}^{aux}\varepsilon_{ij}$ appear due to non-equilibrium of the auxiliary fields, dynamic effect of the actual fields, and nonhomogeneous effects of the actual fields, respectively. If dynamic effects are ignored, this equation reduces to the interaction integral for the static nonhomogeneous material case derived by Kim and Paulino [30].

2.2.2 Incompatibility Formulation

This formulation creates the incompatibility terms explained in Section 1.3.2. For the actual field, the equilibrium and compatibility conditions are

$$\sigma_{ij,j} = \rho \ddot{u}_i, \tag{2.38}$$

$$\varepsilon_{ij} = \frac{1}{2}(u_{i,j} + u_{j,i}), \quad \sigma_{ij} u_{i,1j} = \sigma_{ij} \varepsilon_{ij,1}. \tag{2.39}$$

In this formulation, the equilibrium condition is satisfied,

$$\sigma_{ij,j}^{aux} = 0, \tag{2.40}$$

while the relation of between strain and displacement are not compatible:

$$\varepsilon_{ij}^{aux} \neq \frac{1}{2}(u_{i,j}^{aux} + u_{j,i}^{aux}). \tag{2.41}$$

For the superimposed field of actual and auxiliary field, the following equality is obtained as

$$\begin{aligned} \sigma_{ij}\varepsilon_{ij}^{aux} = C_{ijkl}(\boldsymbol{x})\varepsilon_{kl}\varepsilon_{ij}^{aux} = \sigma_{kl}^{aux}\varepsilon_{kl} = \sigma_{ij}^{aux}\varepsilon_{ij}, \\ C_{ijkl,1}(\boldsymbol{x})\varepsilon_{kl}^{aux}\varepsilon_{ij} = C_{ijkl,1}(\boldsymbol{x})\varepsilon_{ij}^{aux}\varepsilon_{kl}, \\ C_{ijkl}(\boldsymbol{x})\varepsilon_{kl,1}\varepsilon_{ij}^{aux} = \sigma_{ij}^{aux}\varepsilon_{ij,1}, \\ C_{ijkl}(\boldsymbol{x})\varepsilon_{kl,1}^{aux}\varepsilon_{ij} = \sigma_{ij}\varepsilon_{ij,1}^{aux}. \end{aligned} \tag{2.42}$$

Using Eqs. (2.38) through (2.42), one obtains

$$\begin{aligned} M &= \int_A \left\{ (\sigma_{ij}^{aux} u_{i,1} + \sigma_{ij} u_{i,1}^{aux}) - \sigma_{ik}^{aux} \varepsilon_{ik} \delta_{1j} \right\} q_{,j} dA \\ &+ \int_A \left\{ \sigma_{ij}(u_{i,1j}^{aux} - \varepsilon_{ij,1}^{aux}) + \rho \ddot{u}_i u_{i,1}^{aux} - C_{ijkl,1} \varepsilon_{kl}^{aux} \varepsilon_{ij} \right\} q dA, \end{aligned} \tag{2.43}$$

where $\sigma_{ij}(u_{i,1j}^{aux} - \varepsilon_{ij,1}^{aux})$, $\rho \ddot{u}_i u_{i,1}^{aux}$, and $C_{ijkl,1}\varepsilon_{kl}^{aux}\varepsilon_{ij}$ appear due to incompatibility of the auxiliary fields, dynamic effect of the actual fields, and nonhomogeneous effects of the actual fields, respectively.

2.2.3 Constant-constitutive-tensor Formulation

This formulation generates the constant constitutive tensor terms explained in Section 1.3.3. Actual fields satisfy the equilibrium and compatibility condition:

$$\sigma_{ij,j} = \rho \ddot{u}_i, \tag{2.44}$$

$$\varepsilon_{ij} = \frac{1}{2}(u_{i,j} + u_{j,i}), \quad \sigma_{ij} u_{i,1j} = \sigma_{ij} \varepsilon_{ij,1}. \tag{2.45}$$

While auxiliary fields satisfy the equilibrium and compatibility condition, they violate the constitutive relationship, i.e.

$$\sigma^{aux}_{ij,j} = 0, \tag{2.46}$$

$$\varepsilon^{aux}_{ij} = \frac{1}{2}(u^{aux}_{i,j} + u^{aux}_{j,i}), \tag{2.47}$$

$$\sigma^{aux}_{ij} = (C_{ijkl})_{tip} \varepsilon^{aux}_{kl}, \quad (C_{ijkl})_{tip} \neq C_{ijkl}(\boldsymbol{x}). \tag{2.48}$$

Therefore, Eq. (2.42) is not valid any more.

Substituting Eqs. (2.44) through (2.47) leads to

$$\begin{aligned} M \; &= \int_A \left\{ (\sigma^{aux}_{ij} u_{i,1} + \sigma_{ij} u^{aux}_{i,1}) - \frac{1}{2}(\sigma^{aux}_{ik} \varepsilon_{ik} + \sigma_{ik} \varepsilon^{aux}_{ik}) \delta_{1j} \right\} q_{,j} dA \\ &+ \int_A \left\{ \rho \ddot{u}_i u^{aux}_{i,1} - \frac{1}{2}(\sigma^{aux}_{ij,1} \varepsilon_{ij} - \underline{\sigma_{ij,1}} \varepsilon^{aux}_{ij} + \sigma^{aux}_{ij} \underline{\varepsilon_{ij,1}} - \sigma_{ij} \varepsilon^{aux}_{ij,1}) \right\} q dA \end{aligned} \tag{2.49}$$

From a numerical point of view, due to derivatives of the actual stress and strain fields (underlined terms), the accuracy might not be as good as the two previous formulations.

2.2.4 Extraction of SIFs

The actual and auxiliary relationship between J and mixed mode SIFs are, respectively

$$J_{local} = \frac{K_I^2 + K_{II}^2}{E^*_{tip}}, \tag{2.50}$$

$$J^{aux}_{local} = \frac{(K^{aux}_I)^2 + (K^{aux}_{II})^2}{E^*_{tip}} \tag{2.51}$$

where

$$E^*_{tip} = \begin{cases} E_{tip} & \text{Plane Stress} \\ E_{tip}/(1 - \upsilon^2_{tip}) & \text{Plane Strain} \end{cases} \tag{2.52}$$

For the superimposed fields of actual and auxiliary fields, the relationship between J and

SIFs of actual and auxiliary field is obtained as:

$$\begin{aligned} J^{s}_{local} &= \frac{(K_I + K_I^{aux})^2 + (K_{II} + K_{II}^{aux})^2}{E^*_{tip}} \\ &= J_{local} + J^{aux}_{local} + M, \end{aligned} \tag{2.53}$$

where

$$M_{local} = \frac{2}{E^*_{tip}}(K_I K_I^{aux} + K_{II} K_{II}^{aux}). \tag{2.54}$$

Using judicious choice of auxiliary modes I and II SIFs, the SIFs of actual field is decoupled and determined as:

$$K_I = \frac{E^*_{tip}}{2} M_{local} \quad (K_I^{aux} = 1,\ K_{II}^{aux} = 0), \tag{2.55}$$

$$K_{II} = \frac{E^*_{tip}}{2} M_{local} \quad (K_I^{aux} = 0,\ K_{II}^{aux} = 1). \tag{2.56}$$

The relationship between SIFs and M-integral, i.e. Eqs. (2.55) and (2.56), is identical with those for homogeneous materials [60], except that the material properties are sampled at the crack tip location for nonhomogeneous materials.

Chapter 3

Numerical Implementation

To investigate dynamic fracture behavior under different material gradients by means of the FEM, a dynamic finite element code considering nonhomogeneous materials in conjunction with the Newmark β method was developed. The M-integral, which is used to obtain DSIFs, was also implemented in the code. In this section, the concept of isoparametric finite element formulation for incorporating nonhomogeneous material properties at the element level is addressed. The dynamic finite element formulation, the Newmark β method, and the M-integral implementation are explained below.

3.1 Generalized Isoparametric Formulation (GIF)

To incorporate material nonhomogeneity, we can use either graded elements or homogeneous elements. Graded elements incorporate the material property gradient at the size scale of the element, while the homogeneous element produces a stepwise constant approximation to a continuous material property field such as the one shown in Figure 3.1. It is clearly observed that graded elements approximate the real material gradations better than homogeneous elements. The difference of numerical results using two different schemes can be more distinct for relatively coarse meshes where the material gradation is steep. Kim and Paulino [28] investigated the performance of both elements for nonhomogeneous materials where material gradations are either parallel or perpendicular to the applied external loading such as bending, tension and fixed grip loading. Buttlar et al. [7] applied both schemes in pavement systems where material gradations occur due to temperature gradients and aging related stiffness gradients. They implemented the graded elements using the UMAT [1] capability of the finite element software ABAQUS. The authors of both works concluded that graded elements lead to more accurate unaveraged stress along the interface where material properties are not continuous. So, the use of graded elements are more desirable for

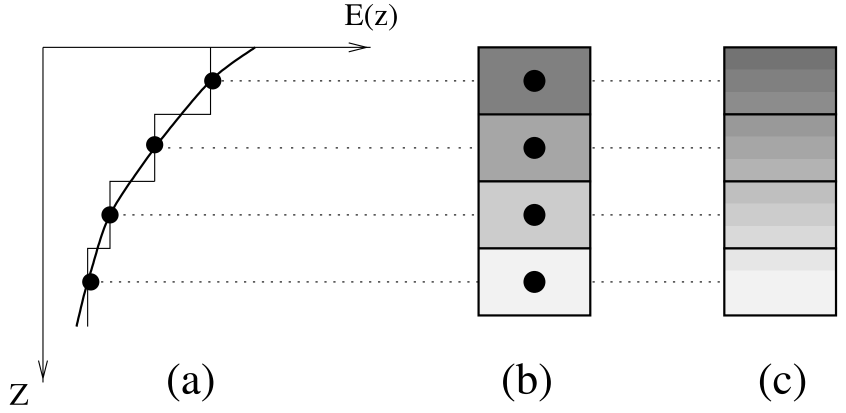

Figure 3.1: Homogeneous versus graded finite elements: (a) property variation along one coordinate axis; (b) homogeneous elements; (c) graded elements. Notice that the property of the homogeneous elements corresponds to the property at the centroids of the graded elements.

nonhomogeneous materials than standard homogeneous elements (see Figure 3.1).

The *Generalized Isoparametric Formulation* (GIF) of Kim and Paulino [28] consists of interpolating geometry, displacements and material properties from nodal points. Thus, material properties such as elastic modulus (E), Poisson's ratio (ν), and mass density (ρ) at Gauss points can be interpolated using shape functions from nodal points as illustrated in Figure 3.2.

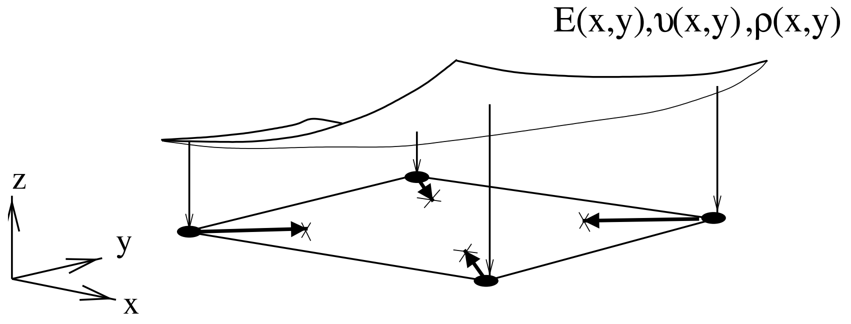

Figure 3.2: Generalized isoparametric formulation (GIF) [28].

The interpolation procedure is summarized as follows [12, 28]:

$$\text{Displacements} \quad : \quad u = \sum_i u_i \mathrm{N}_i(\xi,\eta), \quad v = \sum_i v_i \mathrm{N}_i(\xi,\eta) \tag{3.1}$$

$$\text{Coordinates} \quad : \quad x = \sum_i x_i \mathrm{N}_i(\xi,\eta), \quad y = \sum_i y_i \mathrm{N}_i(\xi,\eta) \tag{3.2}$$

$$\text{Material properties} \quad : \quad E = \sum_i E_i \mathrm{N}_i(\xi,\eta), \quad \nu = \sum_i \nu_i \mathrm{N}_i(\xi,\eta), \;\; \rho = \sum_i \rho_i \mathrm{N}_i(\xi,\eta) \tag{3.3}$$

where N_i are the shape functions, which are functions of the intrinsic coordinates ξ and η. This formulation is implemented in the present code.

Using the GIF, the finite element stiffness matrix relations for nonhomogeneous materials can be written as [26]

$$[\boldsymbol{K}^e]\,\{\boldsymbol{u}^e\} = \{\boldsymbol{F}^e\} \tag{3.4}$$

with

$$[\boldsymbol{K}^e] = \int_{\Omega_e} [\boldsymbol{B}^e]^T [\boldsymbol{D}^e(\boldsymbol{x})][\boldsymbol{B}^e] d\Omega_e, \tag{3.5}$$

where $\{\boldsymbol{u}^e\}$ is nodal displacement vector, $\{\boldsymbol{F}^e\}$ is the load vector, $[\boldsymbol{B}^e]$ is the strain-displacement matrix which contains gradients of the interpolating functions, $[\boldsymbol{D}^e(\boldsymbol{x})]$ is the constitutive matrix (variable), and Ω_e is the domain of element "e". In the present work, the elasticity matrix $[\boldsymbol{D}^e(\boldsymbol{x})]$= $[\boldsymbol{D}^e(x, y)]$ is assumed to be a function of spatial co-ordinates.

The integral in Eq. (3.5) is evaluated by Gauss quadrature, and the matrix $[\boldsymbol{D}^e(\boldsymbol{x})]$ is calculated at each Gaussian integration point. Thus for two-dimensional problems, the resulting integral becomes:

$$[\boldsymbol{K}^e] = \sum_{i=1}^{N} \sum_{j=1}^{N} [\boldsymbol{B}^e_{ij}]^T [\boldsymbol{D}^e_{ij}(\boldsymbol{x})][\boldsymbol{B}^e_{ij}] J_{ij} w_i w_j, \tag{3.6}$$

where the subscripts i and j refer to the Gaussian integration points, J_{ij} is the determinant of the Jacobian matrix, and w_i are the standard Gaussian weights.

3.2 Dynamic Finite Element Formulation

In addition to the implementation details discussed above, the dynamic FEM formulation is presented. It includes aspects such as the background, equilibrium equations, Newmark β method, and displacement control analysis.

3.2.1 Background

In general, if the lowest natural frequency of a structure is bigger than 4 times the frequency of excitation imposed on the structure, the inertia effect is not important which is so called quasistatic [13]. Otherwise, it should be taken into account in deriving a dynamic equilibrium equation.

Dynamic problems are divided into either wave propagation problems or structural dynamic problems [12]. In wave propagation problems, a loading is an impact or an explosive blast such that the duration of period is normally short. In this kind of problems, the influence of stress waves is of main interest. Problems of structural dynamics involve analyses of either time history or natural frequency of vibration. Two methods, modal method and direct integration method, are proposed in time history analysis. In general, the Newmark β methods are among direct integration methods frequently used in dynamic analysis. So, Newmark β methods are implemented here and used in order to obtain field quantities such as displacements, strains and stresses.

There are two distinct schemes of direct integration: an explicit scheme and an implicit scheme. In the explicit scheme, a current solution depends only on previous history information such as displacement, velocity and acceleration. Easy implementation and accurate treatment of general nonlinearities are the key advantages. However, compared to the implicit scheme it is conditionally stable. A central difference method is one of the popular explicit schemes. In the implicit scheme, a current solution depends on previous history information and current unknown information such that it is more computationally complicated than the explicit schemes. However it is unconditionally stable. An average acceleration method is one of the popular implicit methods [13].

Stiffness matrix [K], mass matrix [M], and damping matrix [C] are three major components in the dynamic equilibrium equation. The procedure for calculating the stiffness matrix in dynamic problems is exactly the same as that in static cases (see Section 3.1). In determining the mass matrix, consistent mass matrix and lumping mass matrix schemes are used. The consistent mass matrix uses the same shape functions as those for the stiffness matrix. The properties of the consistent mass matrix are non-diagonal, symmetric and positive definite. With implicit methods, this scheme is preferred for accuracy because the consistent mass matrix has the upper bound property for the frequency and the implicit method has an effect in decreasing the frequency. The lumping scheme is an effective method for producing a diagonal mass matrix. It is recommended for arbitrary elements. With explicit methods like the central difference method, the lumping scheme is preferred for accuracy and economy [12]. In calculating the damping matrix, a *Rayleigh* damping, which is a linear combination of the stiffness matrix and mass matrix, is employed and has the following form;

$$[\boldsymbol{C}] = A[\boldsymbol{K}] + B[\boldsymbol{M}], \tag{3.7}$$

where A and B are scalar coefficients.

3.2.2 Dynamic Equilibrium Equation

The dynamic equilibrium equation is obtained from the the principle of virtual work [12]:

$$\begin{aligned} &\int_{V_e} \{\delta \boldsymbol{u}\}^T \{\boldsymbol{F}\}\, dV \;\; + \int_{S_e} \{\delta \boldsymbol{u}\}^T \{\boldsymbol{\Phi}\}\, dS \;\; + \sum_{i=1}^{n} \{\delta \boldsymbol{u}\}_i^T \{\boldsymbol{p}\}_i \\ = &\int_{V_e} (\{\delta \boldsymbol{\epsilon}\}^T \{\boldsymbol{\sigma}\} \;\; + \{\delta \boldsymbol{u}\}^T \rho(\boldsymbol{x}) \{\ddot{\boldsymbol{u}}\} \;\; + \{\delta \boldsymbol{u}\}^T \kappa_d(\boldsymbol{x}) \{\dot{\boldsymbol{u}}\}) dV, \end{aligned} \tag{3.8}$$

where $\{\delta \boldsymbol{u}\}$ and $\{\delta \boldsymbol{\epsilon}\}$ are arbitrary virtual displacements and corresponding strains, respectively, $\{\boldsymbol{F}\}$ are body forces, $\{\boldsymbol{\Phi}\}$ are surface tractions, $\{\boldsymbol{p}\}$ are concentrated loads, $\kappa_d(\boldsymbol{x})$ is a parameter which is analogous to viscosity, $\rho(\boldsymbol{x})$ is mass density, and a each super-imposed dot indicates derivative with respect to time.

The vectors $\{\boldsymbol{u}\}$, $\{\dot{\boldsymbol{u}}\}$, and $\{\ddot{\boldsymbol{u}}\}$ are functions of time and space and can be interpolated as follows

$$\{\boldsymbol{u}\} = [\boldsymbol{N}] \{\boldsymbol{d}\}, \;\; \{\dot{\boldsymbol{u}}\} = [\boldsymbol{N}] \left\{\dot{\boldsymbol{d}}\right\}, \;\; \{\ddot{\boldsymbol{u}}\} = [\boldsymbol{N}] \left\{\ddot{\boldsymbol{d}}\right\}, \tag{3.9}$$

where the shape functions, $[\boldsymbol{N}]$, are functions of space, $\{\boldsymbol{d}\}$, $\left\{\dot{\boldsymbol{d}}\right\}$ and $\left\{\ddot{\boldsymbol{d}}\right\}$ denote the nodal displacements, velocities and accelerations, respectively. Substituting Eq. (3.9) into Eq. (3.8), one obtains

$$\begin{aligned} &[\int_{V_e} \rho(\boldsymbol{x}) [\boldsymbol{N}]^T [\boldsymbol{N}] dV \left\{\ddot{\boldsymbol{d}}\right\} + \int_{V_e} \kappa_d(\boldsymbol{x}) [\boldsymbol{N}]^T [\boldsymbol{N}] dV \left\{\dot{\boldsymbol{d}}\right\} + \int_{V_e} [\boldsymbol{B}]^T [\boldsymbol{D(x)}] [\boldsymbol{B}] dV \{\boldsymbol{d}\} \\ - &\int_{V_e} [\boldsymbol{N}]^T \{\boldsymbol{F}\}\, dV - \int_{S_e} [\boldsymbol{N}]^T \{\boldsymbol{\Phi}\}\, dS - \sum_{i=1}^{n} \{\boldsymbol{p}\}_i] \{\delta \boldsymbol{d}\}^T = 0, \end{aligned} \tag{3.10}$$

where $[\boldsymbol{B}]$ is the strain-displacement matrix, and $[\boldsymbol{D(x)}]$ is the constitutive matrix.

Since $\{\delta \boldsymbol{d}\}$ is arbitrary, the following finite element system of equations is obtained:

$$[\boldsymbol{M}] \left\{\ddot{\boldsymbol{d}}\right\} + [\boldsymbol{C}] \left\{\dot{\boldsymbol{d}}\right\} + [\boldsymbol{K}] \{\boldsymbol{d}\} = \left\{\boldsymbol{r}^{ext}\right\}, \tag{3.11}$$

where the mass, damping and stiffness matrices are respectively defined as

$$[\boldsymbol{M}] = \int_{V_e} \rho(\boldsymbol{x}) [\boldsymbol{N}]^T [\boldsymbol{N}] dV, \tag{3.12}$$

$$[\boldsymbol{C}] = \int_{V_e} \kappa_d(\boldsymbol{x}) [\boldsymbol{N}]^T [\boldsymbol{N}] dV, \tag{3.13}$$

$$[\boldsymbol{K}] = \int_{V_e} [\boldsymbol{B}]^T [\boldsymbol{D(x)}] [\boldsymbol{B}] dV, \tag{3.14}$$

and the external force vector is defined as

$$\left\{\boldsymbol{r}^{ext}\right\} = \int_{V_e} [\boldsymbol{N}]^T \{\boldsymbol{F}\}\, dV + \int_{S_e} [\boldsymbol{N}]^T \{\boldsymbol{\Phi}\}\, dS + \sum_{i=1}^{n} \{\boldsymbol{p}\}_i\,. \tag{3.15}$$

For the evaluation of the constitutive matrix, $[\boldsymbol{D}(\boldsymbol{x})]$, considering the material gradients, the GIF explained in Section 3.1 is employed.

3.2.3 Newmark β Method

Newmark [41] proposed a family of direct integration schemes, which has been widely used in dynamic analysis. The Newmark β method consists of the following expressions refer to the original paper by Newmark [41]:

$$[\boldsymbol{M}]\left\{\ddot{\boldsymbol{d}}\right\}_{n+1} + [\boldsymbol{C}]\left\{\dot{\boldsymbol{d}}\right\}_{n+1} + [\boldsymbol{K}]\{\boldsymbol{d}\}_{n+1} = \left\{\boldsymbol{r}^{ext}\right\}_{n+1}, \tag{3.16}$$

$$\{\boldsymbol{d}\}_{n+1} = \{\boldsymbol{d}\}_n + \Delta t\left\{\dot{\boldsymbol{d}}\right\}_n + \frac{\Delta t^2}{2}(1-2\beta)\left\{\ddot{\boldsymbol{d}}\right\}_n + \beta\Delta t^2\left\{\ddot{\boldsymbol{d}}\right\}_{n+1}, \tag{3.17}$$

$$\left\{\dot{\boldsymbol{d}}\right\}_{n+1} = \left\{\dot{\boldsymbol{d}}\right\}_n + (1-\gamma)\Delta t\left\{\ddot{\boldsymbol{d}}\right\}_n + \gamma\Delta t\left\{\ddot{\boldsymbol{d}}\right\}_{n+1}, \tag{3.18}$$

where subscripts n and $n+1$ indicate respective time steps, Δt is time increment, and β and γ are parameters depending on the integration schemes employed.

By defining the new quantities $\left\{\tilde{\boldsymbol{d}}\right\}_{n+1}$ and $\left\{\tilde{\dot{\boldsymbol{d}}}\right\}_{n+1}$ at the current time step [26],

$$\left\{\tilde{\boldsymbol{d}}\right\}_{n+1} = \{\boldsymbol{d}\}_n + \Delta t\left\{\dot{\boldsymbol{d}}\right\}_n + \frac{\Delta t^2}{2}(1-2\beta)\left\{\ddot{\boldsymbol{d}}\right\}_n, \tag{3.19}$$

$$\left\{\tilde{\dot{\boldsymbol{d}}}\right\}_{n+1} = \left\{\dot{\boldsymbol{d}}\right\}_n + (1-\gamma)\Delta t\left\{\ddot{\boldsymbol{d}}\right\}_n, \tag{3.20}$$

one rewrites Eqs. (3.17) and (3.18) as follows:

$$\{\boldsymbol{d}\}_{n+1} = \left\{\tilde{\boldsymbol{d}}\right\}_{n+1} + \beta\Delta t^2\left\{\ddot{\boldsymbol{d}}\right\}_{n+1}, \tag{3.21}$$

$$\left\{\dot{\boldsymbol{d}}\right\}_{n+1} = \left\{\tilde{\dot{\boldsymbol{d}}}\right\}_{n+1} + \gamma\Delta t\left\{\ddot{\boldsymbol{d}}\right\}_{n+1}. \tag{3.22}$$

Substituting Eqs. (3.19) through (3.22) into (3.16), one obtains an acceleration form of the Newmark method as follows:

$$\left([\boldsymbol{M}] + \gamma\Delta t[\boldsymbol{C}] + \beta\Delta t^2[\boldsymbol{K}]\right)\left\{\ddot{\boldsymbol{d}}\right\}_{n+1} = \left\{\boldsymbol{r}^{ext}\right\}_{n+1} + [\boldsymbol{C}]\left\{\tilde{\dot{\boldsymbol{d}}}\right\}_{n+1} - [\boldsymbol{K}]\left\{\tilde{\boldsymbol{d}}\right\}_{n+1}. \tag{3.23}$$

The vectors $\left\{\tilde{\boldsymbol{d}}\right\}_{n+1}$ and $\left\{\tilde{\dot{\boldsymbol{d}}}\right\}_{n+1}$ need to be evaluated to solve Eq. (3.23) for $\left\{\ddot{\boldsymbol{d}}\right\}_{n+1}$. Both quantities are obtained based on previous information $\left\{\ddot{\boldsymbol{d}}\right\}_{n}$, $\left\{\dot{\boldsymbol{d}}\right\}_{n}$, and $\{\boldsymbol{d}\}_n$ using Eqs. (3.19) and (3.20). Once $\left\{\ddot{\boldsymbol{d}}\right\}_{n+1}$ is determined through Eq.(3.23), a combination of $\left\{\ddot{\boldsymbol{d}}\right\}$, $\left\{\tilde{\boldsymbol{d}}\right\}$, and $\left\{\tilde{\dot{\boldsymbol{d}}}\right\}$ at time step (n+1) yields $\left\{\dot{\boldsymbol{d}}\right\}$ and $\left\{\dot{\boldsymbol{d}}\right\}$ at time step (n+1) using Eqs. (3.21) and (3.22). The next step follows the same procedure explained above, except that (n) is changed to (n+1) and (n+1) becomes (n+2).

The stability and accuracy of Newmark β methods depend on the parameters γ and β [12]. It is unconditionally stable when

$$2\beta \geq \gamma \geq \frac{1}{2}, \text{ (unconditionally stable),} \tag{3.24}$$

and conditionally stable for zero damping when

$$2\beta < \frac{1}{2}, \quad \gamma \geq \frac{1}{2}, \text{ and } \Delta t \leq \frac{(\gamma/2-\beta)^{1/2}}{\omega_{max}(\gamma/2-\beta)}, \text{ (conditionally stable),} \tag{3.25}$$

where ω_{max} is the maximum natural frequency of the structure.

When $\gamma = \frac{1}{2}$ and $\beta = \frac{1}{4}$, the method is called an *average acceleration method*, which is implicit and unconditionally stable with second order accuracy. When $\gamma = \frac{1}{2}$ and $\beta = 0$, it is called a *central difference method*. It is explicit and conditionally stable with second order accuracy.

3.2.4 Displacement Control Analysis

In some situations, a displacement control tends to be more stable than load control. So it is worth explaining in detail how it is implemented in this code. Unlike the general acceleration form, expressing Newmark β methods in a displacement form is useful to implement displacement control analysis. By solving Eq. (3.17) for $\left\{\ddot{\boldsymbol{d}}\right\}_{n+1}$ and substituting it into Eq. (3.18), one obtains the equations expressed as [13]

$$\left\{\ddot{\boldsymbol{d}}\right\}_{n+1} = \frac{1}{\beta\Delta t^2}(\{\boldsymbol{d}\}_{n+1} - \{\boldsymbol{d}\}_n - \Delta t\left\{\dot{\boldsymbol{d}}\right\}_n) - (\frac{1}{2\beta}-1)\left\{\ddot{\boldsymbol{d}}\right\}_n, \tag{3.26}$$

$$\left\{\dot{\boldsymbol{d}}\right\}_{n+1} = \frac{\gamma}{\beta\Delta t}(\{\boldsymbol{d}\}_{n+1} - \{\boldsymbol{d}\}_n) - (\frac{\gamma}{\beta}-1)\left\{\dot{\boldsymbol{d}}\right\}_n - \Delta t(\frac{\gamma}{2\beta}-1)\left\{\ddot{\boldsymbol{d}}\right\}_n. \tag{3.27}$$

Substituting these equations into Eq. (3.16) and solving for $\{\boldsymbol{d}\}_{n+1}$, one obtains

$$\begin{aligned}[\boldsymbol{K}^{eff}]\{\boldsymbol{d}\}_{n+1} &= \left\{\boldsymbol{r}^{ext}\right\}_{n+1} + [\boldsymbol{M}]\left\{\frac{1}{\beta\Delta t^2}\{\boldsymbol{d}\}_n + \frac{1}{\beta\Delta t}\left\{\dot{\boldsymbol{d}}\right\}_n + (\frac{1}{2\beta}-1)\left\{\ddot{\boldsymbol{d}}\right\}_n\right\} \\ &\quad +[\boldsymbol{C}]\left\{\frac{\gamma}{\beta\Delta t}\{\boldsymbol{d}\}_n + (\frac{\gamma}{\beta}-1)\left\{\dot{\boldsymbol{d}}\right\}_n + \Delta t(\frac{\gamma}{2\beta}-1)\left\{\ddot{\boldsymbol{d}}\right\}_n\right\}, \end{aligned} \tag{3.28}$$

where

$$[\boldsymbol{K}^{eff}] = \frac{1}{\beta\Delta t^2}[\boldsymbol{M}] + \frac{\gamma}{\beta\Delta t}[\boldsymbol{C}] + [\boldsymbol{K}]. \tag{3.29}$$

In Eq.(3.29), $\left\{\boldsymbol{r}^{ext}\right\}_{n+1}$ is zero because in the displacement control analysis, there is no external force. The only variable determining the structural behavior is the displacement at the nodes where displacement boundary condition is prescribed.

Let's let

$$\begin{aligned}\left\{\boldsymbol{p}^{eff}\right\}_n &= [\boldsymbol{M}]\left\{\frac{1}{\beta\Delta t^2}\{\boldsymbol{d}\}_n + \frac{1}{\beta\Delta t}\left\{\dot{\boldsymbol{d}}\right\}_n + (\frac{1}{2\beta}-1)\left\{\ddot{\boldsymbol{d}}\right\}_n\right\} \\ &\quad +[\boldsymbol{C}]\left\{\frac{\gamma}{\beta\Delta t}\{\boldsymbol{d}\}_n + (\frac{\gamma}{\beta}-1)\left\{\dot{\boldsymbol{d}}\right\}_n + \Delta t(\frac{\gamma}{2\beta}-1)\left\{\ddot{\boldsymbol{d}}\right\}_n\right\}. \end{aligned} \tag{3.30}$$

Based on the Eqs. (3.29) and (3.30), $[\boldsymbol{K}^{eff}]$ and $\left\{\boldsymbol{p}^{eff}\right\}$ can be divided as follows [37]:

$$\begin{bmatrix} [\boldsymbol{K}^{eff}_{ff}] & [\boldsymbol{K}^{eff}_{fs}] \\ [\boldsymbol{K}^{eff}_{sf}] & [\boldsymbol{K}^{eff}_{ss}] \end{bmatrix} \left\{ \begin{matrix} \{\boldsymbol{d}_f\}_{n+1} \\ \{\boldsymbol{d}_s\}_{n+1} \end{matrix} \right\} = \left\{ \begin{matrix} \left\{\boldsymbol{p}^{eff}_f\right\}_n \\ \left\{\boldsymbol{p}^{eff}_s\right\}_n \end{matrix} \right\} \tag{3.31}$$

where subscript f, s , (n) and $(n+1)$ denote free boundary, support boundary, $(n)^{th}$ time step and $(n+1)^{th}$ time step, respectively. In the above matrix form, $\{\boldsymbol{d}_s\}$ and $\left\{\boldsymbol{p}^{eff}_f\right\}$ are known. Therefore the general solution is obtained by

$$\left\{\{\boldsymbol{d}_f\}_{n+1}\right\} = [\boldsymbol{K}^{eff}_{ff}]^{-1}\left\{\left\{\boldsymbol{p}^{eff}_f\right\}_n - [\boldsymbol{K}^{eff}_{fs}]\{\boldsymbol{d}_s\}_{n+1}\right\}. \tag{3.32}$$

3.3 Numerical Implementation

The M-integral used to obtain SIFs consists of actual and auxiliary fields, which are based on the global coordinate system and local systems, respectively. Thus, transformation is unavoidable to obtain SIFs. In this section, numerical aspects on evaluating M-integral are provided. They include the relation between global M-integral quantities and local M-integral quantities, and the transformation of auxiliary fields from local to global coordinate systems.

3.3.1 M-Integral: Numerical Aspects

The actual fields such as displacements, strains and stresses are evaluated globally by means of the FEM, while the auxiliary fields and SIFs are local quantities. In this work, the M-integral given by Eq. (2.37) is first computed globally to utilize the actual fields without any transformation and then transformed into the local system to obtain the SIFs.

The global M-integral quantities are evaluated as ($m = 1, 2$):

$$\begin{aligned}(M_m)^g &= \int_A \left\{ (\sigma_{ij}^{aux} u_{i,m} + \sigma_{ij} u_{i,m}^{aux}) - \sigma_{ik}^{aux} \varepsilon_{ik} \delta_{mj} \right\} \frac{\partial q}{\partial X_j} dA \\ &+ \int_A \left\{ \sigma_{ij,j}^{aux} u_{i,m} + \rho \ddot{u}_i u_{i,m}^{aux} - C_{ijkl,m} \varepsilon_{kl}^{aux} \varepsilon_{ij} \right\} q dA, \end{aligned} \tag{3.33}$$

where superscript "g" means global coordinate and X denotes the global coordinate system. The local M-integral quantities are evaluated as

$$M_{local} = (M_1)^g \cos\theta + (M_2)^g \sin\theta. \tag{3.34}$$

3.3.2 Computation of M-Integral Terms

Since the computation of the M-integral is first evaluated in the global coordinate system, each term of auxiliary fields should be evaluated globally, too. In other words, since the auxiliary fields are local quantities, they are computed locally and then transformed into global coordinates to be used in the M-integral. Derivation and explanation of auxiliary field evaluation is based on the non-equilibrium formulation, which is the method implemented in the code (see discussion of alternative methods in Section 1.3.2).

The displacement field of Williams' [58] solution can be written in compact form as (cf. Eqs. (1.24) and (1.25))

$$u^l(r,\theta)_i^{aux} = \frac{K_I^{aux}}{\mu_{tip}} f_i^I(r,\theta) + \frac{K_{II}^{aux}}{\mu_{tip}} f_i^{II}(r,\theta), \ (i = 1, 2), \tag{3.35}$$

where K_I^{aux} and K_{II}^{aux} are mode I and mode II SIFs of the auxiliary fields, respectively, and the angular functions $f_i^I(r,\theta)$ and $f_i^{II}(r,\theta)$ are given by Eqs. (1.24) and (1.25).

The derivatives of auxiliary displacements with respect to the global coordinate systems are calculated as follows ($k = 1, 2$) :

$$u^g(r,\theta)_{i,k}^{aux} = \frac{\partial u^g(r,\theta)_i^{aux}}{\partial X_k} = \frac{\partial u^g(r,\theta)_i^{aux}}{\partial r} \frac{\partial r}{\partial X_k} + \frac{\partial u^g(r,\theta)_i^{aux}}{\partial \theta} \frac{\partial \theta}{\partial X_k}, \tag{3.36}$$

where

$$\begin{Bmatrix} u^g(r,\theta)_1^{aux} \\ u^g(r,\theta)_2^{aux} \end{Bmatrix} = \begin{bmatrix} \cos\alpha & -\sin\alpha \\ \sin\alpha & \cos\alpha \end{bmatrix} \begin{Bmatrix} u^l(r,\theta)_1^{aux} \\ u^l(r,\theta)_2^{aux} \end{Bmatrix}, \tag{3.37}$$

and

$$\frac{\partial r}{\partial X_k} = \frac{\partial r}{\partial x_1}\frac{\partial x_1}{\partial X_k} + \frac{\partial r}{\partial x_2}\frac{\partial x_2}{\partial X_k}, \quad \frac{\partial \theta}{\partial X_k} = \frac{\partial \theta}{\partial x_1}\frac{\partial x_1}{\partial X_k} + \frac{\partial \theta}{\partial x_2}\frac{\partial x_2}{\partial X_k}, \tag{3.38}$$

with

$$\begin{aligned} \frac{\partial r}{\partial x_1} = \cos\theta,\ \frac{\partial r}{\partial x_2} &= \sin\theta \\ \frac{\partial \theta}{\partial x_1} = -\frac{\sin\theta}{r},\ \frac{\partial \theta}{\partial x_2} &= \frac{\cos\theta}{r} \\ \frac{\partial x_1}{\partial X_1} = \cos\alpha\ ,\ \frac{\partial x_1}{\partial X_2} &= \sin\alpha \\ \frac{\partial x_2}{\partial X_1} = -\sin\alpha\ ,\ \frac{\partial x_2}{\partial X_2} &= \cos\alpha. \end{aligned} \tag{3.39}$$

As illustrated in Figure 3.3, α is the angle between global and local coordinates, r is the radial distance, and θ is the angle between local and the point where field quantities are obtained.

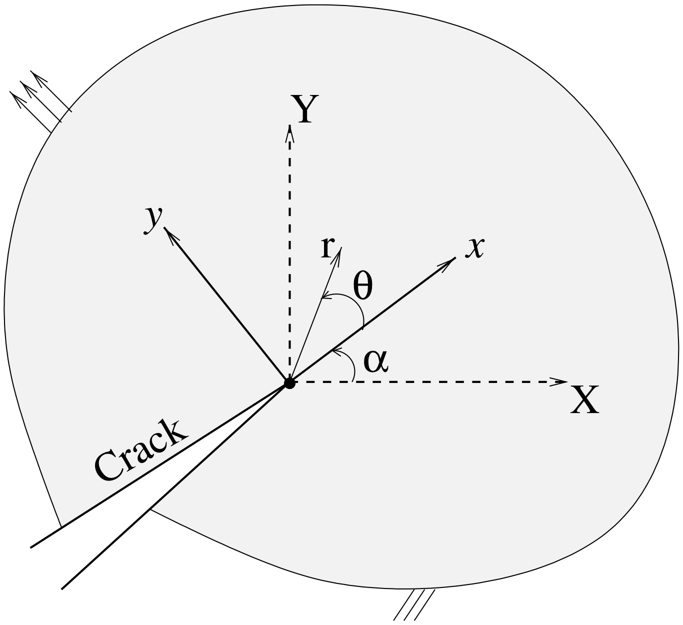

Figure 3.3: Local (x, y) and global (X,Y) coordinate systems.

Due to the non-equilibrium formulation, the auxiliary strain field is obtained using the compatibility condition as:

$$\varepsilon^g(r,\theta)_{ij}^{aux} = \frac{1}{2}(u^g(r,\theta)_{i,j}^{aux} + u^g(r,\theta)_{j,i}^{aux}), \tag{3.40}$$

where $u^g(r,\theta)_{i,j}$ is obtained using Eq. (3.36).

The auxiliary stress is evaluated using the constitutive relationship (cf. Eq. (1.28)):

$$\sigma^g(r,\theta)_{ij}^{aux} = C_{ijkl}(\boldsymbol{x})\varepsilon^g(r,\theta)_{kl}^{aux}. \tag{3.41}$$

The material properties used in the constitutive tensor are computed using the isoparametric formulation, which is explained in Section 3.1.

The derivative of the auxiliary stress is given by

$$\begin{aligned}(\sigma^g(r,\theta)_{ij}^{aux})_{,j} &= (C_{ijkl}(\boldsymbol{x})\varepsilon^g(r,\theta)_{kl}^{aux})_{,j} \\ &= C_{ijkl,j}\varepsilon^g(r,\theta)_{kl}^{aux} + C_{ijkl}\varepsilon^g(r,\theta)_{kl,j}^{aux},\end{aligned} \tag{3.42}$$

where the derivative of auxiliary fields with respect to global coordinates, $\varepsilon^g(r,\theta)_{kl,j}^{aux}$, is evaluated as follows:

$$\varepsilon^g(r,\theta)_{ij,k}^{aux} = \frac{\partial\varepsilon^g(r,\theta)_{ij}^{aux}}{\partial X_k} = \frac{\partial\varepsilon^g(r,\theta)_{ij}^{aux}}{\partial r}\frac{\partial r}{\partial X_k} + \frac{\partial\varepsilon^g(r,\theta)_{ij}^{aux}}{\partial\theta}\frac{\partial\theta}{\partial X_k}. \tag{3.43}$$

In computing Eq. (3.43), the expressions (3.38) and (3.39) are used.

Chapter 4

Verification

Since a new finite element code has been developed, verification of the code is crucial before we discuss the influence of material profiles on the variation of DSIFs for a nonhomogeneous cracked body in Chapter 5. Thus, five different examples are examined to verify the numerical implementations such as the Newmark β method and the M-integral, which are used to obtain dynamic field quantities and SIFs, respectively. The first problem is a nonhomogeneous infinite plate with material gradation perpendicular to external loadings. The σ_{yy} stress is compared with analytical solutions. The second problem is a homogeneous cantilever beam where sinusoidal external loading is applied. The tip displacement is verified through comparison with analytical solutions. This problem is also extended to consider nonhomogeneous materials. The third problem is a nonhomogeneous unbounded plate with an arbitrarily oriented crack where SIFs are verified. The fourth problem is a homogeneous edge cracked semi-infinite plate under impact velocity. The history of mixed mode DSIFs is obtained analytically and compared with present numerical solutions. The last problem is a nonhomogeneous edge cracked semi-infinite plate subjected to dynamic loading where Young's modulus varies exponentially along the x direction. An UMAT of Abaqus and DCT are adopted to verify DSIFs for dynamic nonhomogeneous case.

4.1 Verification Problems without Cracks

In this section, two uncracked bodies are employed and examined to verify static and dynamic finite element implementations. For the static case, analytical solutions of σ_{yy} for isotropic nonhomogeneous materials, where material properties vary exponentially along the x direction, are used as reference solutions to verify the numerical implementation [20]. For the dynamic case, the numerical tip displacement of a homogeneous cantilever beam subjected to a transient sinusoidal dynamic loading is compared with analytical solutions [55].

4.1.1 Static Response of a Nonhomogeneous Infinite Plate

Erdogan and Wu [20] investigated an infinite nonhomogeneous medium where material gradations are perpendicular to external loading, which may be of the following type: a fixed grip, membrane loading and bending.

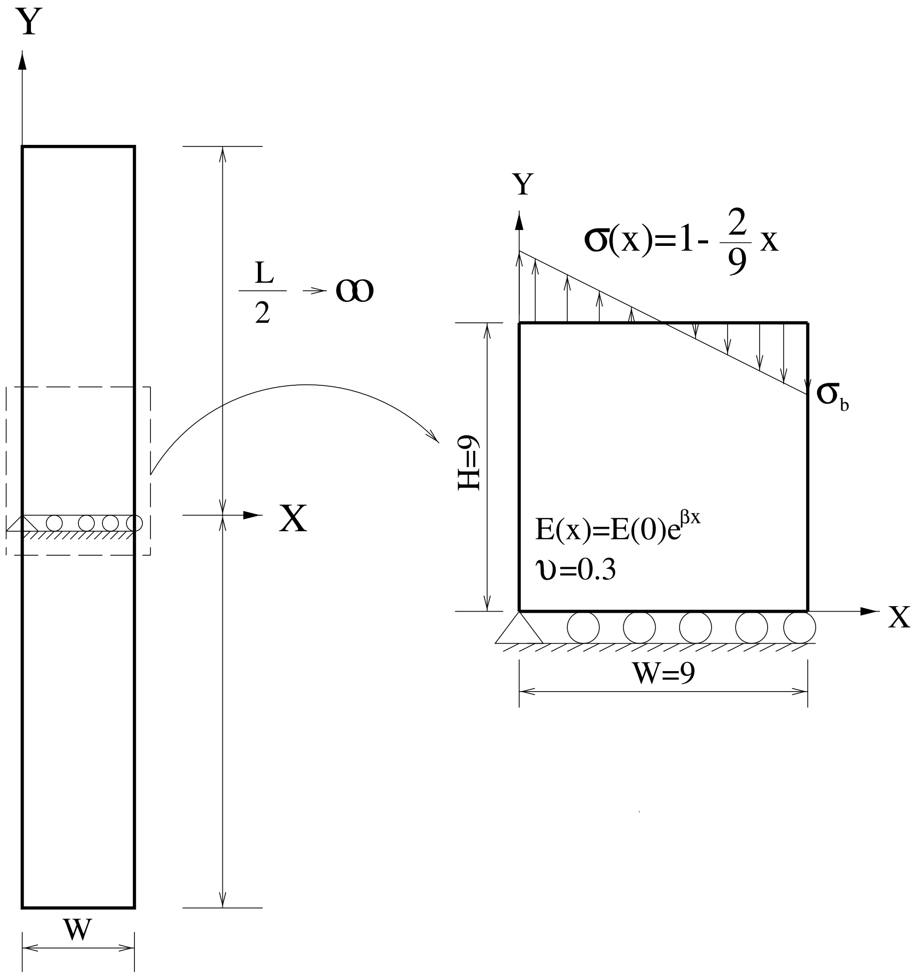

Figure 4.1: Geometry and boundary conditions for a nonhomogeneous plate.

A rectangular finite plate with the width W=9 and the height H=9 is chosen as illustrated in Figure 4.1. The external forces which vary with a function, $\sigma(x) = 1 - 2x/9$, are applied to the top edge given by

$$M = \frac{\sigma_b W^2}{6}, \tag{4.1}$$

where σ_b is the magnitude of external traction applied at the top right or left node (see Figure 4.1). Displacement boundary conditions, $u_2 = 0$ for the bottom edge and $u_1 = 0$ for the left bottom node, are prescribed. Constant Poisson's ratio ν=0.3 is used. The elastic modulus varies exponentially along the x direction, that is,

$$E(x) = E(0)e^{\beta x}, \quad \beta = \frac{1}{W} log \left(\frac{E(W)}{E(0)} \right), \tag{4.2}$$

where $E(0)$=1, $E(W)$=8 and β is a material nonhomogeneity parameter. Plane stress, eight-node quadrilateral (Q8) and six-node triangular (T6) elements are used with a reduced integration scheme.

The compatibility condition, $\partial \varepsilon_{yy}^2 / \partial x^2 = 0$, yields strain and stress fields given by [20]

$$\varepsilon_{yy} = Ax + B, \tag{4.3}$$

$$\sigma_{yy}(x) = E(0)e^{\beta x}(Ax + B), \tag{4.4}$$

where the coefficients A and B are determined from the following equilibrium equations for bending,

$$\int_0^W \sigma_{yy}(x)\ dx = 0\ , \int_0^W \sigma_{yy}(x) x\ dx = M, \tag{4.5}$$

where the moment M is given by Eq. (4.1). So, the stress distribution is

$$\begin{aligned} \sigma_{yy}(x) &= \beta^2 M e^{\beta x} \left\{ \left(\frac{\beta \left(1 - e^{\beta W}\right)}{e^{\beta W} \beta^2 W^2 - e^{2\beta W} + 2e^{\beta W} - 1} \right) x \right. \\ &+ \left. \frac{\beta W e^{\beta W} - e^{\beta W} + 1}{e^{\beta W} \beta^2 W^2 - e^{2\beta W} + 2e^{\beta W} - 1} \right\}. \end{aligned} \tag{4.6}$$

Figure 4.2 shows a comparison between the analytical solutions and the numerical results. The abscissa indicates the horizontal distance where y is zero. The ordinate indicates σ_{yy}. The numerical results agree well with the analytical solutions. The discrepancy between numerical and analytical results might be due to the fact that the analytical solution is derived based on an infinite length, while numerical results are determined based on a finite length. The difference between numerical results using Q8 and T6 elements is negligible.

4.1.2 Dynamic Response of Homogeneous and Nonhomogeneous Cantilever Beams

A homogeneous cantilever beam is used to verify dynamic field quantities by means of comparison of present numerical results with analytical solution, and a nonhomogeneous cantilever beam is employed to examine the influence of material gradation on the dynamic behavior.

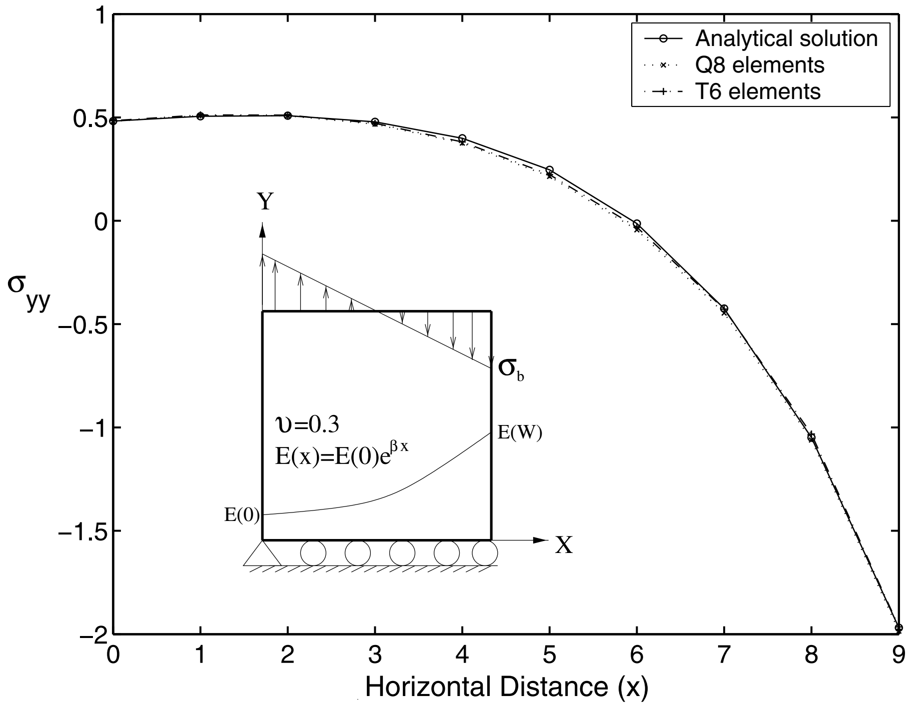

Figure 4.2: Comparison of FEM results for stress distribution (σ_{yy}) with analytical solutions [20] for bending loads.

Warburton [55] investigated transient dynamic response of a cantilever beam subjected to a sinusoidal dynamic loading assuming no damping. Figure 4.3 illustrates the boundary conditions and geometry of a cantilever beam with length L=20mm and height H=0.1mm. The loading, applied to the free end of the beam, consists of a sinusoidal function whose duration T corresponds to the fundamental period of a vibration mode given by [55]

$$T = \frac{2\pi}{\omega_1}, \quad \omega_i^2 = \lambda_i^4 \frac{EI}{\rho A} \ \ (i = 1, 2, 3, ...), \tag{4.7}$$

where ω_i is the fundamental frequency and A, E, ρ, and I denote the cross-sectional area, Young's modulus, mass density and moment of inertia, respectively. Besides, λ_i is given by

$$\lambda_1 L = 1.875, \quad \lambda_2 L = 4.694, \quad \lambda_3 L = 7.855. \tag{4.8}$$

The tip deflection w(L,t) is [55]

$$\mathrm{w}(L, t) = 4\frac{P}{m}\sum_i [\frac{1}{\omega_i}\int_0^t \sin\frac{\pi\tau}{T}\sin\omega_i(t-\tau)d\tau] \quad \text{for} \quad 0 \le t \le T$$

$$= 4\frac{PL^3}{EI}\sum_i [\frac{\pi/(\omega_i T)}{(\lambda_i L)^4((\pi/(\omega_i T))^2-1)}\{(\cos\omega_i T+1)+\sin\omega_i(t-T)+\sin\omega_i T\cos\omega_i(t-T)\}]. \quad \text{for} \quad T \le t \qquad (4.9)$$

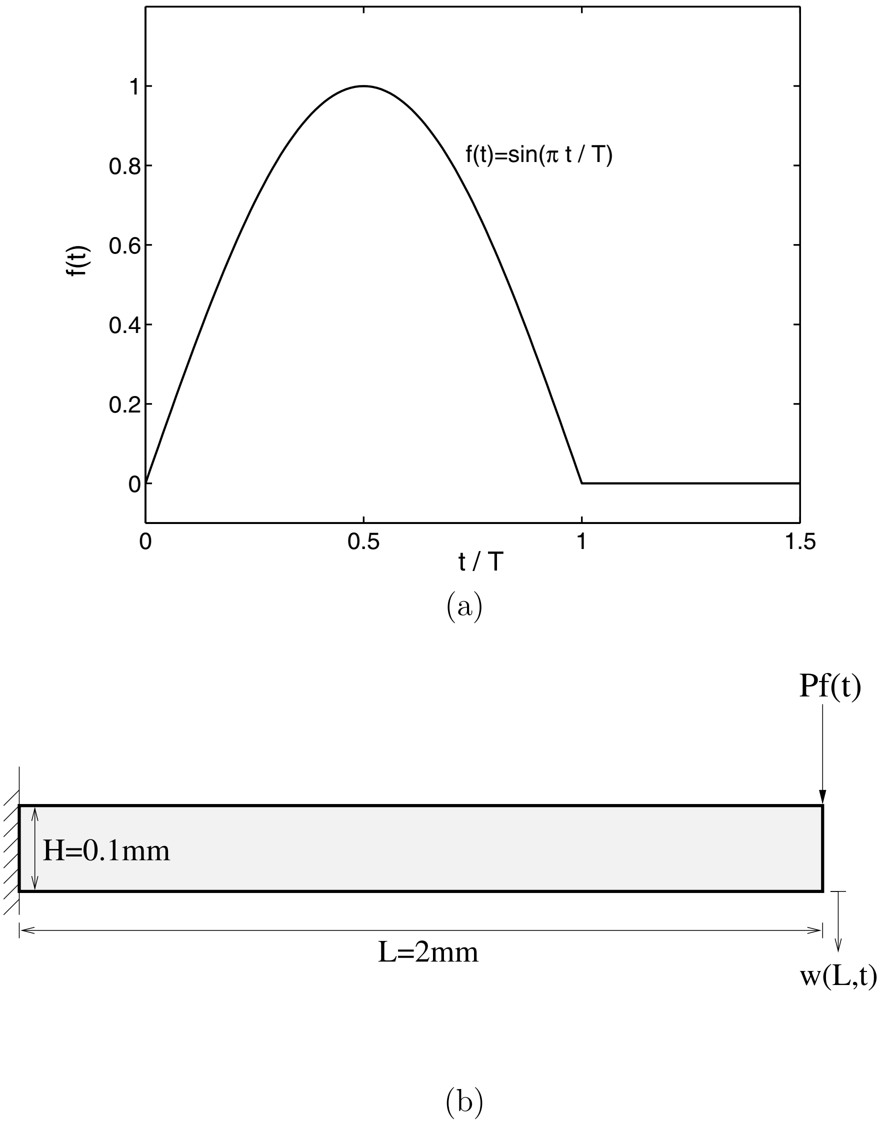

Figure 4.3: A cantilever beam subjected to half-sine pulse loading: (a) half-sine pulse loading; (b) cantilever beam with height 0.1mm and length 2mm. The vertical tip displacement is denoted by w(L,t).

For the nonhomogeneous beam, the Young's modulus vary linearly as given by

$$E = E_1 + (E_2 - E_1)x/L, \qquad (4.10)$$

where subscripts 1 and 2 indicates the location of clamped end and free end, respectively. Table 4.1 shows material properties for both homogeneous and nonhomogeneous beams. Constant Poisson's ratio of 0.3 and constant mass density of 7850 Kg/m^3 are used for all the analyses. The input loading (Fig. 4.3 (a)) is the same for all the beams (see Table 4.1). Damping is neglected and a consistent mass matrix method is used. Plane stress condition is adopted and the *average acceleration method* is employed.

Table 4.1: Material properties for both homogeneous and nonhomogeneous beams.

Beam	$E_1(GPa)$	$E_2(GPa)$
Homogeneous	210	210
Nonhomogeneous (clamped end is stiff)	336	84
Nonhomogeneous (clamped end is soft)	84	336

Figure 4.4 illustrates the comparison of the present numerical results for the homogeneous beam with the analytical solution by Warburton [55]. Numerical results are also given for the nonhomogeneous beams. The abscissa indicates time normalized with respect to T, the first fundamental period for the homogeneous beam, and the ordinate indicates the tip displacement normalized as $PL^3/E_{avg}I$. Notice that E_{avg} is same for homogeneous and nonhomogeneous beams. The same T, obtained from expression (4.7) for the homogeneous beam, is adopted for all the cases (homogeneous and nonhomogeneous beams). For the homogeneous case, the present numerical results match remarkably well with the analytical solution as illustrated in Figure 4.4. For nonhomogeneous case, a beam softer at the clamped end ($E_1/E_2 = 1/4$) is more compliant than a beam stiffer at the clamped end ($E_1/E_2 = 4$) such that it produces larger period and higher magnitude compared to the latter.

4.2 Verification Problems with Cracks

In this section, three cracked bodies of either homogeneous or nonhomogeneous materials are analyzed to verify the M-integral implementation. The first problem is an unbounded nonhomogeneous elastic medium containing an arbitrarily oriented crack. Analytical mixed-mode SIFs from the literature are compared with present numerical results to verify the M-integral implementation for the static nonhomogeneous case. The second problem is a homogeneous edge-cracked semi-infinite plate under dynamic loading. Calculated DSIFs are used as reference solution to verify the M-integral implementation for dynamic loading of homogeneous cracked specimen. The last problem is a nonhomogeneous edge-cracked semi-infinite plate under dynamic loading. In order to verify the M-integral implementation for

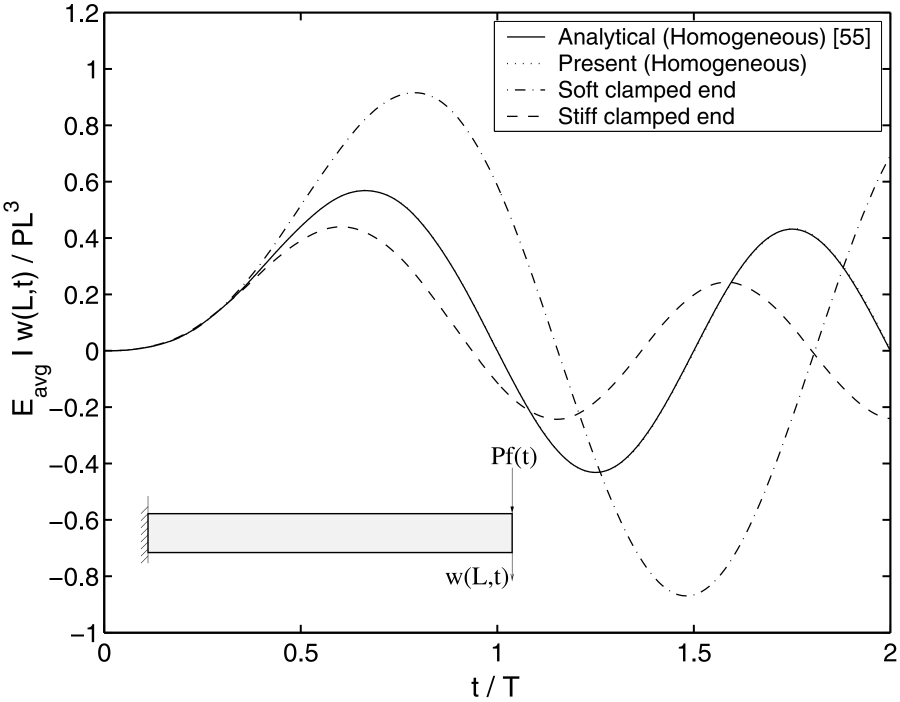

Figure 4.4: Normalized tip deflection versus normalized time. The time is normalized with respect to T, which denotes the first fundamental period for the homogeneous beam.

the dynamic nonhomogeneous case, the UMAT of ABAQUS and the DCT are employed.

4.2.1 Nonhomogeneous Unbounded Plate with an Arbitrarily Oriented Crack

Konda and Erdogan [33] obtained mixed-mode SIFs for an unbounded nonhomogeneous elastic medium containing an arbitrarily oriented crack by solving integral equations. A finite plate, which is large relative to a crack length 2a = 8, is chosen with width $2W$=80 and height $2H$=80, as illustrated in Figure 4.5 (a). Figures 4.5 (b), (c) and (d) show the whole mesh configuration, crack tip region and three different contours, respectively.

Young's modulus varies exponentially along the x direction with a function, $E(x) = \bar{E}e^{\beta x}$, and a constant Poisson's ratio of 0.3 is used. Due to the material gradient for the fixed-grip loading, the applied load is equal to $\sigma_{22}(x, 40) = \bar{\varepsilon}\bar{E}e^{\beta X}$ where $\bar{\varepsilon}$ and $\bar{E}$ are equal to 1. Displacement boundary conditions, $u_2 = 0$ for the bottom edge and $u_1 = 0$ for the left bottom node, are prescribed. Plane stress elements are used for the bulk elements which consist of 446 Q8 and 274 T6 elements. Ratios $\beta a = 0.5$ and $\theta/\pi = 0.32$ are chosen.

Table 4.2 shows normalized K_I and K_{II} for three different contours, demonstrating path

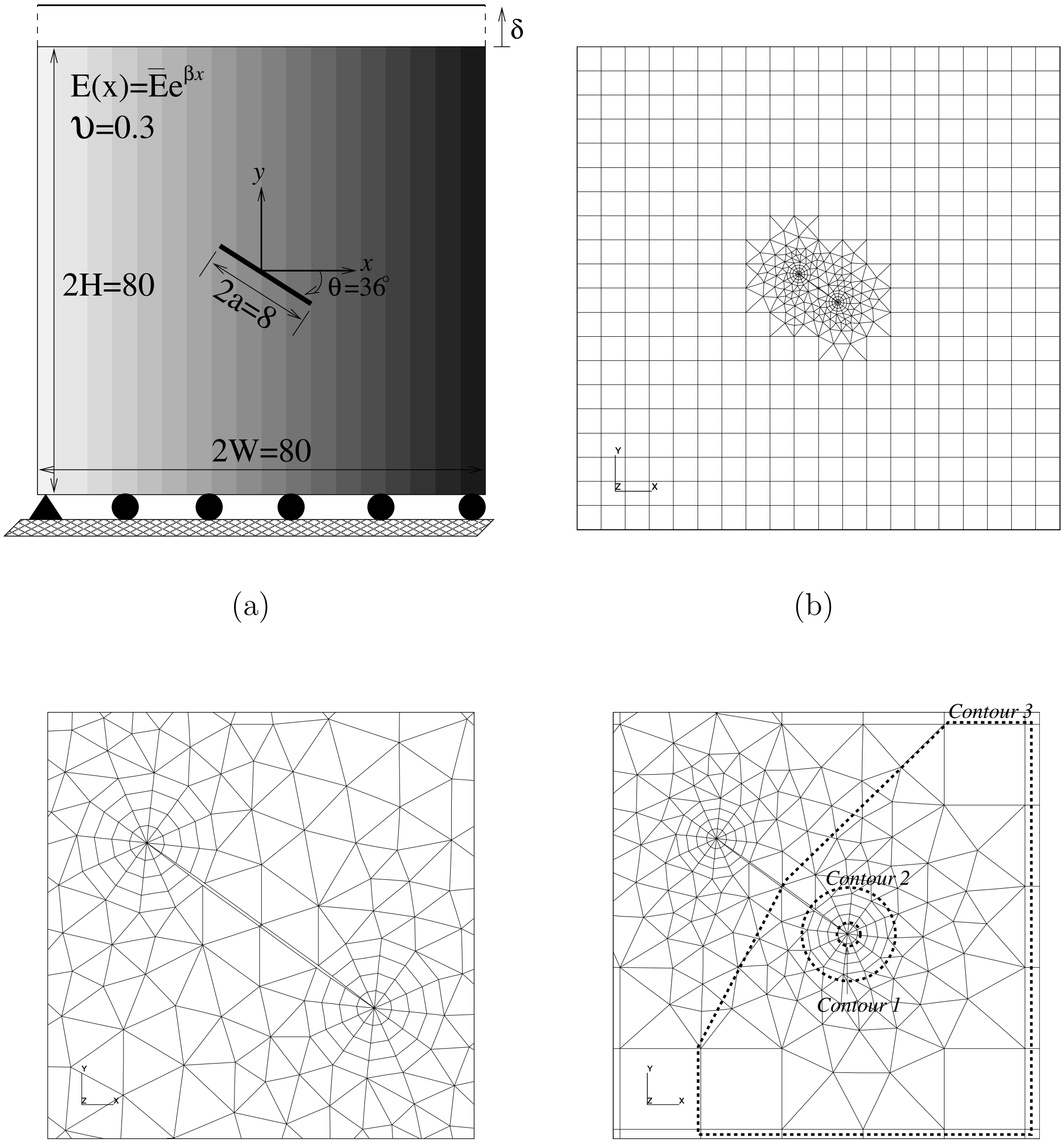

(a) (b)

(c) (d)

Figure 4.5: Nonhomogeneous unbounded plate: (a) geometry, boundary conditions and material properties; (b) mesh configuration for the whole geometry; (c) mesh details for the crack tip (12 sectors and 4 rings); (d) 3 different contours.

independence of the M-integral. The mixed mode SIFs are normalized with respect to $K_0 = \bar{\varepsilon}\bar{E}\sqrt{\pi \mathrm{a}}$. Table 4.3 compares the present normalized SIFs with the analytical solutions obtained by Konda and Erdogan [33], and numerical results obtained by Dolbow and Gosz [15] using X-FEM and by Kim and Paulino [31] using the I-FRANC2D finite element code. Dolbow and Gosz [15], and Kim and Paulino [31] used the M-integral to obtain SIFs.

Table 4.2: Normalized SIFs at the right crack tip for 3 different contours ($\beta a = 0.5$ and $\theta/\pi = 0.32$).

	Contour 1	Contour 2	Contour 3
K_I	0.9270	0.9225	0.9224
K_{II}	-0.5446	-0.5492	-0.5502

Good agreement exists between the present numerical results and the analytical solutions, which have a maximum difference of 0.8 percent.

Table 4.3: Comparison of normalized SIFs at both crack tips between the present solution, and the current analytical solution and numerical results ($\beta a = 0.5$ and $\theta/\pi = 0.32$).

	Left crack tip		Right crack tip	
References	K_I	K_{II}	K_I	K_{II}
Konda and Erdogan [33]	0.925	-0.548	0.460	-0.365
Present	0.9225	-0.5492	0.4560	-0.3623
Kim and Paulino [31]	0.9224	-0.5510	0.4559	-0.3621
Dolbow and Gosz [15]	0.930	-0.560	0.467	-0.364

4.2.2 Homogeneous Edge Cracked Semi-Infinite Plate

Lee and Freund [35] evaluated mixed-mode DSIFs for an edge-cracked semi-infinite plate under impact loading using linear superposition of obtainable stress wave solutions. During the period from initial loading until the first scattered waves at the crack tip are reflected, the mixed-mode SIF history was determined. Belytschko et al. [4] studied this problem numerically and evaluated DSIFs using the EFG method.

A finite plate with width W=0.2m, height H=0.3m and crack length a=0.05m is chosen, as illustrated in Figure 4.6. The velocity, v=6.5m/s, is imposed on the upper half of the left boundary and no other boundary conditions are prescribed (see Figure 4.6 (a)). The material properties of steel are chosen as E=200GPa, $\rho = 7850Kg/m^3$ and ν=0.25. The corresponding wave speeds are

$$C_d = \sqrt{\frac{E(1-\nu)}{\rho(1+\nu)(1-2\nu)}} = 5529.3\ m/sec, \tag{4.11}$$

$$C_s = \sqrt{\frac{E}{2\rho(1+\nu)}} = 3192\ m/sec, \tag{4.12}$$

$$C_R \approx 0.928c_s \approx 2962\ m/sec, \tag{4.13}$$

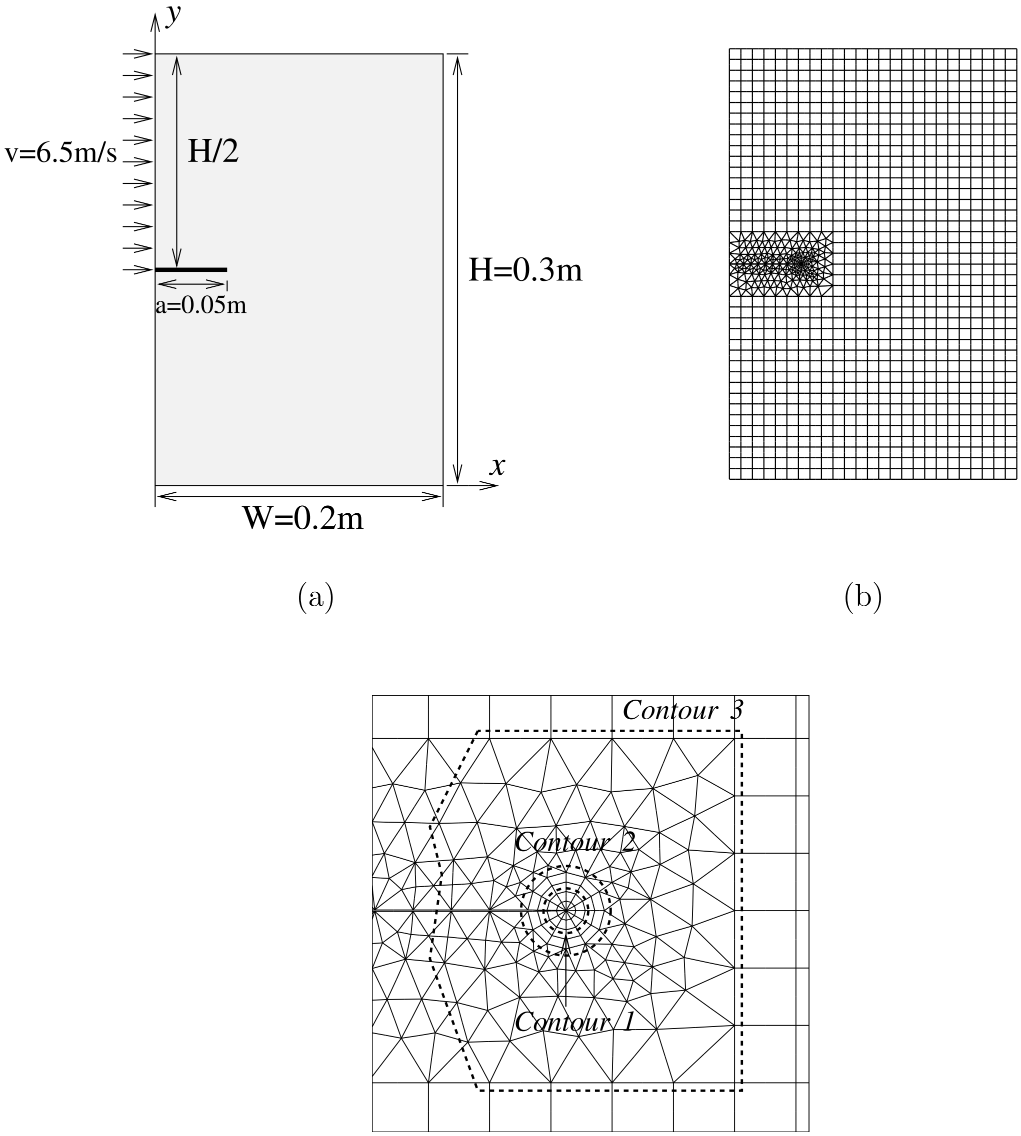

(a) (b)

(c)

Figure 4.6: Edge cracked semi-infinite plate: (a) geometry and boundary conditions; (b) mesh configuration for the whole geometry; (c) close up of crack tip (12 sectors and 4 rings) and 3 different contours.

where C_d, C_s and C_R are the longitudinal wave, shear wave, and *Rayleigh* wave speeds [24], respectively. Plane strain condition is used with a full integration scheme, and the *average acceleration method* is used with a time step of $\Delta t = 0.4\ \mu s$. Consistent mass matrix is used for the mass matrix formulation.

Due to the instantaneous velocity, first compressive waves are propagated and then relatively large shear waves are induced around the crack tip. Normalized mixed-mode DSIFs versus normalized time are plotted for three different contours in Figure 4.7. The abscissa is time normalized with respect to the crack length and dilatational wave speed, and the ordinate is DSIFs normalized as

$$\frac{E\mathrm{v}\sqrt{\frac{a}{\pi}}}{2C_d(1-\nu^2)}. \tag{4.14}$$

The history of DSIFs is plotted from the initial loading until the first wave scattered at the crack tip bounces back from the boundary. Since the numerical results overlap each other, path independence is demonstrated numerically.

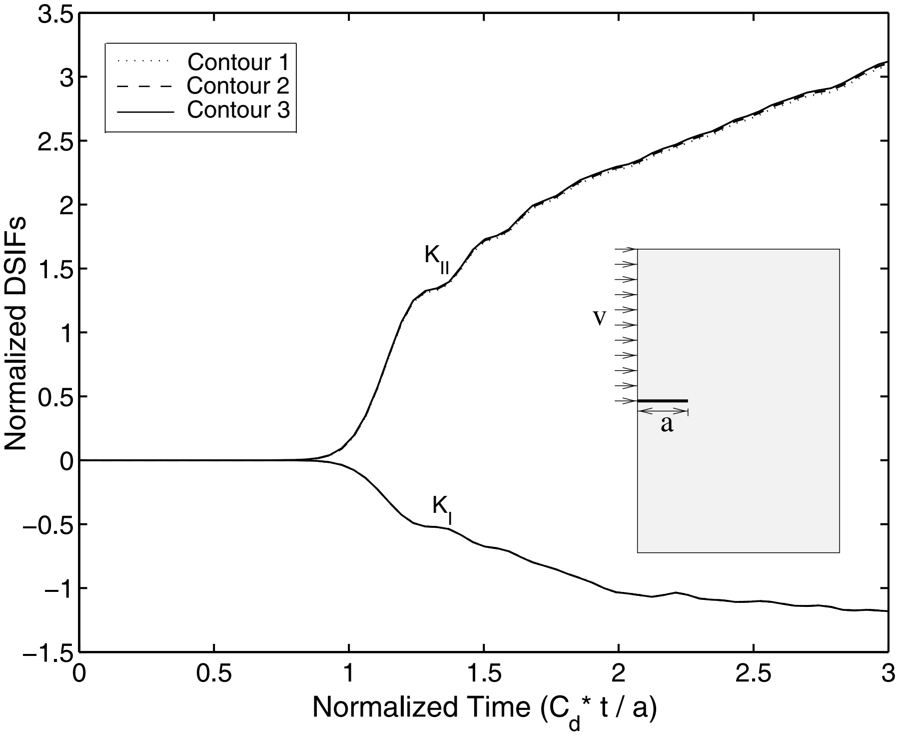

Figure 4.7: Normalized DSIFs for three different contours.

The present numerical results are compared with the analytical solutions [35] in Fig. 4.8. For both K_I and K_{II}, the present numerical results and analytical solutions agree well. The magnitude of DSIFs increases gradually, due to the instantaneous velocity. Besides, the compressive waves and relatively large shear waves generated from the velocity induce the negative K_I and positive K_{II}, respectively, as shown in Fig. 4.8.

4.2.3 Nonhomogeneous Edge Cracked Semi-Infinite Plate

In the previous example, the M-integral implementation for dynamic homogeneous case was verified by comparing the present numerical results with the analytical solutions by Lee and

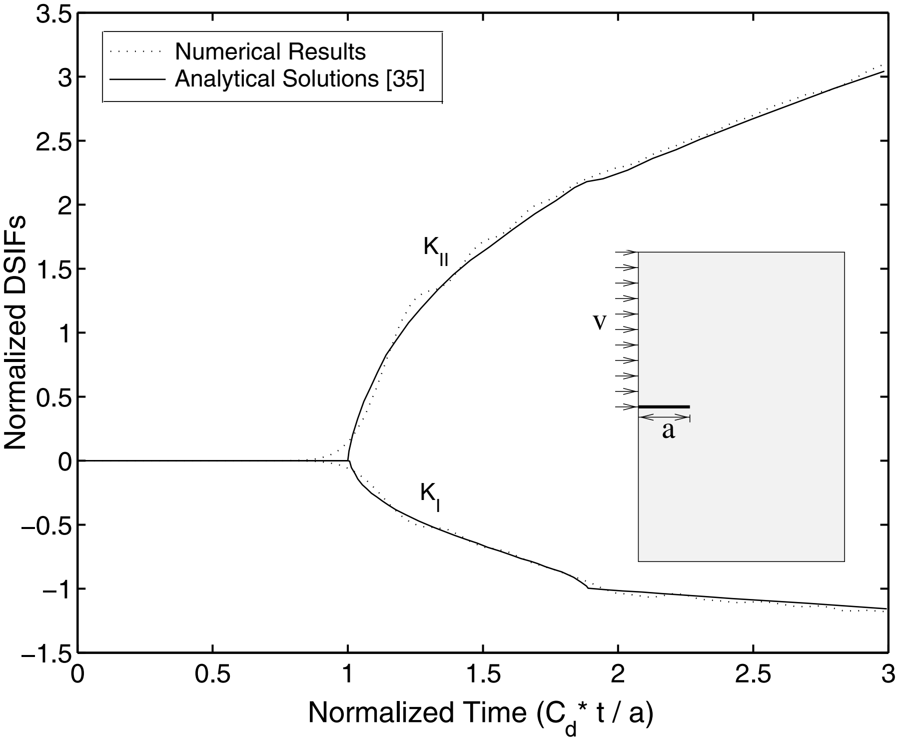

Figure 4.8: Comparison of the numerical results with the analytical solutions.

Freund [35]. In this section, UMAT of ABAQUS [1] is used to incorporate material gradations of Young's modulus and Poisson's ratio under dynamic loading, and the DCT [49] is employed to verify the M-integral implementation for the dynamic nonhomogeneous case. The UMAT is developed to analyze pavement systems which are graded due to temperature gradients and aging related stiffness gradients [7]. In the UMAT, graded elements are implemented by means of direct sampling of properties at the Gauss points of the element [28].

The same geometry and boundary conditions shown in Figure 4.6 (a) are used. The mass density and Poisson's ratio are $\rho = 7850 Kg/m^3$ and ν=0.25, respectively. The elastic modulus varies exponentially along the x direction as follows:

$$E(x) = E(0)e^{\beta x}, \quad \beta = \frac{1}{W} log\left(\frac{E(W)}{E(0)}\right), \tag{4.15}$$

where W=0.2m, $E(0)$=100GPa, $E(W)$=300GPa and β is the material nonhomogeneity parameter. The material properties at the crack tip are $E = 131.6 GPa$, $\rho = 7850 Kg/m^3$ and $\nu = 0.25$. Plane strain elements are used with both reduced and full integration schemes. The *average acceleration method* is adopted with a time step of $\Delta t = 0.4\ \mu s$ and consistent mass matrix is employed.

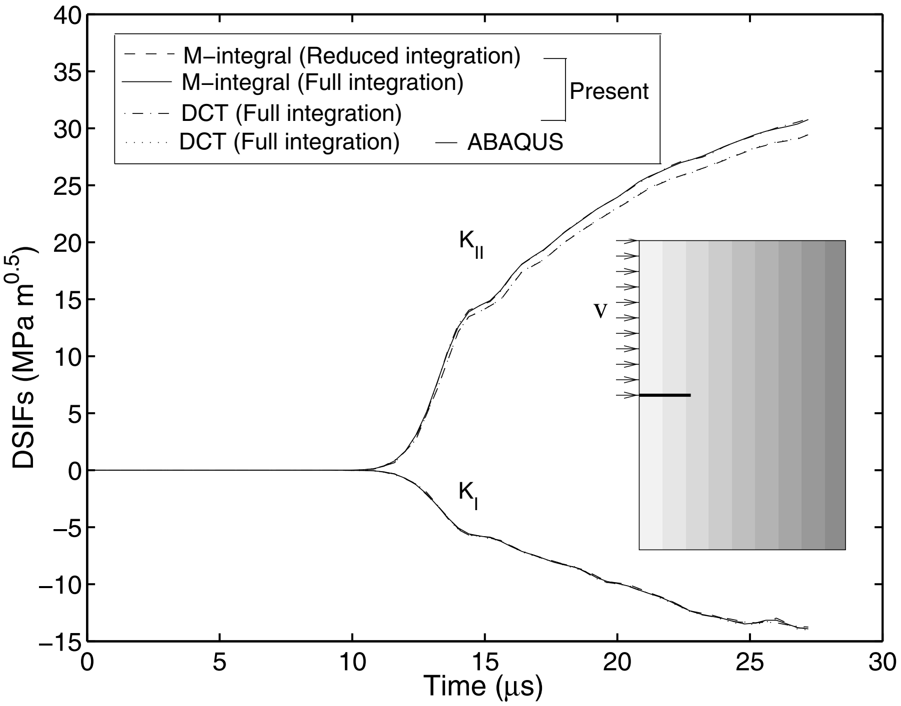

Figure 4.9: Comparison of numerical results between the M-integral and the DCT.

Figure 4.9 illustrates the variation of DSIFs with time and compares the DSIFs using the M-integral and the DCT from the present results with those using the DCT from ABAQUS. Notice that DSIFs using the M-integral are based on both reduced and full integration schemes, and DSIFs using the DCT are based on the full integration scheme. The abscissa and ordinate indicate time and DSIFs, respectively. DSIFs of K_I and K_{II} using the DCT for both the present and ABAQUS results are overlapped. Besides, the two different numerical schemes, i.e. the M-integral and the DCT, yield almost identical K_I values and close K_{II} values. The present numerical results of K_I and K_{II} using both full and reduced integration schemes are overlapped as shown in Figure 4.9, indicating that the influence of the selected integration orders on DSIFs for nonhomogeneous materials is negligible for this problem.

4.3 Remarks

The M-integral implemented here to incorporate material nonhomogeneity and dynamic effects is given by Eq. (2.37). Notice that the first three terms correspond to homogeneous materials under static conditions, the term $\rho \ddot{u}_i u_{i,1}^{aux}$ accounts for dynamic effects, and the terms $\sigma_{ij,j}^{aux} u_{i,1}$ and $C_{ijkl,1} \varepsilon_{kl}^{aux} \varepsilon_{ij}$ arise due to material nonhomogeneity.

For the verification of the dynamic finite element implementation, two examples are adopted: 1) Nonhomogeneous infinite plate [20] where stress fields are verified; 2) Homogeneous cantilever beam [55] where displacement fields are verified.

For the verification of the M-integral implementation, three cracked media are employed: 1) Nonhomogeneous unbounded plate with an arbitrarily oriented crack [33] where the terms $\sigma_{ij,j}^{aux} u_{i,1}$ and $C_{ijkl,1} \varepsilon_{kl}^{aux} \varepsilon_{ij}$ are verified because the terms account for material nonhomogeneity; 2) Homogeneous edge cracked semi-finite plate [35] where the term $\rho \ddot{u}_i u_{i,1}^{aux}$ is verified since the term accounts for dynamic effects; 3) Nonhomogeneous edge cracked semi-finite plate where the terms $\sigma_{ij,j}^{aux} u_{i,1}$, $C_{ijkl,1} \varepsilon_{kl}^{aux} \varepsilon_{ij}$ and $\rho \ddot{u}_i u_{i,1}^{aux}$ are verified. So, field quantities, which are the components of each term consisting in the M-integral, and individual terms in the M-integral are verified.

Chapter 5

Computational Results

With the code verified in the previous chapter, various problems are examined to evaluate DSIFs for homogeneous and nonhomogeneous materials and to explore fracture behavior for different material profiles. In this chapter, the following problems are considered:

- Homogeneous center cracked tension (CCT) specimen, which is a pure mode I problem.
- Nonhomogeneous CCT specimen with mixed-mode crack behavior.
- Homogeneous and nonhomogeneous rectangular plate with an inclined crack.
- Homogeneous and nonhomogeneous rectangular plate with cracks emanating from a circular hole.

In the examples, path-independence is assessed and the present numerical results are compared with reference solutions. The dynamic fracture behavior is investigated for different material gradations considering the influence of the time step on DSIFs, the relation between initiation time and the domain size, and the contribution of each distinct term in the M-integral.

5.1 Homogeneous CCT Specimen

This problem was first examined by Chen [9] and since then, it has been considered as a benchmark problem. Chen [9] determined mode I SIFs under step loading for a CCT specimen using a time dependent Lagrangian finite difference method (FDM). In his work, DSIFs were determined using the relation between stresses and SIFs around the crack tip.

Chen's [9] problem has been studied by many researchers. Brickstad [5] utilized the relation between SIFs and crack opening displacement (COD) to obtain DSIFs. Murti and Valliappan [39] employed the finite element method to determine DSIFs using the DCT.

Lin and Ballmann [36] revisited Chen's problem using the FDM. They employed a greater number of finite difference cells and obtained slightly different numerical results. Dominguez and Gallego [16] computed DSIFs using the BEM with quarter-point elements (QPEs). Sladek et al. [50, 51] used the $\hat{J}$ integral to determine DSIFs in the BEM context.

5.1.1 Problem Description

Consider a rectangular finite plate of width $2W$=20mm and height $2H$=40mm, with a center crack of length $2a$=4.8mm. Geometry, boundary conditions, finite element discretization, and three different M-integral domain contours are illustrated in Figure 5.1. The total mesh (see Figure 5.1 (b)) consists of 816 Q8 and 142 T6 2D plane strain elements. Notice that 8 T6 elements and 24 Q8 elements, which consist of four rings and eight sectors are employed as the crack tip template and lead to sufficient mesh refinement around the crack tips. The external force, $p(t)$, is applied instantaneously to both top and bottom edges with a step function, as shown in Figure 5.2. No other boundary conditions are prescribed. Young's modulus, mass density and Poisson's ratio are 199.992 GPa, 5000 Kg/m^3 and 0.3, respectively, and the corresponding wave speeds are

$$C_d = \sqrt{\frac{E(1-\nu)}{\rho(1+\nu)(1-2\nu)}} = 7.34\ mm/\mu sec, \tag{5.1}$$

$$C_s = \sqrt{\frac{E}{2\rho(1+\nu)}} = 3.92\ mm/\mu sec, \tag{5.2}$$

$$C_R \approx 0.928c_s \approx 3.63\ mm/\mu sec, \tag{5.3}$$

where C_d, C_s and C_R are the longitudinal wave, shear wave, and *Rayleigh* wave speeds [24], respectively. In the following simulation, we adopt the *average acceleration method* with a time step of $\Delta t = 0.05\mu s$, full integration, and consistent mass matrix.

5.1.2 Path Independence of the M-Integral for Homogeneous Materials

Path independent domain integrals such as the J and M-integrals are significant in fracture mechanics because accurate results can be obtained regardless of domain size. To evaluate path independence numerically, three different contours are selected, as illustrated in Figure 5.1(d). Figure 5.3 shows the normalized DSIFs versus normalized time for the three different contours. The time is normalized with respect to the dilatational wave speed (c_d), and the

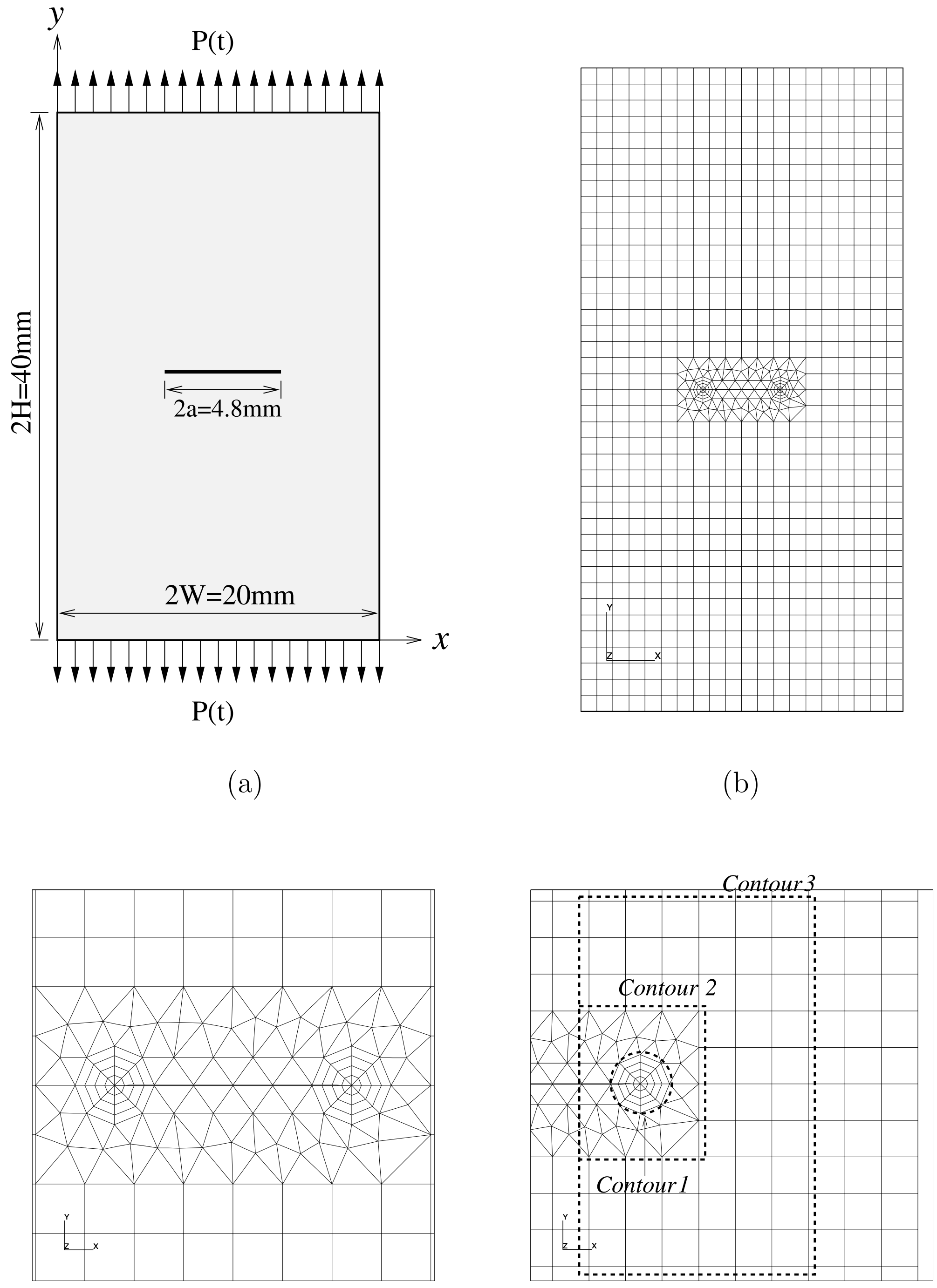

(a) (b)

(c) (d)

Figure 5.1: Benchmark CCT specimen: (a) geometry and boundary conditions; (b) mesh configuration for whole geometry; (c) mesh detail for the crack tip regions (8 sectors and 4 rings); (d) domain contours.

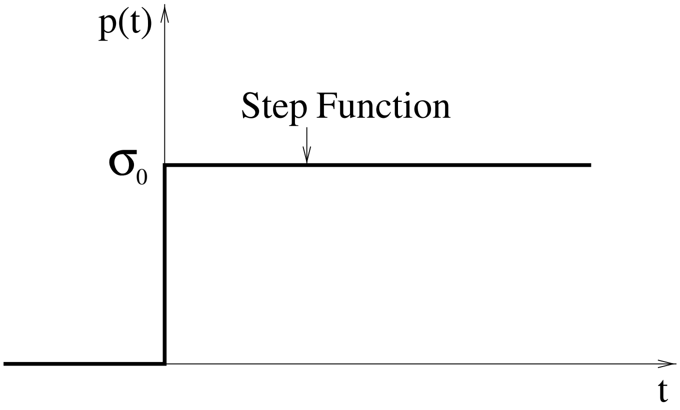

Figure 5.2: Applied load vs. time (step function)

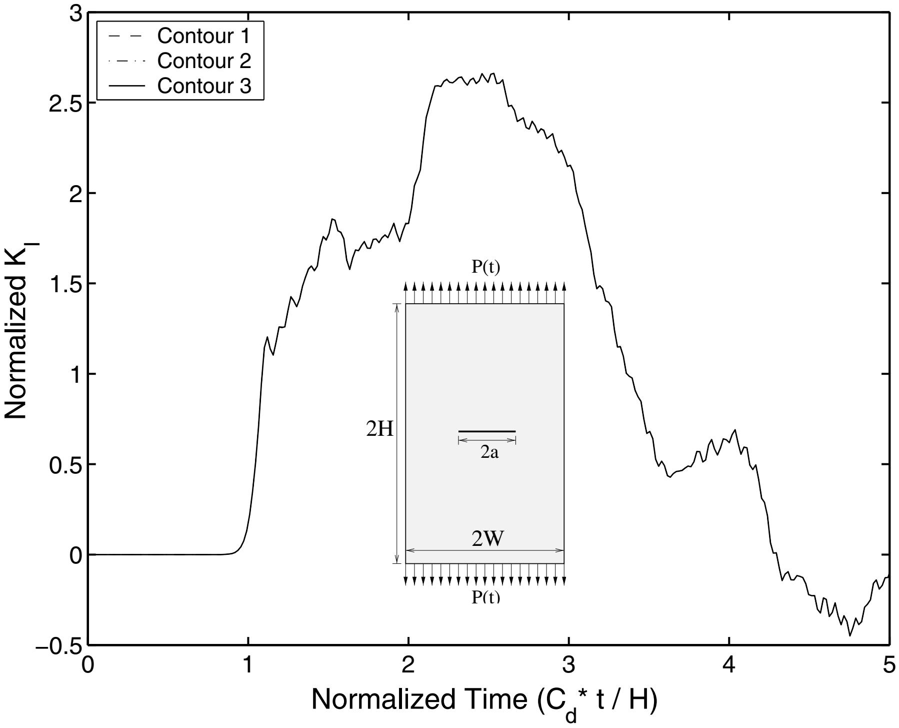

Figure 5.3: Numerical results for three different contours.

DSIFs are normalized with respect to

$$K_s = \sigma_0(\sqrt{\pi a}), \tag{5.4}$$

where the σ_0 is the magnitude of the applied stress and a is half of the total crack length. The similarity of numerical results for the three different contours demonstrate numerical path independence.

5.1.3 Comparison between J and M-Integrals

In 1968, Rice proposed the J integral which is equivalent to the energy release rate under static linear elastic conditions [46]. Since then, this method has been widely used and has been the basis of new methods proposed by many researchers. For instance, the J-integral can be decomposed to evaluate mixed mode SIFs [6, 32, 21]. Under dynamic loading conditions, it is necessary to include dynamic terms in order to obtain path independent DSIFs [59, 38]. Owing to significance of the J integral in fracture mechanics, we implemented Eq. (2.19) in the code employing the equivalent domain integral formulation (EDI) [44] and used the J-integral to verify the implementation of the M-integral.

This problem is a pure mode I problem since homogeneous materials are adopted. Therefore, a comparison of numerical results between using the J-integral and M-integral in terms of DSIFs is performed. Figure 5.4 compares DSIFs obtained using the J and the M-integrals. Up to the normalized time T_1 of 4.3 in Figure 5.4, the two numerical results match within 0.02 percent, which is expected because the M-integral is based on the J-integral. However, after the time T_1 both schemes yield nearly equal magnitude but they are opposite in sign as illustrated in Figure 5.4. Because J represents an energy which is always positive, the

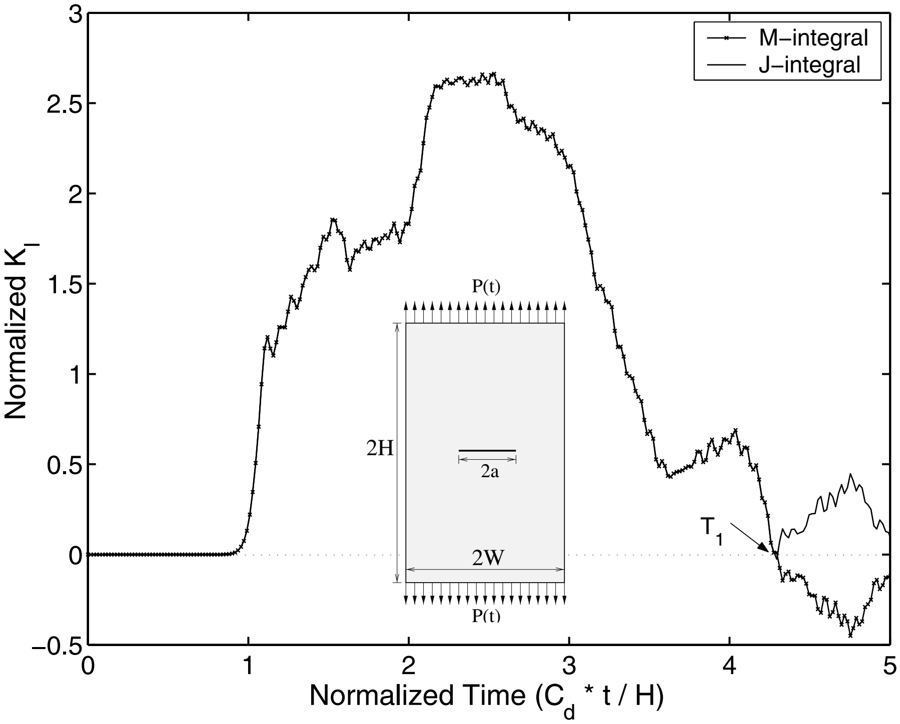

Figure 5.4: Numerical comparison between the J-integral and the M-integral

calculation of SIFs from J values, which follows

$$K = \sqrt{JE^{*}}, \tag{5.5}$$

always yields a positive value of K_I. This fact indicates that the J-integral may have limitations for dynamic problems because transient DSIFs often oscillate between positive and negative values. Here the negative mode I SIF simply indicates crack closure.

5.1.4 Comparison of Present Results with a Numerical Reference Solution

Lin and Ballmann [36] revisited Chen's problem using the FDM and obtained DSIFs utilizing the relation between SIFs and stress. Figure 5.5 compares the present numerical results with those of Lin and Ballmann [36]. A software named as DigXY was used to extract numerical values from graphical data in reference [36].

Overall, there is good agreement between the present numerical results and the reference solution. The reference solution shows a theoretical normalized initiation time of 1 as illustrated in Figure 5.5 because the step function is adopted for external loading. The present numerical results indicate an initiation time smaller than the theoretical value. However, the numerical initiation time approaches the theoretical value as the time step is decreased, which will be presented below (see Section 5.1.5). For the first peak, both results show a similar magnitude and corresponding time.

5.1.5 Comparison of Theoretical Initiation Time and First Peak

In this section, two important time locations, the initiation time and the first peak, during transient responses, are discussed by comparing the present numerical values with theoretical ones. The theoretical initiation time corresponds to the time necessary for a dilatational wave induced by external forces to reach a crack tip location, and in this case it equals H/c_d. Ideally, the numerical initiation time should coincide with the theoretical initiation time. In reality, numerical initiation values precede the theoretical values. For this problem, the normalized initiation time of the numerical results is 0.9 when time step 0.05μs is adopted, and the normalized theoretical initiation time is 1. Through numerical simulations, we observe that as the time step decreases, the numerical initiation time approaches the theoretical value of 1 in Figure 5.6. The normalized K_I for different time steps ($0.05\mu s$, $0.1\mu s$, $0.3\mu s$ and $0.5\mu s$) is plotted versus the normalized time in Figure 5.6.

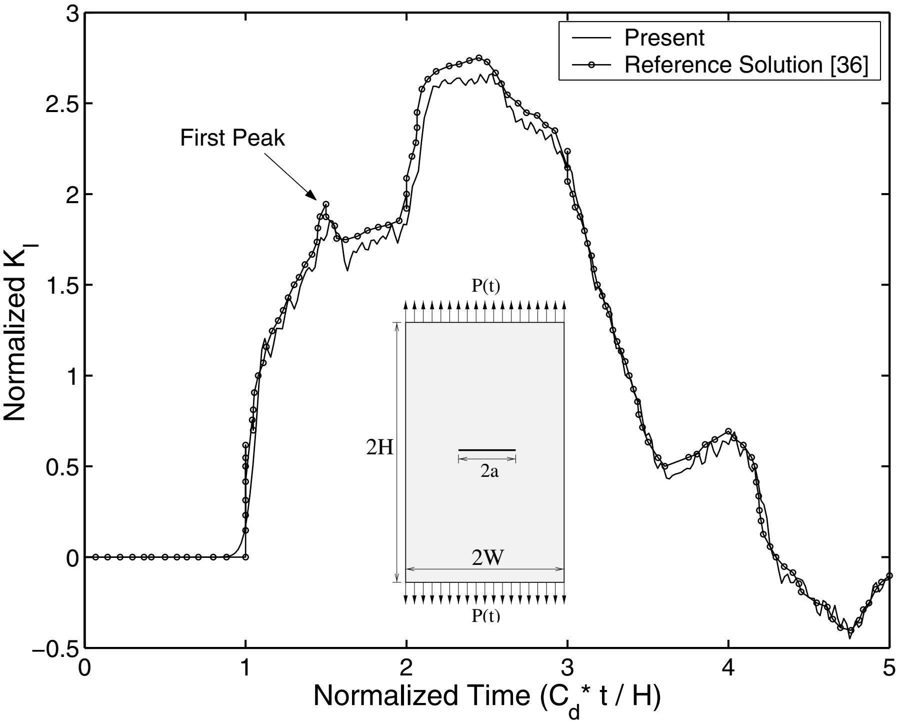

Figure 5.5: Comparison between the present numerical results and the reference solution by Lin and Ballmann [36]

The first peak, indicated in Figure 5.5, occurs in this problem when dilatational waves reach the crack tip, and generated *Rayleigh* waves travel to the opposite crack tip. At that instant, the *Rayleigh* waves cause compression at the crack tip and thus reduce the K_I values. The normalized theoretical time for this event is 1.485 and the present numerical value is 1.523 for a time step of $\Delta t = 0.05\ \mu s$. There is reasonably good agreement between these numbers with a relative error less than 3 %.

5.1.6 Sensitivity of Numerical Results with Respect to Time Step Size

For step loading, transient DSIFs are highly influenced by time step increment because the waves induced by this loading have a significant influence on crack tip fields, whereas for ramp loading, the crack tip fields are influenced primarily by the remote load. In the ramp loading, the load is always increasing with time and, as a consequence, the magnitude of SIFs increases monotonically with time and shows little variation due to propagating waves. Therefore, SIFs are not very sensitive to the time step increment for ramp loading.

Four different time steps, $0.05\mu s$, $0.1\mu s$, $0.3\mu s$ and $0.5\mu s$, are chosen to investigate the

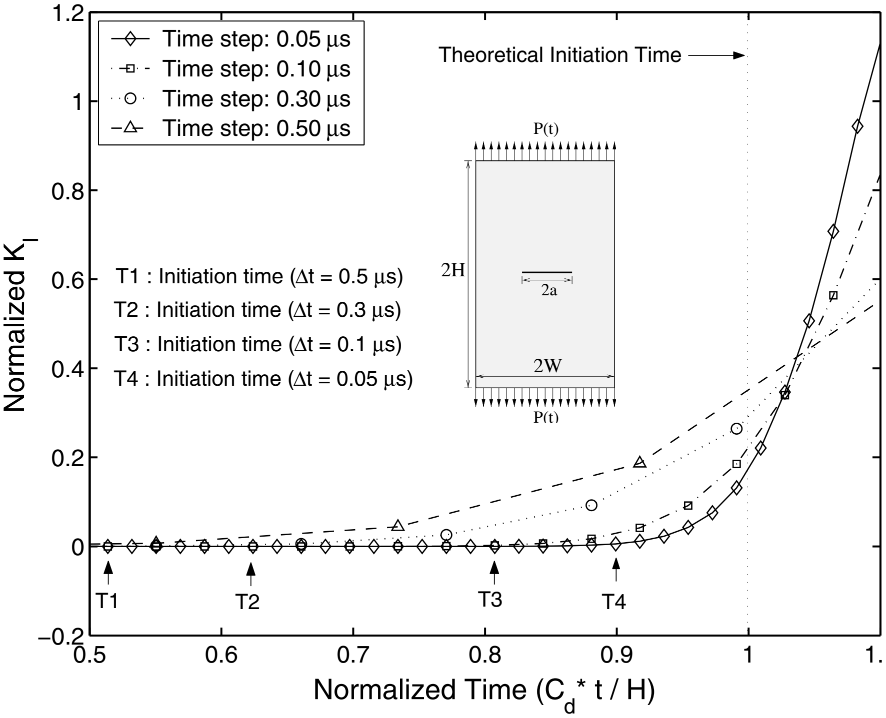

Figure 5.6: Initiation time for 4 different time steps.

influence of time step on the DSIFs for step loading. As illustrated in Figure 5.7, numerical results are highly influenced by the time step. The abscissa and ordinate represent normalized time and normalized K_I, respectively. As the time step decreases, the numerical results appear to converge. For the larger time steps, the difference between numerical results is especially pronounced near the peaks. This result indicates that for large time steps, the transient response cannot be captured accurately.

5.1.7 Discussion of M-Integral Terms

The M-integral based on the non-equilibrium formulation is given by Eq. (2.37), i.e.,

$$\begin{aligned} M &= \int_A \left\{ (\sigma_{ij}^{aux} u_{i,1} + \sigma_{ij} u_{i,1}^{aux}) - \sigma_{ik}^{aux} \varepsilon_{ik} \delta_{1j} \right\} q_{,j} dA \\ &+ \int_A \left\{ -C_{ijkl,1} \varepsilon_{kl}^{aux} \varepsilon_{ij} + \sigma_{ij,j}^{aux} u_{i,1} + \rho \ddot{u}_i u_{i,1}^{aux} \right\} q dA. \end{aligned} \tag{5.6}$$

The above expression consists of various terms which accounts for dynamic loading and nonhomogeneous materials. Now, we will investigate and discuss the contribution of each

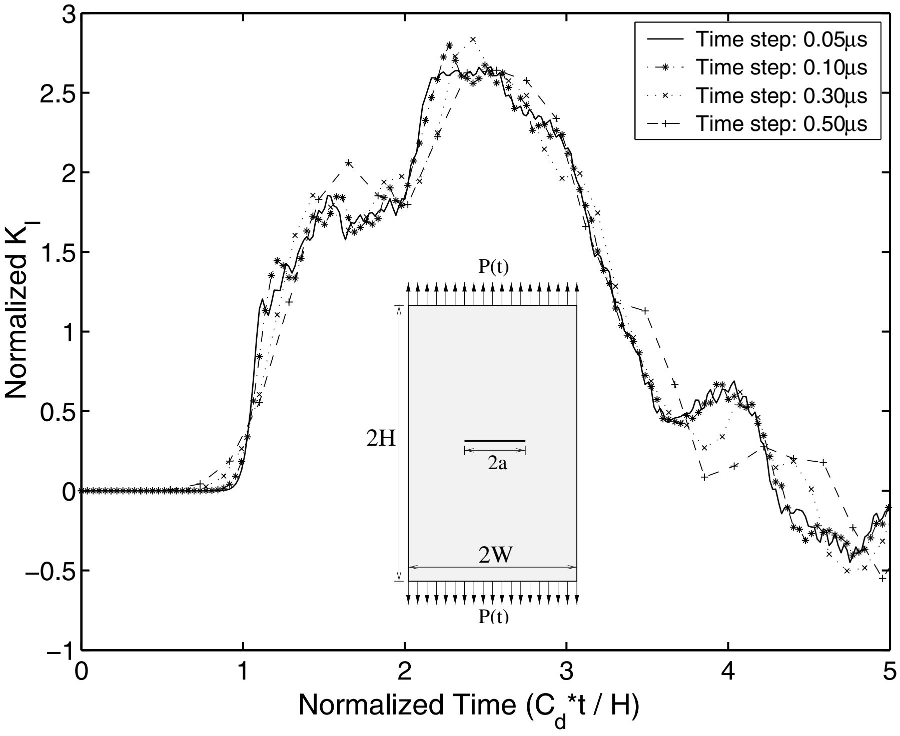

Figure 5.7: Normalized K_I at the right crack tip for 4 different time steps: 0.05 μs, 0.1μs, 0.3μs and 0.5μs.

term of the M-integral and its path independence. Let's define

$$\text{Term 1} = \int_A \sigma_{ij}^{aux} u_{i,1} q_{,j} dA \tag{5.7}$$

$$\text{Term 2} = \int_A \sigma_{ij} u_{i,1}^{aux} q_{,j} dA \tag{5.8}$$

$$\text{Term 3} = -\int_A \sigma_{ik}^{aux} \varepsilon_{ik} \delta_{1j} q_{,j} dA \tag{5.9}$$

$$\text{Term 4} = -\int_A C_{ijkl,1} \varepsilon_{kl}^{aux} \varepsilon_{ij} q dA \tag{5.10}$$

$$\text{Term 5} = \int_A \sigma_{ij,j}^{aux} u_{i,1} q dA \tag{5.11}$$

$$\text{Term 6} = \int_A \rho \ddot{u}_i u_{i,1}^{aux} q dA \tag{5.12}$$

Terms 1, 2, and 3 are the same as those for homogeneous materials under quasi-static conditions. Terms 4 and 5 arise due to material nonhomogeneity, and Term 6 is due to dynamic effects.

For this simulation, the contours used are shown in Figure 5.1 (a). Contour 1 includes 8

T6 and 24 Q8 elements, contour 2 contains 54 T6 and 24 Q8 elements, and contour 3 has 54 T6 and 72 Q8 elements. Figures 5.8 (a), (b), and (c) show the contribution of each term for contours 1, 2, and 3, respectively. The abscissa and ordinate represent normalized time and normalized K_I, respectively. Terms 4 and 5 are not included in Figures 5.8 because they are zero for homogeneous materials. For all contours, the contributions of Terms 1 and 2 are higher than those of the other terms. Terms 1, 2, and 3 follow the trend of the total K, whereas Term 6 oscillates. Two important phenomena are observed from this simulation. The first is the oscillatory nature of the contribution of Term 6 for different contours. The second is the relationship between initiation time and domain size.

For contour 1, illustrated in Figure 5.8 (a), the magnitude of Term 6 is small compared to that of other terms. But as the domain size increases (from contour 1 to contour 3), the magnitude of Term 6 increases as illustrated in Figure 5.9. It turns out that even if Term 6, which accounts for dynamic effects, is relatively small compared to other terms, the influence of this term in obtaining DSIFs becomes significant as the domain size increases. Therefore, this term must be taken into account to satisfy path-independence and to obtain correct DSIFs for dynamic problems.

Dilatational waves reach the boundary of larger domains earlier than the boundary of small domains. We now investigate initiation times of individual terms for different domain sizes. Figures 5.8 show the contribution of each term for the three contours. Because contour 1 is very small, the difference between the initiation time for each term and for the total DSIF is small (see Figure 5.8 (a)). However, for the larger contours 2 and 3 (see Figures 5.8 (b) and (c), respectively), it is clearly observed that Terms 1 and 6 initiate earlier than the total DSIF. Moreover, Terms 1 and 6 initiate earlier in the larger domain as shown in Figures 5.10 and 5.9, respectively. However, the change of initiation time for the different domain sizes is not pronounced for Terms 2 and 3 (see Figure 5.8). Notice that even if a few terms initiate earlier as the domain size increases, the initiation time of the total DSIF is independent of domain size, demonstrating path-independence (see Figure 5.3).

5.2 Nonhomogeneous CCT Specimen

Dynamic fracture behavior of a homogeneous CCT specimen is examined thoroughly in Section 5.1. In this section, various material profiles are adopted to investigate fracture behavior in a nonhomogeneous specimen. First, path independence of DSIFs for nonhomogeneous material is verified. Then, behavior of DSIFs at the right and left crack tips is explored.

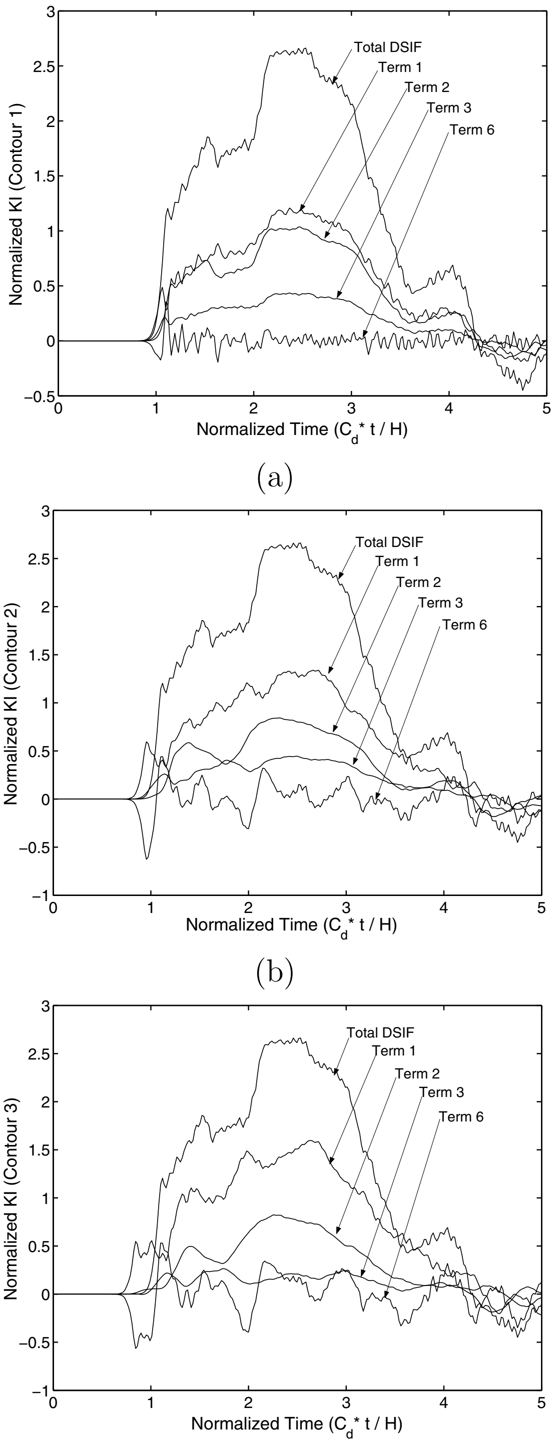

(a)

(b)

(c)

Figure 5.8: Normalized K_I for three different contours: (a) Contribution of each term for contour 1; (b) Contribution of each term for contour 2; (c) Contribution of each term for contour 3.

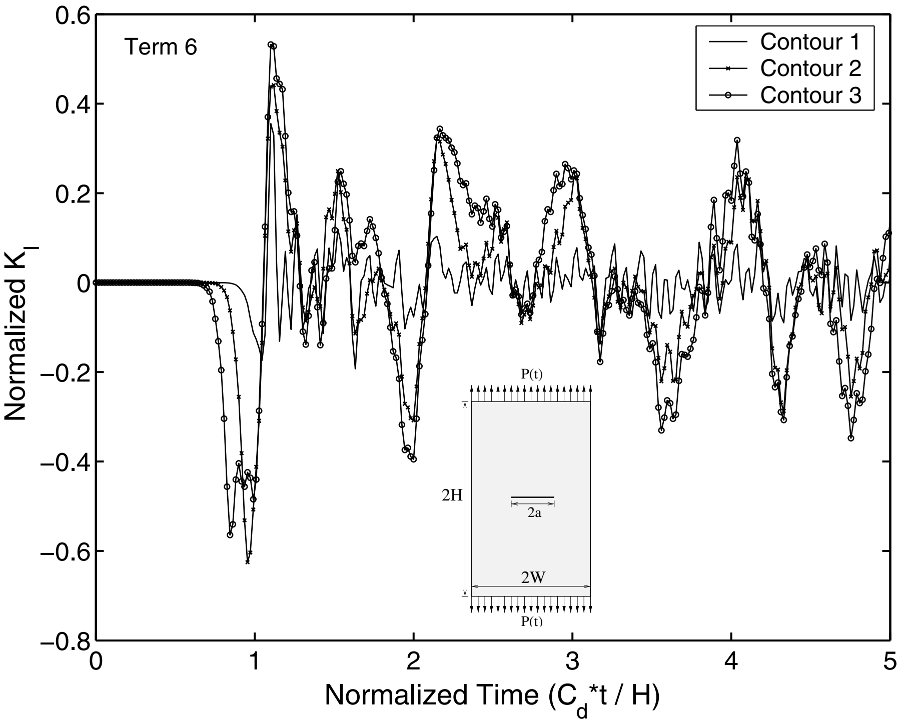

Figure 5.9: Contribution of Term 6 to normalized DSIFs for three different contours.

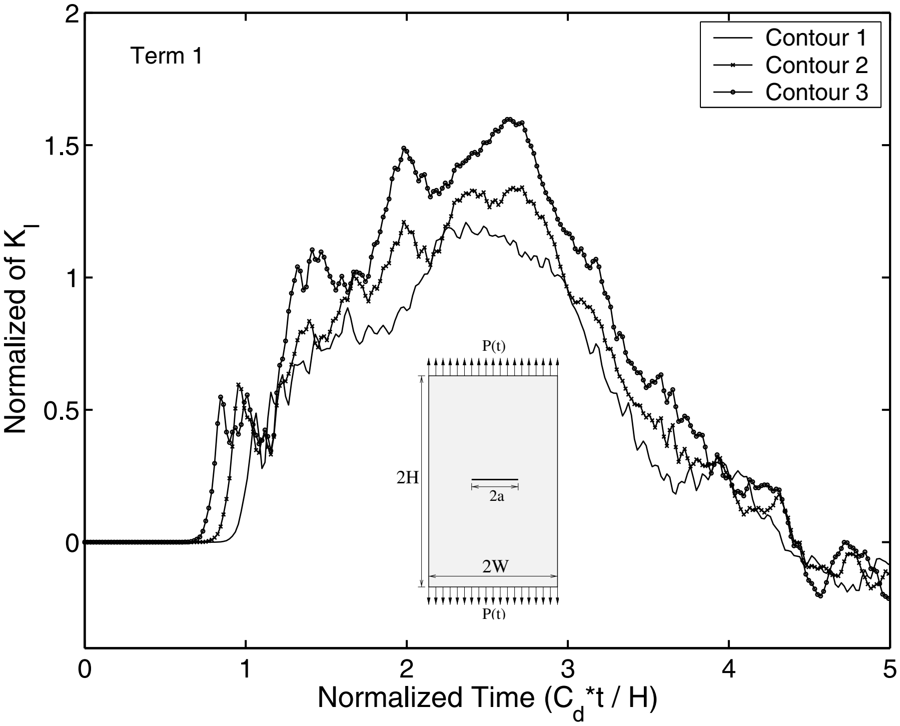

Figure 5.10: Contribution of Term 1 to normalized DSIFs for three different contours.

Young's modulus and mass density vary exponentially, such that $E/\rho \equiv$ constant, as given by

$$E = E_H \; exp(\beta_1 x + \beta_2 y), \tag{5.13}$$

$$\rho = \rho_H \; exp(\beta_1 x + \beta_2 y), \tag{5.14}$$

where E_H and ρ_H are Young's modulus and mass density for homogeneous materials and β_1 and β_2 are nonhomogeneity parameters along the x and y directions, respectively. When β_1 and β_2 are equal to zero, Eqs. (5.13) and (5.14) reflect homogeneous materials. A constant Poisson ratio of 0.3 is used. Plane strain elements with full integration and consistent mass matrices are adopted for the bulk elements. The *average acceleration method* is used with a time step of $\Delta t = 0.1\ \mu s$. The geometry and the boundary conditions are identical to those of homogeneous specimen analyzed in Section 5.1. Notice again that no other boundary conditions are prescribed except for the external loading.

5.2.1 Path Independence for Nonhomogeneous Materials

In this section, path independence of the M-integral for nonhomogeneous materials is demonstrated numerically. In order to employ severe material gradations, relatively high β values are chosen: $\beta_1 = 0.1$ and $\beta_2 = 0.1$. Material properties vary simultaneously along both the x and y directions according to coordinate system shown in Figure 5.1 (a).

Figure 5.11 shows DSIFs at the right crack tip for the same contours used in the homogeneous specimen (see Figure 5.1 (d)). The abscissa and ordinate are normalized by the homogeneous material constants, given by the dilatational wave speed of 7.34 $mm/\mu sec$ in expression (5.1) and the SIF in expression (5.4), respectively. Even with high material gradation, the normalized K_{II} is relatively small for this loading and geometry. The numerical results for the three different contours shown in Figure 5.11 are almost identical, demonstrating path independence for nonhomogeneous materials.

5.2.2 Exponentially Graded Materials in the x Direction

Here, various material gradations which vary only along the x direction are employed to investigate dynamic fracture behavior. For this analysis, the material gradation parameter β_1 is chosen as 0.0, 0.05, and 0.1, and β_2 equals 0.0. The ratio of the material properties at the left and right boundary ranges from 1.0 to 7.4.

Figures 5.12 (a) and (b) show the variation of normalized K_I at the left and right crack tips, respectively. The contour 3 shown in Figure 5.1 (d) is used to obtain DSIFs. The abscissa is normalized with respect to the homogeneous dilatational wave speed of

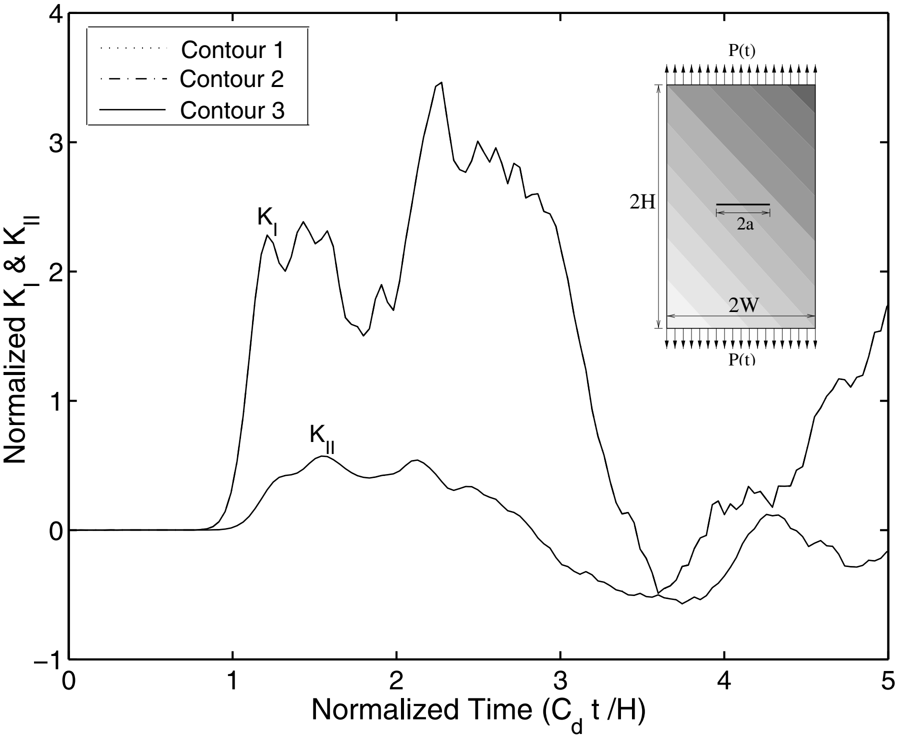

Figure 5.11: Normalized DSIFs for three different contours.

7.34 $mm/\mu sec$ in expression (5.1), and the ordinate is normalized with respect to the homogeneous material analytical SIF in expression (5.4), respectively. This analysis leads to three observations which are coincident with physical intuition. First, for both crack tips, the crack initiation time is the same regardless of material gradation. Initiation time depends on the dilatational wave speed which is a function of Young's modulus, Poisson's ratio, mass density, and geometry. Because the same exponential function describes the variation of Young's modulus and mass density ($E/\rho \equiv$ constant), these material gradations result in the same initiation time. Second, for the same β_1, the maximum normalized SIF at the left crack tip is smaller than that at the right crack tip. This is due to the fact that material at the right crack tip has higher stiffness than the material at the left crack tip. Third, as β_1 increases, the maximum DSIF decreases at the left crack tip, while it increases at the right crack tip. The values of K_{II} are relatively small, because cracks and material gradation are parallel to external loadings. Therefore, the variation of K_{II} is not discussed in this section.

5.2.3 Exponentially Graded Materials in the y Direction

In this section, we consider material properties that vary along the y direction. The material gradation parameter β_1 is set to 0.0, and β_2 is chosen as 0.0, 0.05 and 0.1. Since material

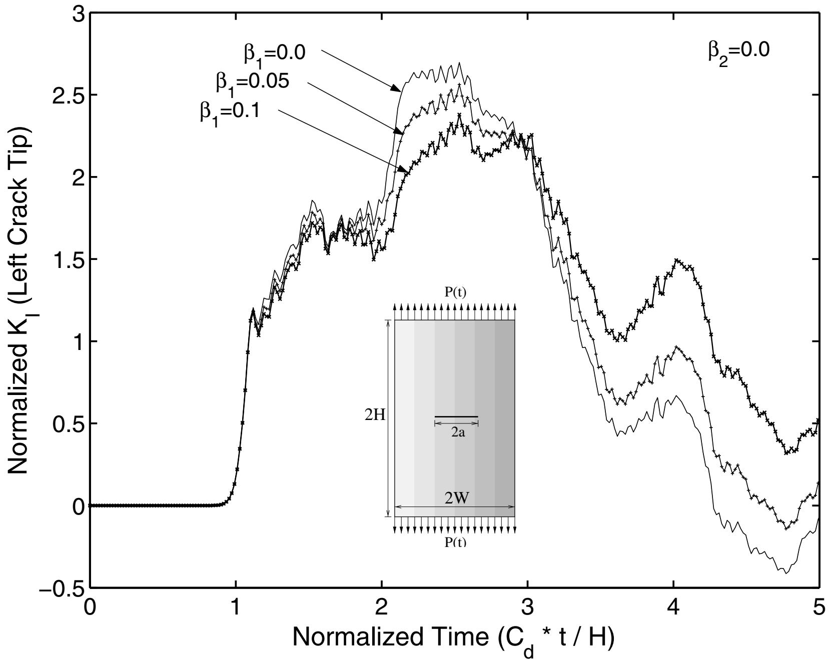

(a)

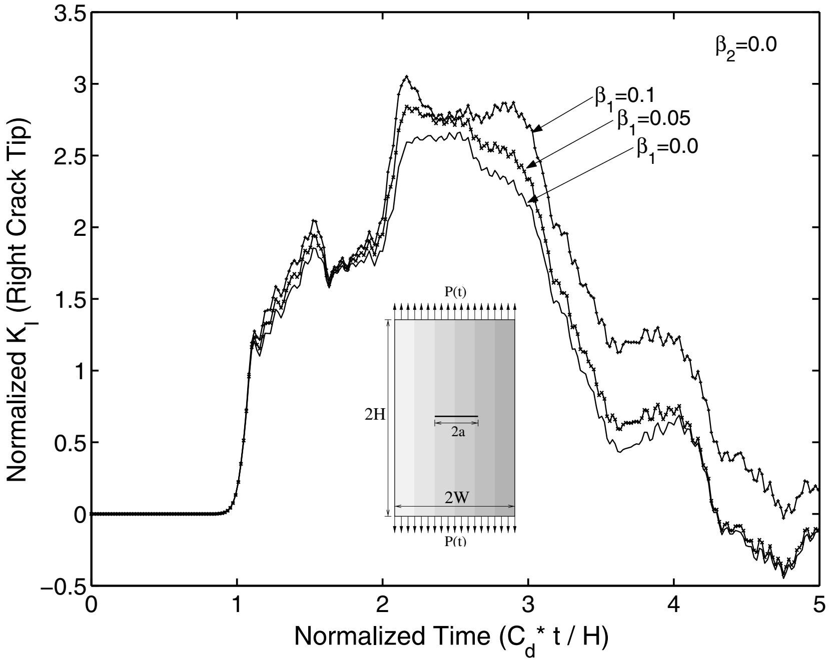

(b)

Figure 5.12: DSIFs for different material gradations along the x-direction: (a) Normalized K_I at the left crack tip; (b) Normalized K_I at the right crack tip

properties vary along the y direction, the material properties are the same at both crack tips. The ratios of material properties between the bottom and top edges are 1.0, 7.4 and 54.6, which correspond to β_1=0.0, 0.05, and 0.1, respectively.

Figure 5.13 shows mixed mode DSIFs at the right crack tip. The contour 3 shown in Figure 5.1 (d) is used to evaluate the M-integral. The abscissa indicates time normalized with respect to the homogeneous dilatational wave speed of 7.34 $mm/\mu sec$ in expression (5.1) and the ordinate indicates the DSIFs normalized as the homogeneous analytical SIF in expression (5.4). Since material gradations vary along the y direction, K_I is identical at both crack tips, while the magnitude of K_{II} at the left crack tip is equal in magnitude and opposite in sign to the value at the right crack tip. The initiation time at both crack tips remains the same for all cases of material gradation because the same exponential function describes Young's modulus and mass density. Values of K_{II}, induced by material gradients, are more significant with increasing β, whereas the maximum magnitude of K_I is relatively insensitive to β. Nevertheless, the magnitude of K_{II} is relatively small compared to that of K_I.

5.3 Rectangular Plate with an Inclined Crack

Chen and Wilkins [10] studied the problem of a rectangular plate with an inclined crack using the FDM and obtained results which have been questioned by several researchers. Murti and Valliappan [39] investigated this problem using QPEs with the FEM. Dominguez and Gallego [16], Fedelinski et al. [21], and Sladek et al. [51] investigated this problem using the BEM. Krysl and Belytschko [34], and Tabiei and Wu [52] explored the problem with the 3D EFG and the 3D FEM, respectively.

Consider an inclined crack of length $2a$=14.14 mm in a rectangular plate of width $2W$=30 mm and height $2H$=60 mm, as shown in Figure 5.14(a). Figures 5.14(b) and (c) illustrate the mesh for the whole geometry, and the four contours employed at each crack tip. The entire mesh consists of 206 Q8 and 198 T6 elements. Contour 1 includes only 8 T6 elements, contour 2 encloses 8 T6 and 24 Q8 elements, contour 3 contains 31 T6 and 24 Q8 elements, and contour 4 has 77 T6 and 26 Q8 elements. To obtain a reasonable mesh resolution near the crack tips, 4 rings and 8 sectors of elements are used. The external force, $p(t)$, is applied instantaneously to both the top and bottom edges with a step function (see Figure 5.2). No other boundary conditions are prescribed.

For the nonhomogeneous case, Young's modulus and mass density vary exponentially

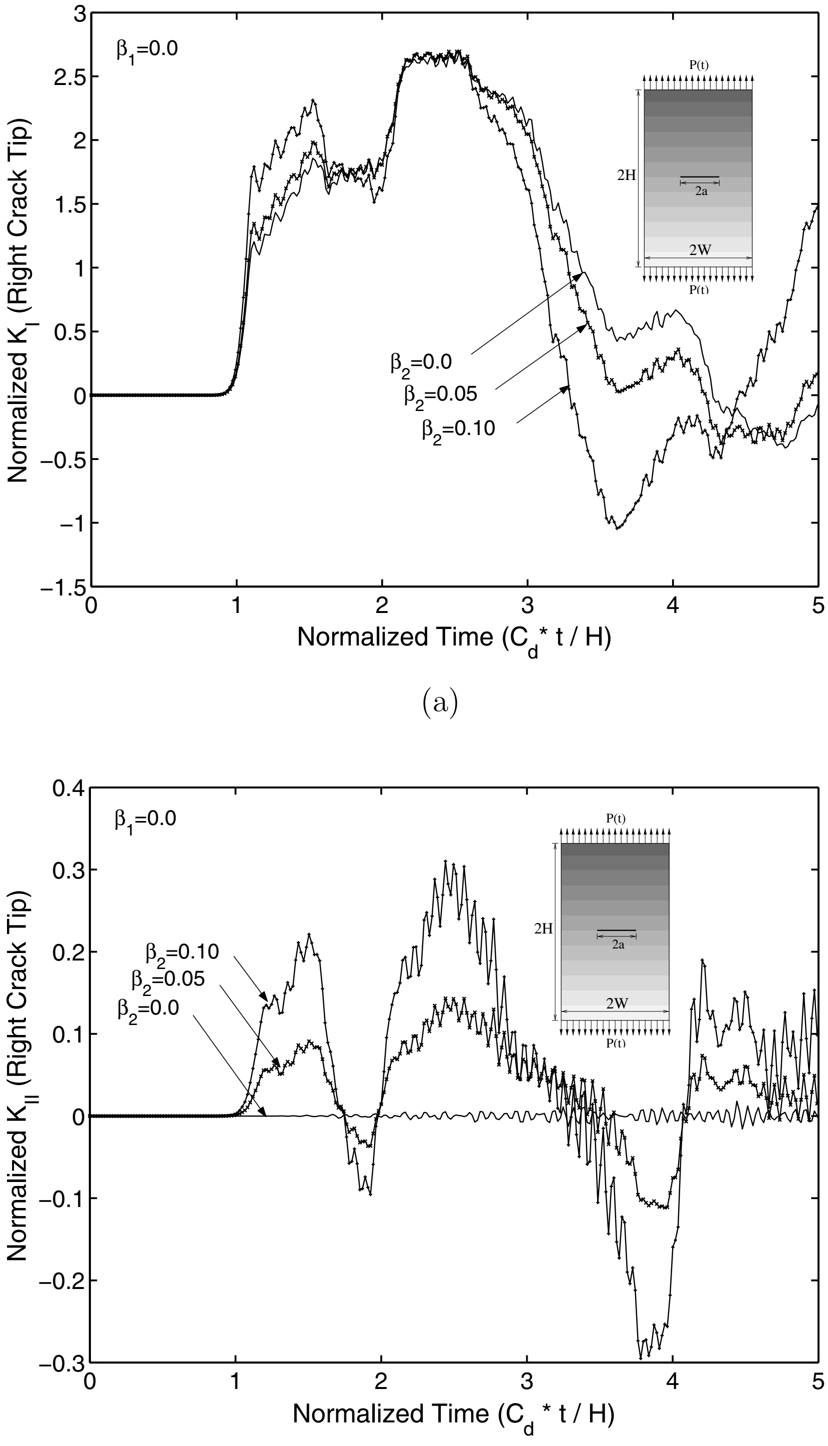

(a)

(b)

Figure 5.13: DSIFs for different material gradations along the y-direction: (a) Normalized K_I at the right crack tip; (b) Normalized K_{II} at the right crack tip.

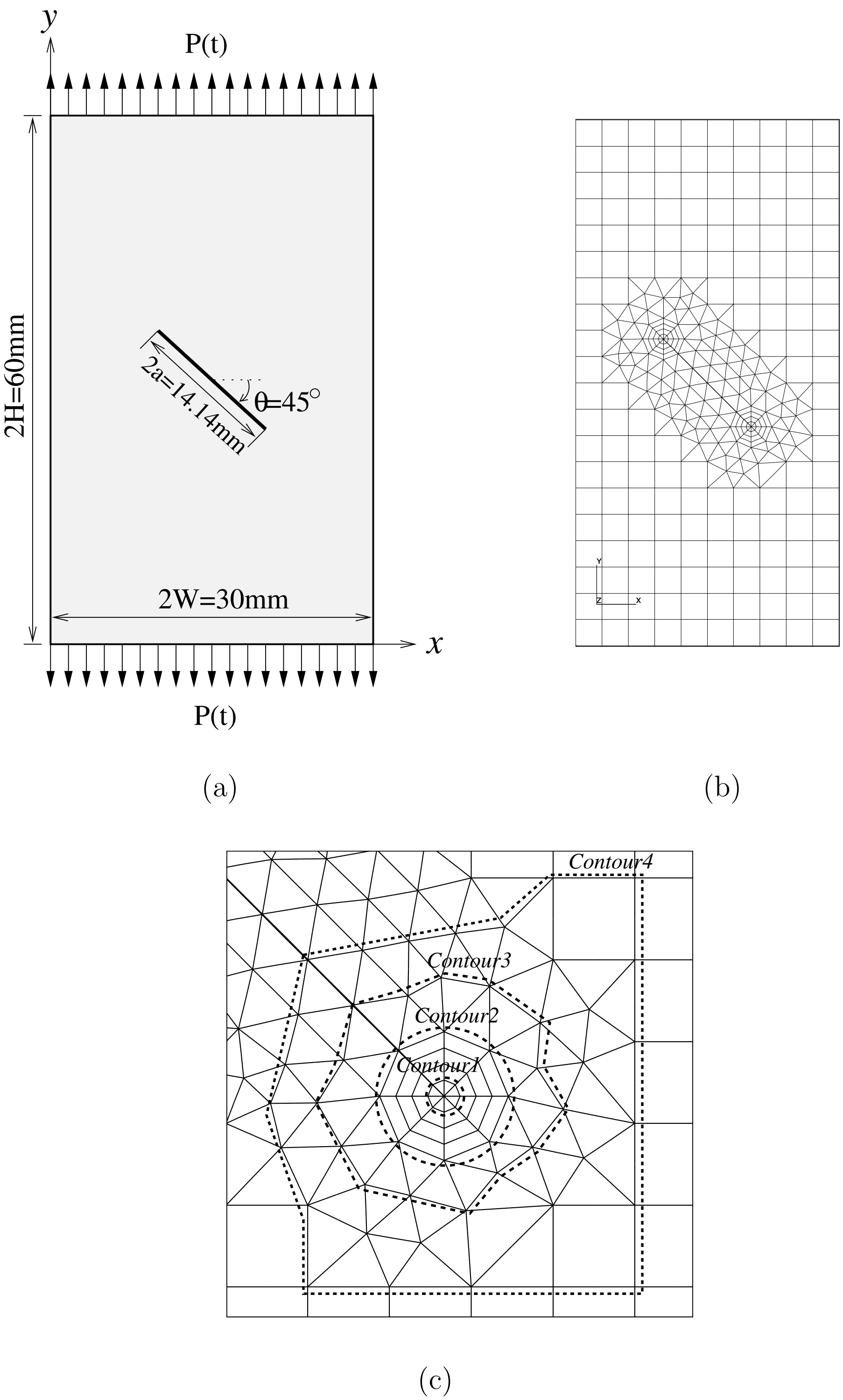

Figure 5.14: Rectangular plate with an inclined crack: (a) geometry and boundary conditions; (b) mesh configuration for whole geometry; (c) domain contours.

along the x and y directions, such that $E/\rho \equiv$ constant, according to

$$E = E_H \; exp(\beta_1 x + \beta_2 y) \tag{5.15}$$

$$\rho = \rho_H \; exp(\beta_1 x + \beta_2 y), \tag{5.16}$$

where E_H and ρ_H are Young's modulus and mass density for homogeneous material, and β_1 and β_2 are the material nonhomogeneity parameters that describe material gradation. When β_1 and β_2 equal zero, homogeneous material properties are recovered. A constant Poisson's ratio of 0.3 is employed. Plane strain elements with full integration are used. The *average acceleration method* is adopted with a time step $\Delta t = 0.1 \; \mu s$. For the mass matrix formulation, consistent mass matrix is employed.

In this section, we compare the present numerical results with current available reference solutions for homogeneous materials. Then, material gradations which vary along the x direction are adopted to investigate dynamic fracture behavior in terms of DSIFs for nonhomogeneous materials. The effects of domain sizes and the contribution of each term in the M-integral is explored.

5.3.1 Homogeneous Rectangular Plate

Here, the present numerical results are compared with available reference solutions for the homogeneous material case. With parameters β_1 and β_2 set to zero, the following homogeneous material properties are employed:

$$E = 199.992GPa, \;\; \rho = 5000Kg/m^3, \;\; \nu = 0.3. \tag{5.17}$$

The corresponding wave speeds are given by expressions (5.1), (5.2) and (5.3).

Figure 5.15 shows a comparison between the present numerical results and the reference solutions by Fedelinski et al. [21] who used a time-domain BEM, Dominguez and Allego [16] who used the dual BEM with the $\hat{J}$ integral, and Murti and Valliappan [39] who used FEM with QPEs. The abscissa indicates time. The ordinate indicates the DSIF normalized with respect to K_s given by expression (5.4).

The reference results plotted here are obtained from graphical data using special-purpose software. Up to $10\mu s$, the difference between the results is not significant. After that time, the discrepancy among the results becomes greater when the influence of reflected waves becomes significant. This implies that the various numerical schemes differently predict the transient fracture response which is highly influenced by propagating waves reflected from the boundary and crack surfaces. Up to $10\mu s$, the present results match well with the solution by Dominguez and Allego [16], and afterwards, the present results are within the range of the other solutions. Moreover, the present results show more oscillations (small amplitude) than the other solutions.

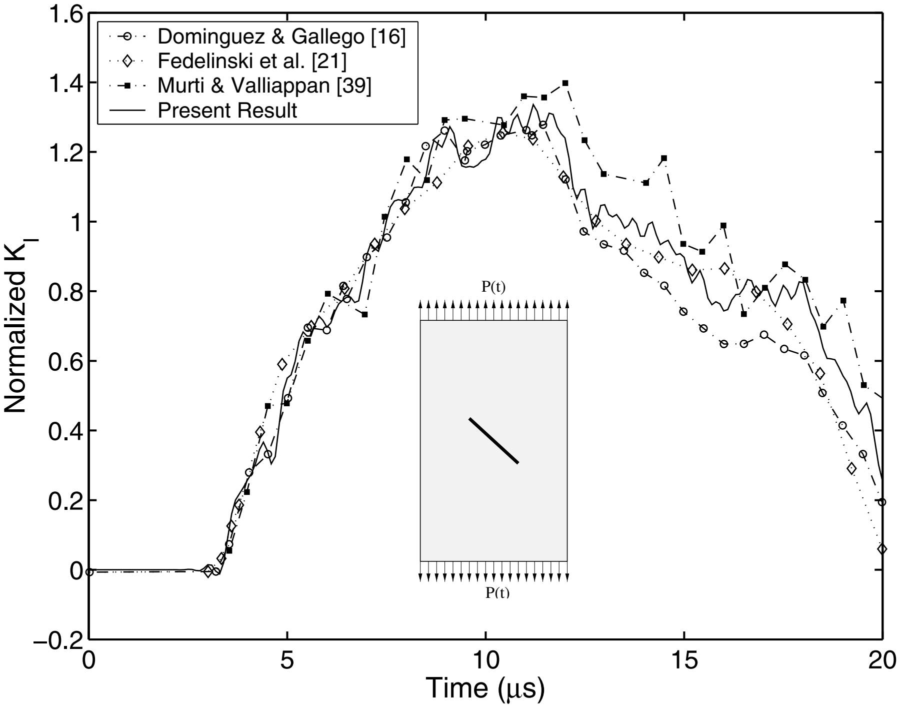

Figure 5.15: Numerical comparison between the present results and the reference solutions [16, 21, 39]

5.3.2 Exponentially Graded Materials in the x Direction

Material properties varying along the x direction are employed to investigate DSIFs for nonhomogeneous materials. The material gradation parameter β_1 is chosen as 0.0, 0.05, 0.1 and 0.15, and β_2 is set to zero. The ratio of material properties at the left and right boundaries ranges from 1.0 to 90.0. Although this high material ratio, i.e. 90, is not realistic, such high material gradation is adopted in order to clearly observe the influence of different material profiles on the variation of DSIFs.

Figure 5.16 illustrates the variation of mixed mode DSIFs at the left and right crack tip locations. The ordinate indicates normalized DSIFs and the abscissa indicates time up to $22\mu s$. Both crack tips have the same initiation time for the different material gradations because Young's modulus and mass density follow the same exponential function. As the

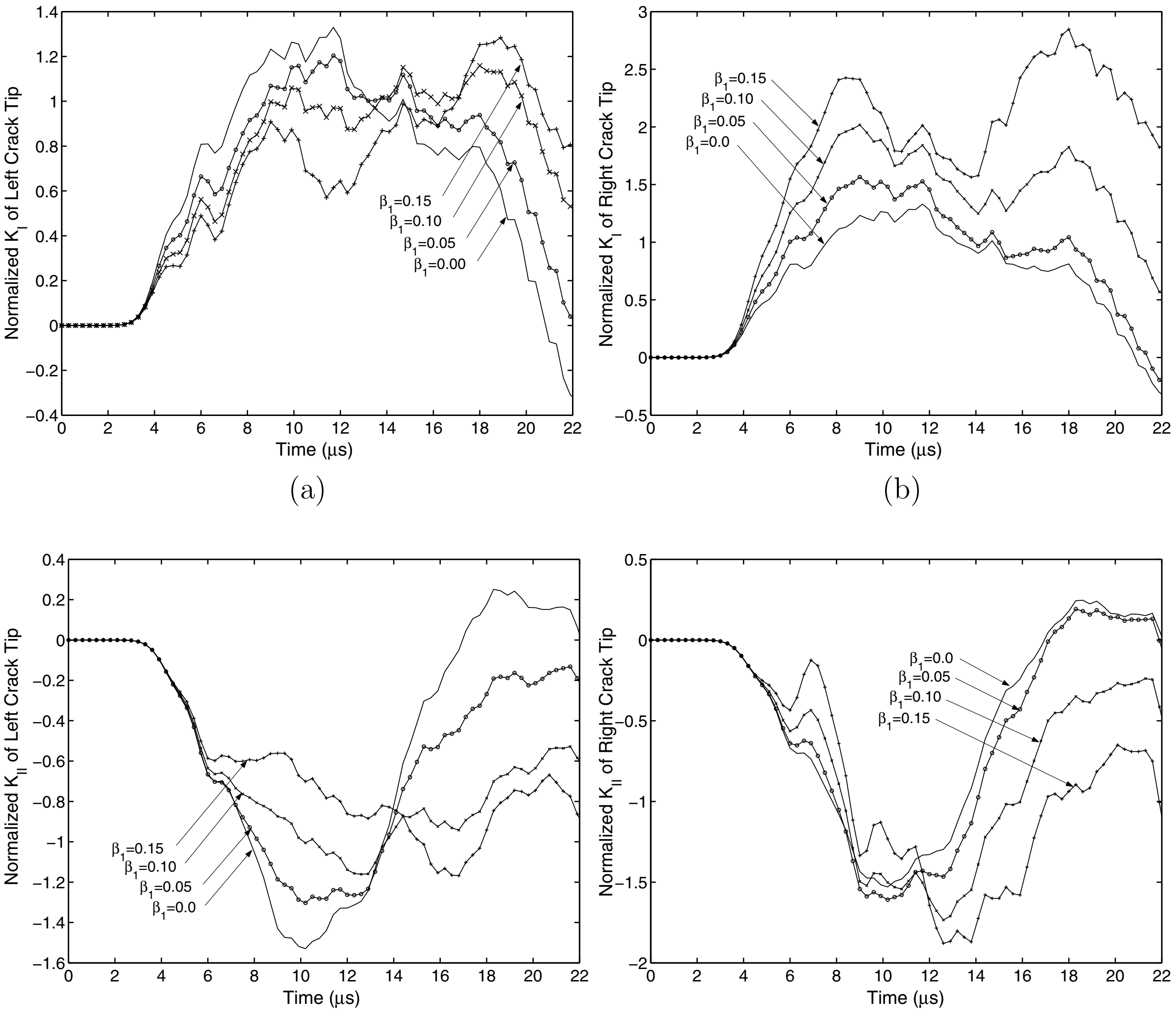

(a) (b)

(c) (d)

Figure 5.16: Mixed mode DSIFs: (a) Normalized K_I at the left crack tip; (b) Normalized K_I at the right crack tip; (c) Normalized K_{II} at the left crack tip; (d) Normalized K_{II} at the right crack tip

parameter β_1 increases, the magnitude of $K_I(t)$ at the right crack tip increases. At the left crack tip, up to around $15\mu s$, the magnitude of $K_I(t)$ is larger for smaller values of β_1 and after that time, the magnitude of $K_I(t)$ becomes smaller for smaller values of β_1. For $K_{II}(t)$, as β_1 increases, the absolute magnitude of $K_{II}(t)$ at both crack tips first decreases and then increases. Moreover, the absolute value of maximum $K_I(t)$ at the right crack tip is higher than that at the left crack tip as β_1 increases. This behavior is reasonable because the material property values at the right crack tip are higher than those at the left crack tip.

5.3.3 Discussion of M-Integral Terms for Nonhomogeneous Materials

In Section 5.1.8, the contribution of each term was explored throughly for homogeneous materials. To account for material nonhomogeneity in the current specimen, the M-integral includes Terms 4 and 5. In this section, we examine the influence of each term of the M-integral. Also, we discuss the influence of domain size on the magnitude of Terms 4, 5 and 6, which account for nonhomogeneity and dynamic effects. The four different contours illustrated in Figure 5.14 (a) are used. The value of β_1 is chosen as 0.1 and β_2 is chosen as zero, i.e. $(\beta_1, \beta_2) = (0.1, 0.0)$. The element type, numerical schemes and time step are the same as in the homogeneous case for this specimen.

Figure 5.17 shows the contribution of individual terms to normalized DSIFs, $K_I(t)/K_s$ and $K_{II}(t)/K_s$ where K_s is given by expression (5.4), versus time at both the right and left crack-tip locations for the four different contours. The different terms are given by Eqs. (5.7) through (5.12). For contour 1, Terms 4 and 5, representing nonhomogeneous material effects, and Term 6, accounting for dynamic effects, are small. This shows numerically that the influence of inertia and nonhomogeneity on DSIFs is almost negligible very near the crack tip. For other contours, the contribution of Terms 4, 5 and 6 to DSIFs is larger than for contour 1. Overall, the trend and contribution of Terms 1 and 2 are similar for all contours. During the time period up to 22 μs, Terms 1, 2, 3 and 5 are positive, Term 4 is negative, and Term 6 oscillates. Notice that even though the contribution of each term varies for different contours, the total K is the same for each contour, demonstrating path independence. We now discuss two important observations: 1) The effects of domain size on nonhomogeneous and dynamic terms; 2) the relationship between initiation time and domain size.

Figures 5.18 (a), (b) and (c) respectively illustrate the contribution of Terms 4, 5 and 6 for different domain sizes. For contours 2, 3 and 4, the contribution of the nonhomogeneous and dynamic terms is significant. As we increase the domain size from contour 1 to contour 4, the contribution of Terms 4 and 5, which account for nonhomogeneity, increases. Term 6, which represents dynamic effects, increases in magnitude from contour 1 to contour 4. Therefore, if we neglect these terms in evaluating the M-integral for dynamic loading of nonhomogeneous materials, path independence is violated and accuracy worsens as the domain size increases.

Figures 5.19 (a) and (b) show the initiation time of each term for contours 1 and 4, respectively. For both figures, the abscissa indicates time from 1.5 μs to 3.5 μs and the ordinate indicates normalized $K_I(t)$. For contour 1, each term and the total DSIF initiate at the same time denoted by T in Figure 5.19 (a). For contour 4, however, the initiation time of Terms 1, 2, 3 and 6, T_1 in Figure 5.19 (b), is less than that of total DSIF, which is

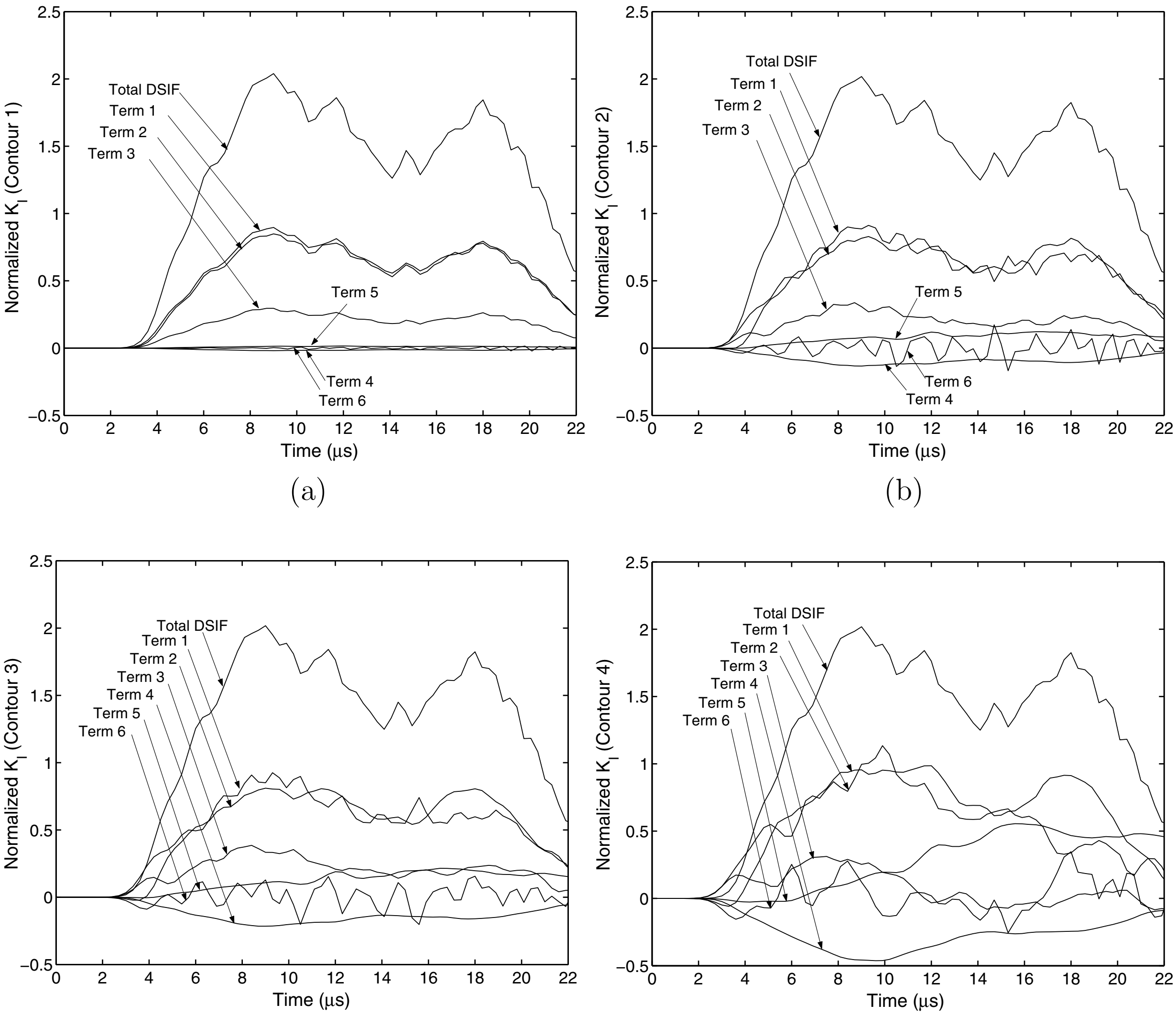

(a) (b)

(c) (d)

Figure 5.17: Contribution of individual terms to the DSIFs for different contours: (a) Contribution of each term for contour 1; (b) Contribution of each term for contour 2; (c) Contribution of each term for contour 3; (d) Contribution of each term for contour 4

reasonable because waves reach the boundary of larger domains earlier than the boundary of small domains. On the contrary, initiation time T of Terms 4 and 5 and total DSIF are almost identical. Even though a few terms initiate early, the initiation time of the total DSIF for different contours is the same satisfying path independence.

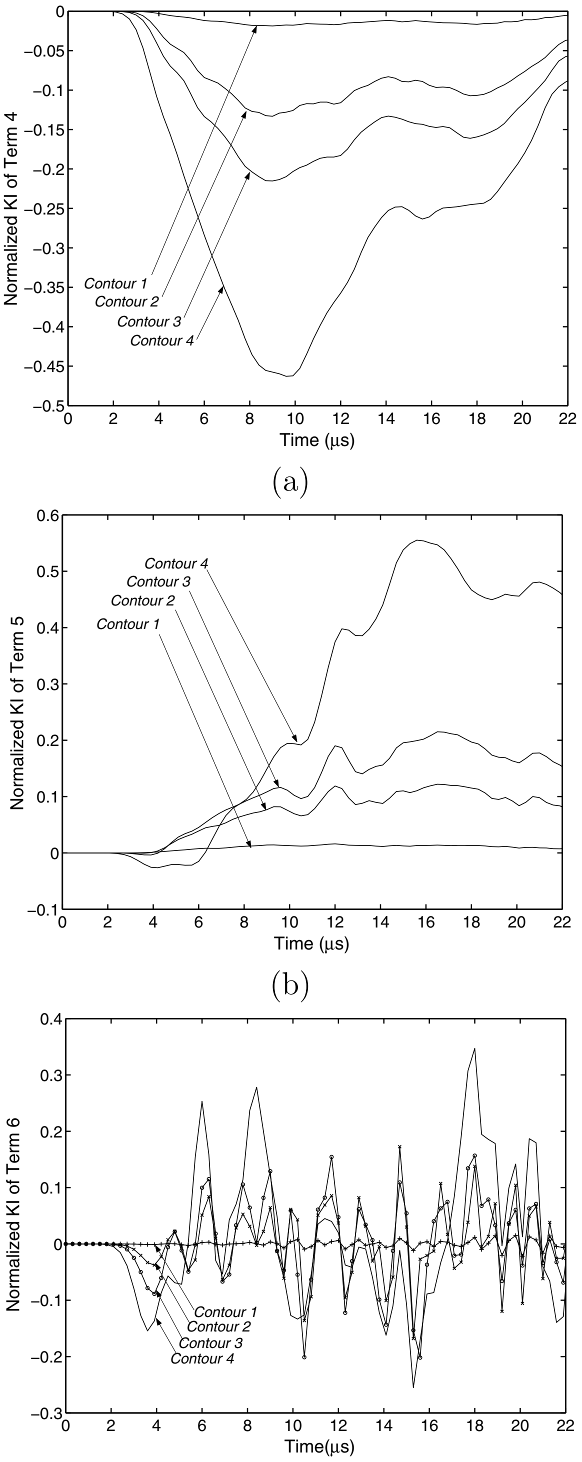

(a)

(b)

(c)

Figure 5.18: The influence of domain size on the contribution of each term to DSIFs: (a) Term 4 contribution; (b) Term 5 contribution; (c) Term 6 contribution.

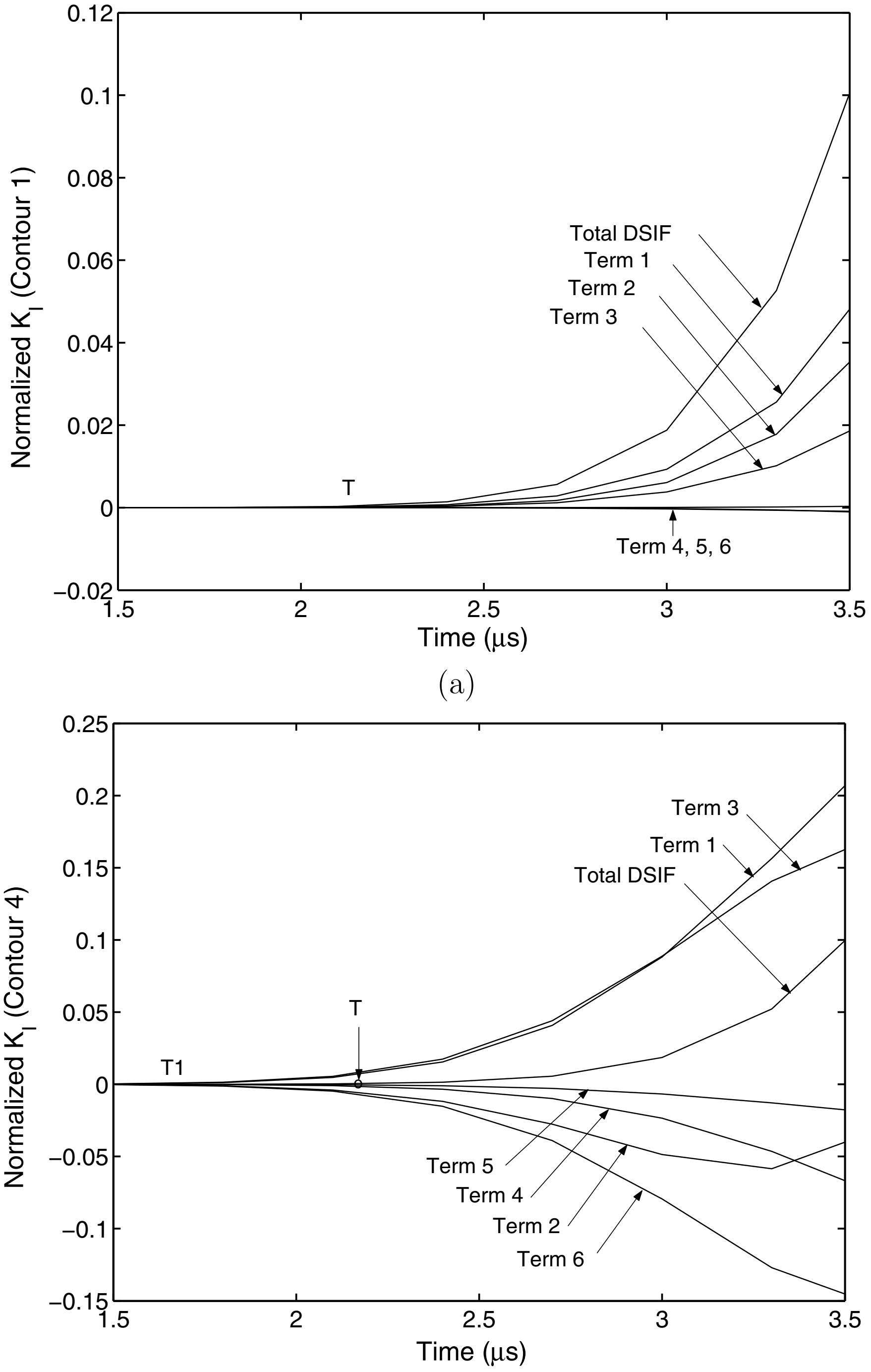

(a)

(b)

Figure 5.19: Relationship between domain size and initiation time of each term in the M-integral: (a) Normalized K_I at right crack tip for contour 1; (b) Normalized K_I at right crack tip for contour 4

5.4 Rectangular Plate with Cracks Emanating from a Circular Hole

Fedelinski el al. [21] used the dual BEM and $\hat{J}$ integral to determine DSIFs in a rectangular plate with cracks emanating from a circular hole. A decomposition procedure was employed for mode mixity. Various angles which range from 0° to 60° were adopted to investigate fracture behavior in terms of the variation of DSIFs. In this study, crack angles of 30° are chosen to verify DSIFs for homogeneous materials and to investigate the influence of material gradation on DSIFs for nonhomogeneous materials.

Figure 5.20 (a) illustrates a rectangular finite plate with a width $2W$=30 mm and a height $2H$=60 mm containing a hole of radius r=3.75 mm. Two cracks extend from the hole, and the length between the two crack tips is 15mm. The cracks are inclined at 30° clockwise from horizontal. Figures 5.20 (b), (c) and (d) show the mesh configurations for the whole geometry, and mesh detail for near the hole and the crack tips. A crack tip template of 12 sectors and 4 rings of elements provide sufficient mesh refinement around the crack tip regions, which is crucial to obtain reliable numerical results. Step loading, which is illustrated in Figure 5.2, is applied to both the top and bottom edges. No other boundary conditions are prescribed.

In this mesh, 1350 Q8 and 204 T6 plane strain elements are used with full integration. The *average acceleration method* is adopted with a time step of $\Delta t = 0.1\ \mu s$, and consistent mass matrix is employed.

5.4.1 Homogeneous Plate

A comparison between the present numerical results and a reference solution is carried out. For the homogeneous plate, the material properties described in Section 5.3.1 are used. The corresponding wave speeds are given by expressions (5.1), (5.2) and (5.3).

Figure 5.21 shows the comparison between present numerical results at the right crack tip and the solution by Fedelinski et al. [21]. The reference results plotted here are obtained from graphical data using special-purpose software. The abscissa indicates time up to 20 μs. The DSIFs are normalized by K_s given in expression (5.4). The values of K_{II} in Fedelinski et al. [21] are positive, while the present numerical values of K_{II} are negative up to around 18 μs in Fig. 5.21. This might be due to different sign convention in shear. The same magnitude but opposite sign of the K_{II} in the reference solution is compared with the present numerical values of K_{II}. Greater but acceptable difference is found between K_I values than between K_{II} values. The difference may be due to different numerical schemes, different domain

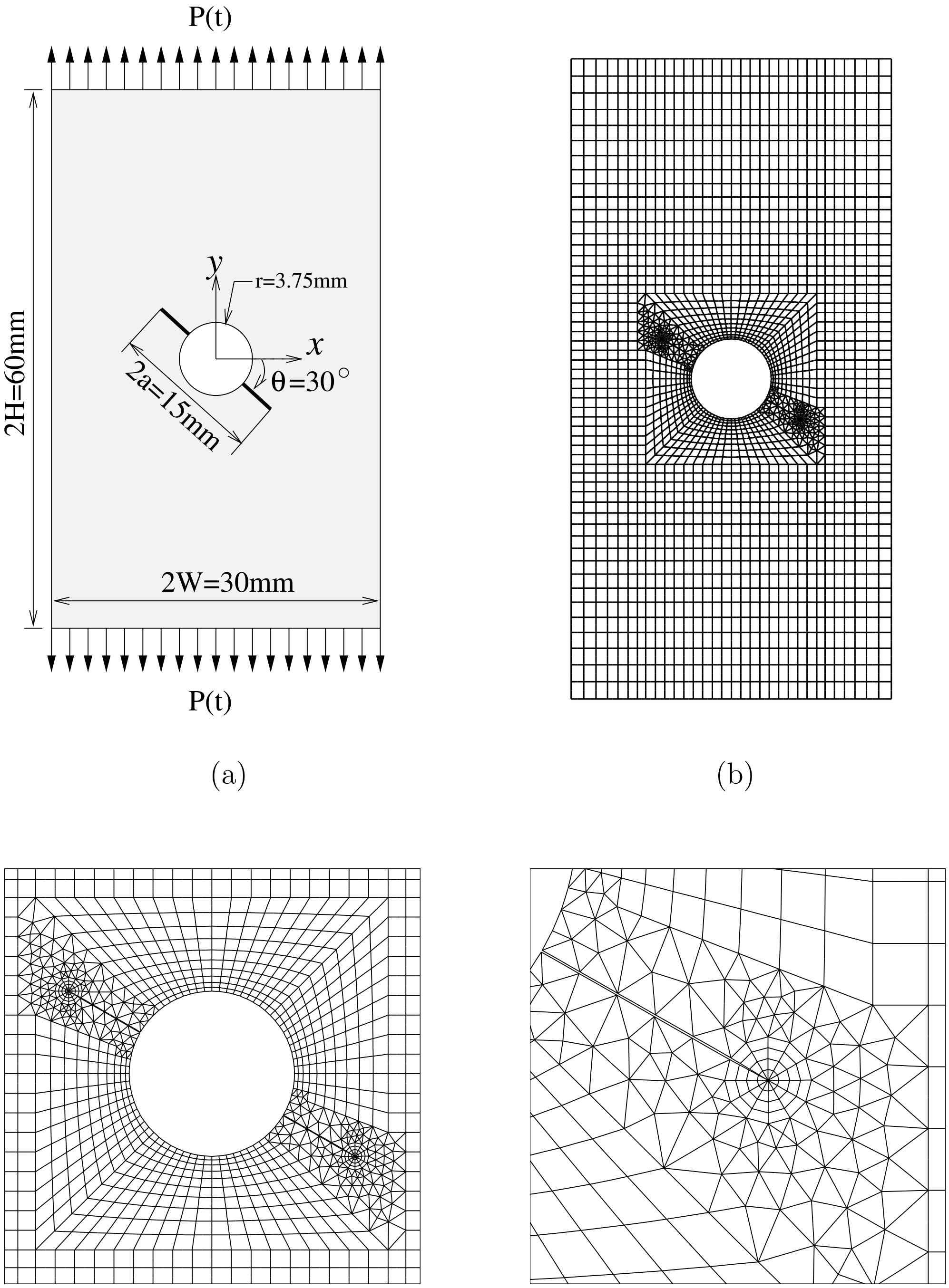

(a)

(b)

(c)

(d)

Figure 5.20: Rectangular plate with cracks emanating from a circular hole: (a) geometry and boundary conditions; (b) mesh configuration for whole geometry; (c) mesh details for both crack tip regions (d) mesh details for the right crack tip (12 sectors and 4 rings).

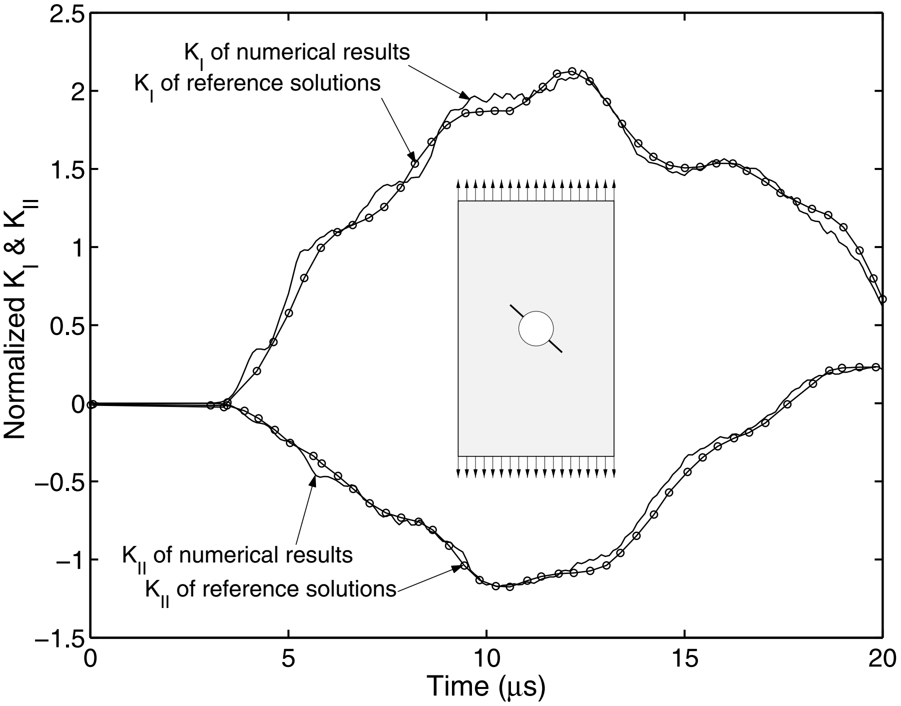

Figure 5.21: The comparison between the present numerical results and reference solutions [21]

discretization, and different conservation integrals; $\hat{J}$ integral and M-integral. Overall, the present numerical results agree well with this reference solution.

5.4.2 Nonhomogeneous Plate

Unlike in previous examples, realistic nonhomogeneous material properties are adopted here to investigate fracture behavior. Rousseau and Tippur [48] prepared three point bending specimens made of epoxy and solid soda-lime glass spheres. The material properties of the current specimen follow the values provided in Rousseau and Tippur [48] and assume linear variation of material properties in the x direction, described by

$$E(x) = (244x \ + \ 7471) \ (MPa), \tag{5.18}$$

$$\rho(x) = (28.8x \ + \ 1380) \ (Kg/m^3). \tag{5.19}$$

A constant Poisson's ratio of 0.3 is used. Table 5.1 shows material properties and the corresponding dilatational wave speed along the left edge and the right edge. Notice that the longitudinal wave speed is different at each location due to the different variation between

Young's modulus and mass density.

Table 5.1: Material properties and dilatational wave speed along the left and right edges.

	Young's modulus	Mass density	Longitudinal wave speed
Left edge	3811 MPa	948 Kg/m^3	2.33 $mm/\mu s$
Right edge	11130 MPa	1812 Kg/m^3	2.88 $mm/\mu s$

Normalized mixed-mode DSIFs at both the right and left crack tip locations for homogeneous and nonhomogeneous materials are plotted versus time in Figure 5.22. The ordinate indicates DSIFs normalized by K_s (see expression (5.4)) and the abscissa is time up to 40 μs. Since initiation time of DSIFs depends on the dilatational wave speed, first the DSIFs for homogeneous materials initiate, then the DSIFs at the right crack tip for the nonhomogeneous case initiate, and finally, the DSIFs at the left crack tip for the nonhomogeneous case initiate as shown in Figure 5.22. At any given time of the transient response, the magnitude of K_I at the right crack tip is higher than that at the left crack tip for the nonhomogeneous case. This is due to the fact that the values of material properties at the right crack tip are higher than those at the left crack tip.

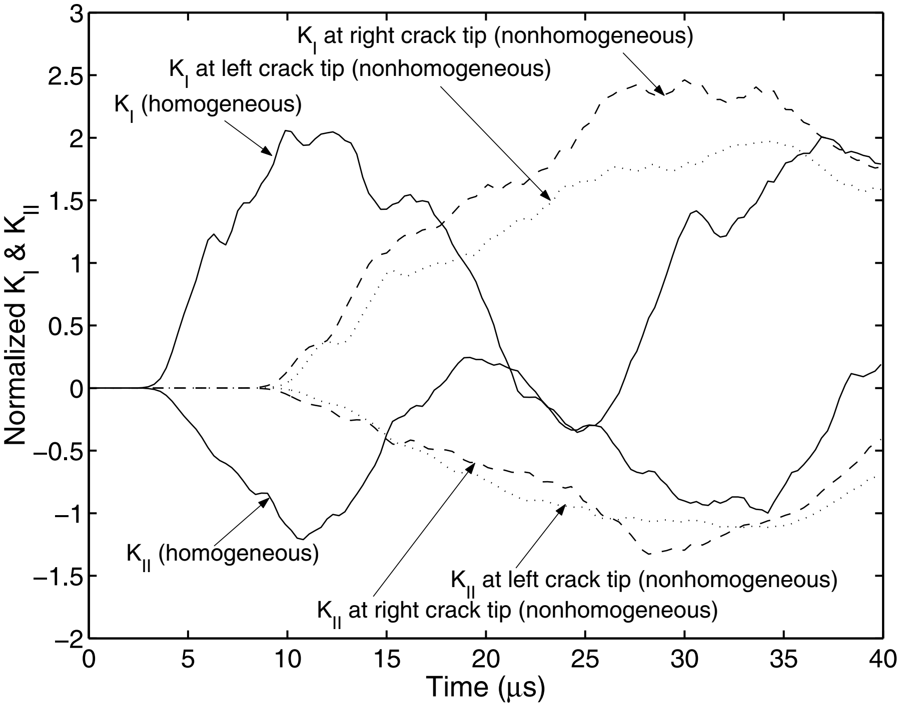

Figure 5.22: Normalized mixed-mode DSIFs at both the left and right crack tips for homogeneous and nonhomogeneous materials.

Chapter 6

Conclusion and Future Work

Dynamic fracture behavior for both homogeneous and nonhomogeneous materials is examined thoroughly using the dynamic fracture research code developed in this study. The investigations include the influence of different material profiles on DSIFs, the relation between initiation time and the domain size, and the contribution of each distinct term in the M-integral. This code has been developed using the implicit time scheme and the M-integral with graded elements, which are implemented by means of the GIF [28]. The non-equilibrium formulation of the M-integral is implemented to evaluate SIFs for both static and dynamic cases. As illustrated in this study, the M-integral is superior to the DCT in terms of accuracy, and unlike the standard J-integral, it yields mixed-mode SIFs directly. The M-integral proves to be an attractive and superior approach in exploring transient dynamic fracture behavior in terms of DSIFs.

In this Chapter, a brief summary of this study is provided. Then, the contribution of this study and suggestions for future work follow.

6.1 Summary

In Chapter 1, literature reviews regarding the evaluation of DSIFs were presented. Throughout the reviews, we found that various numerical schemes such as the FDM, the FEM, the BEM and the EFG have been proposed to set up the dynamic equations. *The DCT, the J-integral, and the modified J-integral have been developed for evaluating DSIFs.* Then, background regarding asymptotic fields for dynamic nonhomogeneous materials were provided. A few works revealed that the asymptotic singular stress fields in nonhomogeneous materials under dynamic condition are identical with those in homogeneous materials under quasi-static condition. Finally, dynamic auxiliary fields for nonhomogeneous materials were discussed in conjunction with non-equilibrium, incompatibility, and constant constitutive formulations. The three different formulations arise due to violation of one of the fundamental properties of mechanics: equilibrium, compatibility and constitutive model. However, this violation is considered and compensated in the formulation.

In Chapter 2, the generalized J-integral considering dynamic effects was derived. The J-integral, which is equivalent to energy release rate under linear elastic condition, was proved to be path independent under the steady state condition, i.e. $\partial u_i/\partial t = -V\partial u_i/\partial x_1$. In other words, if crack speed varies, path independence is violated. We demonstrated theoretically and numerically that the generalized J-integral is reduced to standard J-integral by Rice [46] under stationary condition, i.e. $V = 0$. Then, the J-integral was extended to incorporate material nonhomogeneity and dynamic effects. It is reduced to the J-integral derived by Kim and Paulino [27] for static nonhomogeneous material case and to the one derived by Moran et al. [38] under the stationary condition, i.e. V=0, for dynamic homogeneous case. The M-integral considering material nonhomogeneity and dynamic effects was derived. This M-integral utilizes actual and auxiliary fields superimposed on the J-integral. In the M-integral using non-equilibrium formulation, terms $\sigma_{ij,j}^{aux}u_{i,1}$ and $C_{ijkl,1}\varepsilon_{kl}^{aux}\varepsilon_{ij}$ account for material nonhomogeneity, and $\rho\ddot{u}_i u_{i,1}^{aux}$ accounts for mass effects.

In Chapter 3, the concept of homogeneous elements and graded elements was introduced, and the GIF for graded elements was explained and implemented. Dynamic finite element formulations were presented including the concept of elastodynamics, Newmark β method, and displacement control analysis. Numerical aspects of the M-integral were explained in detail. Transformations are unavoidable in obtaining DSIF using the M-integral because SIF and auxiliary field quantities are local, while the actual quantities are global.

In Chapter 4, benchmark problems were selected to verify the implementation of the implicit time scheme, and the M-integral in the research code. The first problem is an uncracked nonhomogeneous infinite plate where material gradation changes along the x direction. In this problem, stress fields of σ_{yy} were verified by comparing present numerical results with analytical solutions. The second problem is an uncracked homogeneous cantilever beam where displacements of the tip were compared with analytical solutions. It has also been extended to the nonhomogeneous material case. The third problem is a nonhomogeneous unbounded plate with an arbitrarily oriented crack under static condition. In this problem, path-independence for K_I and K_{II} was demonstrated numerically and the M-integral implementation for a static nonhomogeneous medium was verified. The fourth problem is a homogeneous edge cracked semi-infinite plate where path-independence and the M-integral implementation for dynamic homogeneous materials were investigated. The last problem is a nonhomogeneous edge cracked semi-infinite plate. In this problem, field quantities such as displacements and the M-integral implementation for nonhomogeneous materials under dynamic loading were considered.

In Chapter 5, dynamic fracture behavior for homogeneous and nonhomogeneous materials was investigated in the following examples: 1) Homogeneous CCT specimen; 2) Nonhomogeneous CCT specimen with mixed-mode crack behavior; 3) Homogeneous and nonhomogeneous rectangular plate with an inclined crack; 4) Homogeneous and nonhomogeneous rectangular plate with cracks emanating from a circular hole. In the examples, path-independence is assessed and the present numerical results are compared with reference solutions. Besides, the influence of material gradation on DSIFs, the relation between initiation time and the domain size, and the contribution of each distinct term in the M-integral were studied.

6.2 Concluding Remarks and Extensions

The major contributions of this study can be summarized as follows:

- The M-integral is derived to account for material nonhomogeneity and dynamic effects.
- Three different formulations of the M-integral, i.e. non-equilibrium, incompatibility and constant tensor formulations, are derived.
- The mode I and mixed mode DSIFs for both homogeneous and nonhomogeneous materials are evaluated using the M-integral.
- The path-independence of the M-integral is assessed numerically for both homogeneous and nonhomogeneous materials under dynamic loading.
- Fracture behavior is investigated thoroughly for homogeneous and nonhomogeneous materials under dynamic loading, including the influence of material gradation on variations of DSIFs, the relation between initiation time and the domain size, and the contribution of each distinct term in the M-integral.

In this study, consistent mass matrix is used in conjunction with implicit time schemes such as the *average acceleration method* because a consistent mass matrix has the upper-bound property for the frequency and the implicit method slightly dampens the frequency. However, this fact has not been examined for nonhomogeneous materials. Therefore, an investigation of the influence of lumped and consistent mass matrix formulation methods in conjunction with implicit and explicit time schemes for nonhomogeneous materials is recommended. Moreover, extensive dynamic fracture behavior is examined under the assumption of stationary condition, i.e. V=0. Even though good understanding is obtained throughout this study for dynamic fracture behavior of both homogeneous and nonhomogeneous materials, this assumption has limitations of application to crack propagation. Therefore, to better understand more realistic behavior of dynamic problems, i.e. intersonic or supersonic propagation, extension of this code to simulate crack propagation is necessary.

Appendix A

ABAQUS User Subroutine for Graded Elements

```
c
c-------------------------------------------------------------------------
c    Subroutine implemented by S.H.Song
c    University of Illinois at Urbana-Champaign
c
c    * PROBLEM DESCRIPTION
c    This UMAT user subroutine is for isotropic and isothermal materials.
c    This subroutine is designed for 3-D and plane strain problems.
c    This subroutine needs to be modified for plane stress.
c    Both homogeneous and graded properties are possible by selecting
c    appropriate functional form of "props".
c    This UMAT is based on direct integration method
c
c    * IMPORTANT NOTICE
C    For new problems, choose the function for
c    the material variation and the values of "props".
c    After that, go to the section -CHANGE- and change the function and
c    values accordingly
c-------------------------------------------------------------------------
c
      subroutine UMAT(stress, statev, ddsdde, sse, spd, scd,
     & rpl, ddsddt, drplde, drpldt,
     & stran, dstran, time, dtime, temp, dtemp, predef, dpred, cmname,
```

```
     & ndi, nshr, ntens, nstatv, props, nprops, coords, drot, pnewdt,
     & celent, dfgrd0, dfgrd1, noel, npt, layer, kspt, kstep, kinc)
c
      include 'ABA_PARAM.INC'
c
      character*80 cmname
      dimension stress(ntens), statev(nstatv),
     & ddsdde(ntens, ntens),
     & ddsddt(ntens), drplde(ntens),
     & stran(ntens), dstran(ntens), time(2), predef(1), dpred(1),
     & props(nprops), coords(3), drot(3,3), dfgrd0(3,3), dfgrd1(3,3)

c     Determine material properties based on global coordinates of gauss points.
c      coords(1) is X-coordinate of gauss points.
c      coords(2) is Y-coordinate of gauss points.
c      coords(3) is Z-coordinate of gauss points.
c      props is defined by users.
c      The function can be also defined by users.
c
c ----CHANGE------------------------------------------------
       E=props(1)+props(2)*coords(1)+props(3)*coords(2)
     &   +props(4)*coords(3)
       v=props(5)+props(6)*coords(1)+props(7)*coords(2)
     &   +props(8)*coords(3)
c-----------------------------------------------------------
c
c     Determine Lame's constants
c      amu is mu
c      alambda is lambda
c
      amu=E/2.0d0/(1.0d0+v)
      alambda=E*v/(1.0d0+v)/(1.0d0-2.0d0*v)
c
c
c
c     Determine the tangent(Jacobian) matrix
```

```
c
c      ndi is number of normal stresses (e.g. Sxx, Syy, Szz))
c      nshr is number of shear stresses (e.g. Sxy)
c      ntens is dimension of constitutive matrix(ntens=ndi+nshr)
c
      do i=1, ndi
         do j=1, ndi
            if (i.eq.j) then
               ddsdde(i,i)=alambda+2.0d0*amu
            else
               ddsdde(i,j)=alambda
            endif
         enddo
      enddo
      do i=ndi+1, ntens
         ddsdde(i,i)=amu
      enddo

c
c  Determine the stress and update the stress
c
      do i=1, ntens
         do j=1, ntens
            stress(i)=stress(i)+ddsdde(i,j)*dstran(j)
         enddo
      enddo
c
      return
      end
```

References

[1] ABAQUS, Version 6.2, H.K.S. Inc., Pawtucket, RI, 2002.

[2] Anderson, T. L. 1995. *Fracture Mechanics: Fundamentals and Application*, CRC, Boca Raton.

[3] Aoki, S., Kishimoto, K., Kondo, H. and Sakata, M. 1978. Elastodynamic analysis of crack by finite element method using singular element, *International Journal of Fracture*, **14**(1), 59-67.

[4] Belytschko, T. Lu, Y.Y, Gu, L and Tabbara, M. 1995. Element free Galerkin methods for static and dynamic fracture, *International Journal of Solids and Structures*, **32**(17/18), 2547-2570.

[5] Brickstad, B. 1983. A FEM analysis of crack arrest experiments, *International Journal of Fracture*, **21**(3), 177-194.

[6] Bui, H.D. 1983. Associated path independent J-integrals for separating mixed modes, *Journal of the Mechanics and Physics of Solids*, **31**(6), 439-448.

[7] Buttlar, W.G., Paulino, G.H., Song, S.H. Application of graded finite elements for asphalt pavement analysis. *Proceedings of Second MIT Conference on Computational Fluid and Solid Mechanics*, Cambridge, MA, June, 2003.

[8] Chang, J.H and Wu, D.J. 2003. Calculation of mixed-mode stress intensity factors for a crack normal to a bimaterial interface using contour integrals. *Engineering Fracture Mechanics*, **70**(13), 1675-1695.

[9] Chen, Y. M. 1975. Numerical computation of dynamic stress intensity factors by a Lagrangian finite-difference method (the HEMP code), *Engineering Fracture Mechanics*, **7**(4), 653-660.

[10] Chen, Y.M. and Wilkins, M.L. 1976. Stress analysis of crack problems with a three dimensional time dependent computer program, *International Journal of Fracture*, **12**(4), 607-617.

[11] Chiu, T.-C. and Erdogan, F. 1999. One dimensional wave propagation in a functionally graded elastic medium, *Journal of Sound and Vibration*, **222**(3), 453-487.

[12] Cook, R.D., Malkus, D.S. and Plesha, M.E. 1989. *Concepts and Application of Finite Element Analysis*. John Wiley & Sons; New York.

[13] Cook, R.D., Malkus, D.S., Plesha, M.E. and Witt, R.J. 2002. *Concepts and Application of Finite Element Analysis*. John Wiley & Sons : New York.

[14] Delale, F. and Erdogan, F. 1983. The crack problem for a nonhomogeneous plane. *ASME Journal of Applied Mechanics*, **50**, 609-614.

[15] Dolbow, J. and Gosz, M. 2000. On the computation of mixed-mode stress intensity factors in functionally graded materials, *International Journal of Solids and Structures*, **39**(9), 2557-2574.

[16] Dominguez, J. and Gallego, R. 1992. Time domain boundary element method for dynamic stress intensity factor computations, *International Journal for Numerical Methods in Engineering*, **33**(3), 635-647.

[17] Eftis, J., Subramonian, N. and Liebowitz, H. 1977. Crack border stress and displacement equation revisited, *Engineering Fracture Mechanics*, **9**(1), 189-210.

[18] Eischen, J.W. 1987. Fracture of nonhomogeneous materials, *International Journal of Fracture*, **34**(1), 3-22.

[19] Enderlein, M., Ricoeur, A. and Kuna, M. 2003. Comparison of finite element technique for 2D and 3D crack analysis under impact loading. *International Journal of Solids and Structures*, **40**(13/14), 3425-3437.

[20] Erdogan, F., and Wu, B. H. 1997. The surface crack problem for a plate with functionally graded properties, *ASME Journal of Applied Mechanics*, **64**(3), 449-456.

[21] Fedelinski, P, Aliabadi, M.H. and Rooke, D.P. 1994. The dual boundary element method: $\hat{J}$-integral for dynamic stress intensity factors, *International Journal of Fracture*, **65**(4), 369-381.

[22] Freund, L.B. 1998. *Dynamic Fracture Mechanics*, Cambridge University Press, Cambridge.

[23] Freund, L.B. and Clifton, R.J. 1974. On the uniqueness of plane elastodynamic solutions for running cracks, *Journal of Elasticity*, **4**(4), 293-299.

[24] Fung, Y.C. 1965. *Foundation of Solid Mechanics*, Prentice-Hall, Englewood Cliffs, NJ.

[25] Gurtin, M.E. 1976. On a path-independent integral for elastodynamics. *International Journal of Fracture*, **12**(4), 643-644.

[26] Hughes, T. J. R. 2000. *The Finite Element Method: Linear Static and Dynamic Finite Element Analysis*. Dover; New York.

[27] Kim, J.-H. and Paulino, G.H. 2002. Finite element evaluation of mixed mode stress intensity factors in functionally graded materials, *International Journal for Numerical Methods in Engineering*, **53**(8), 1903-1935.

[28] Kim J.-H. and Paulino G.H. 2002. Isoparametric graded finite elements for nonhomogeneous isotropic and orthotropic materials. *ASME Journal of Applied Mechanics*, **69**(4), 502-514.

[29] Kim, J.-H. and Paulino, G.H. 2003. T-stress, mixed-mode stress intensity factors, and crack initiation angles in functionally graded materials: a unified approach using the interaction integral method, *Computer Metheods in Applied Mechanics and Engineering*, **192**(11/12), 1463-1494.

[30] Kim, J.-H. and Paulino, G. H. 2003. Consistent formulations of the interaction integral method for fracture of functionally graded materials (submitted).

[31] Kim, J.-H. and Paulino, G.H. 2003. An accurate scheme for mixed-mode fracture analysis of functionally graded materials using the interaction integral and micromechanics models, *International Journal for Numerical Methods in Engineering*, **58**(10), 1457-1497.

[32] Kishimoto, K., Aoki, S. and Sakata, M. 1980. Dynamic stress intensity factors using J-integral and finite element method, *Engineering Fracture Mechanics*, **13**(2), 387-394.

[33] Konda, N. and Erdogan, F. The mixed mode crack problem in a nonhomogeneous elastic medium, *Engineering Fracture Mechanics*, **47**(4), 533-545.

[34] Krysl, P. and Belytschko, T. 1999. The element free Galerkin method for dynamic propagation of arbitrary 3-D cracks, *International Journal for Numerical Methods in Engineering*, **44**(6), 767-800.

[35] Lee, Y. J. and Freund, L.B. 1990. Fracture initiation due to asymmetric impact loading of an edge cracked plate, *ASME Journal of Applied Mechanics*, **57**(1), 104-111.

[36] Lin, X. and Ballmann, J. 1993. Re-consideration of Chen's problem by finite difference method, *Engineering Fracture Mechanics*, **44**(5), 735-739.

[37] McGuire, W., Gallagher, R.H. and Ziemian, R.D. 2000. *Matrix Structural Analysis*, John Wiley & Sons : New York.

[38] Moran, B. and Shih, F. C. 1987. Crack tip and associated domain integrals from momentum and energy balance. *Engineering Fracture Mechanics*, **27**(6), 615-642.

[39] Murti, V. and Valliappan, S. 1986. The use of quarter point element in dynamic crack analysis, *Engineering Fracture Mechanics*, **23**(3), 585-614.

[40] Nakamura, T., Shih, F.C. and Freund, L. B. 1985. Computational methods based on an energy integral in dynamic fracture. *International Journal of Fracture*, **27**(3/4), 229-243.

[41] Newmark, N.M. 1959. A method of computation for structural dynamics, *Journal of the Engineering Mechanics Division, ASCE*, **85**(3), 67-94.

[42] Nilsson, F. 1974. A note on the stress singularity at a non-uniformly moving crack tip, *Journal of Elasticity*, **4**(1), 73-75.

[43] Parameswaran, V. and Shukla, A. 1999. Crack tip stress fields for dynamic fracture in functionally gradient materials, *Mechanics of Materials*, **31**(9), 579-596.

[44] Raju, I.S. and Shivakumar, K.N. 1990. An equivalent domain integral method in the two dimensional analysis of mixed mode crack problems. *Engineering Fracture Mechanics*, **37**(4), 707-725.

[45] Rao, B.N. and Rahman, S. 2003. Mesh-free analysis of cracks in isotropic functionally graded materials, *Engineering Fracture Mechanics*, **70**(1), 1-27

[46] Rice, J. R. 1968. A path-independent integral and the approximate analysis of strain concentration by notches and cracks, *ASME Journal of Applied Mechanics*, **35**(2), 379-386.

[47] Rice, J.R. 1968. Mathematical analysis in the mechanics of fracture, in Fracture, Vol II, ed. by H. Liebowitz, Academic Press, 191-311.

[48] Rousseau, C.-E. and Tippur, H. V. 2001. Dynamic fracture of compositionally graded materials with cracks along the elastic gradient: experiment and analysis, *Mechanics of Materials*, **33**(7), 403-421.

[49] Shih, C.F., deLorenzi, H.G. and German, M.D. 1976. Crack extension modeling with singular quadratic isoparametric elements, *International Journal of Fracture*, **12**, 647-651.

[50] Sladek, J, Sladek, V and Fedelinski, P. 1997. Integral formulation for elastodynamic T-stresses, *International Journal of Fracture*, **84**(2), 103-116.

[51] Sladek, J, Sladek, V and Fedelinski, P. 1999. Computation of the second fracture parameter in elastodyanamics by the boundary element method, *Advances in Engineering Software*, **30**(9/11), 725-734.

[52] Tabiei, A. and Wu, J. 2003. Development of the DYNA3D simulation code with automated fracture procedure for brick elements, *International Journal for Numerical Methods in Engineering*, **57**(14), 1979-2006.

[53] Tan, M. and Meguid, S.A. 1996. Dynamic analysis of cracks perpendicular to bimaterial interfaces using a new singular finite element. *Finite Elements in Analysis and Design*, **22**(1), 69-83.

[54] Vargas, P.M. and Dodds, Jr. R.H. 1995. Inelastic response of a deep crack single-edge notch specimen under impact loading. *ASME Journal of Offshore Mechanics and Arctic Engineering*, **117**(3), 205-211.

[55] Warburton, G.B. 1976. *The Dynamical Behavior of Structures*, Pergamon: Oxford.

[56] Wen, P.H., Aliabadi, M.H. and Rooke, D.P. 1997. A contour integral method for dynamic stress intensity factors, *Theoretical and Applied Fracture Mechanics*, **27**(1), 29-41.

[57] Whirley, R.G. and Engelmann, B.E. 1993. *DYNA3D User Manual*, Lawrence Livermore National Laboratory.

[58] Williams, M.L. 1957. On the stress distribution at the base of a stationary crack, *ASME Journal of Applied Mechanics*, **24**(1), 109-114.

[59] Wu, C.-C., He P. and Li, Z. 2002. Extension of J integral to dynamic fracture of functional graded material and numerical analysis. *Computers and Structures*, **80**(5/6), 411-416.

[60] Yau, J.F., Wang, S. S. and Corten, H. T. 1980. A mixed mode crack analysis of isotropic solids using conservation laws of elasticity. *ASME Journal of Applied Mechancis*, **47**(2), 335-341.

[61] Zhang, Ch. 2002. A 2D hypersingular time domain traction BEM for transient elastodynamic crack analysis, *Wave Motion*, **35**(1), 17-40.

Vita

Seong Hyeok Song was born on May 21, 1972, in Cheju, Korea. He earned his B.E. degree from the Department of Civil Engineering, University of Seoul, in February 2000. He was admitted to the Department of Civil and Environmental Engineering, University of Illinois at Urbana-Champaign, in August 2000. He had worked for the Champaign Caterpillar Simulation Center of NCSA at University of Illinois at Urbana-Champaign from June 2001 to May 2002 as a graduate assistant. Since June 2002, he has been employed as a graduate research assistant for Grant Opportunities for Academic Liaison with Industry (GOALI) project.